

OPTIMIZATION OF OPTICAL CHARACTERISTICS OF A STRAINED NITRIDE SEMICONDUCTOR BASED QUANTUM WELL LASER

by

Md. Mobarak Hossain Polash
Student No.: 0412062228

MASTER OF SCIENCE IN ELECTRICAL AND ELECTRONIC ENGINEERING



**Department of Electrical and Electronic Engineering
Bangladesh University of Engineering and Technology (BUET)**

May 2015

OPTIMIZATION OF OPTICAL CHARACTERISTICS OF A STRAINED NITRIDE SEMICONDUCTOR BASED QUANTUM WELL LASER

A thesis submitted to the department of Electrical and Electronic Engineering, Bangladesh University of Engineering Technology (BUET), Dhaka, Bangladesh in partial fulfillment of the requirements for the degree of Master of Science in Electrical and Electronic Engineering.

by

Md. Mobarak Hossain Polash,
Student No.: 0412062228

Under the supervision of

Dr. Md. Shah Alam
Professor, Department of EEE, BUET



**Department of Electrical and Electronic Engineering
Bangladesh University of Engineering and Technology (BUET)**

May 2015

APPROVAL CERTIFICATE

The thesis titled “**OPTIMIZATION OF OPTICAL CHARACTERISTICS OF A STRAINED NITRIDE SEMICONDUCTOR BASED QUANTUM WELL LASER**” submitted by Md. Mobarak Hossain Polash, Student ID: 0412062228 F, Session: April 2012 has been accepted as satisfactory in partial fulfillment of the requirement for the degree of Master of Science in Electrical and Electronic Engineering on June 10, 2015.

BOARD OF EXAMINERS

1.

Chairman
(Supervisor)

Dr. Md. Shah Alam
Professor
Department of EEE
Bangladesh University of Engineering and Technology, Dhaka-1000.

2.

Member
(Ex-Officio)

Dr. Taifur Ahmed Chowdhury
Professor and Head
Department of EEE
Bangladesh University of Engineering and Technology, Dhaka-1000.

3.

Member

Dr. Md. Ziaur Rahman Khan
Professor
Department of EEE
Bangladesh University of Engineering and Technology, Dhaka-1000.

4.

Member
(External)

Dr. Kazi Mohiuddin Ahmed
Professor
Department of EEE
University of Asia Pacific (UAP), Dhaka-1209.

DECLARATION

This is to certify that this thesis is the result of the work of the undersigned. No part of this work has been submitted elsewhere, partially or fully, for the award of any other degree or diploma. Any material reproduced in this thesis has been properly acknowledged.

(Md. Mobarak Hossain Polash)

Signature of the supervisor,

(Prof. Dr. Md. Shah Alam)

ACKNOWLEDGEMENT

First of all, the author expresses his profound gratitude to his supervisor, Professor Dr. Shah Alam, Department of electrical and electronic engineering, BUET, for allowing the author to enter into the amazingly interesting world of Quantum Well (QW) based optoelectronic device like LED and laser and teaching the author how to perform research work. Without his continuous supervision, guidance, encouragement and valuable advice, it would have been impossible to complete the work. The author is especially grateful to him for providing continuous encouragement throughout this thesis work and for his patience which he has shown with the author.

The author sincerely thanks to Mr. Saumya Biswas, Ph. D. student, Department of EEE, University of California, Riverside for his suggestions and many valuable discussions regarding my work. Author also like to thank him for his assistance in developing the numerical simulation model.

Thanks are given to Professor Dr. Md. Taifur Ahmed Chowdhury, the head of the department of EEE, BUET for his continuous support and encouragement. Sincerest thanks are given to my friends for their continuous encouragement and for more valuable discussions.

Author also likes to express his esteemed gratitude to his all faculty members of Department of EEE, BUET for their great assistance with teaching and motivation. Without their painstaking help in acquiring knowledge, these work could not be completed.

Lastly, author expressed his esteemed gratitude to his parents and family as well as all of his friends for their continuous motivations and inspiration which help him lot to conduct the thesis work.

ABSTRACT

In this work, a wurtzite-strained nitride based single quantum well laser structure has been designed using a 12Å InN well layer and 15Å In_{0.25}Ga_{0.75}N barrier layer which is characterized and optimized for an optical output of 1330nm wavelength known for short distance communication. A Separate Confinement Heterostructure (SCH) layer of GaN has been used for providing better confinement for carrier and photon. Materials and device parameters are selected using practical considerations for fabrication process. A self-consistent Schrodinger Solver along with a simulation model for obtaining optical properties has been developed for the characterization which is verified with previously published work. In self-consistent Schrodinger solver, two Schrodinger equations for both conduction and valence band have been solved followed by the performance of Poisson's equation. The 6-band ***k.p*** formalism has been utilized for valence band calculation including valence band mixing, strain effect, spontaneous polarization, and piezoelectric polarization effect, etc. With the performed energy subbands, interband transition momentum matrix elements are calculated. Several optical characteristics like spontaneous emission rate, material gain, radiative recombination current density etc. are performed from the obtained electronic properties. Also parameters like, peak material gain versus carrier density and material gain versus radiative recombination current density are found out to characterize the structure. At carrier density of $6 \times 10^{19} \text{ cm}^{-3}$ and $T = 300\text{K}$, the peak optical gain of $5261.5187 \text{ cm}^{-1}$ has been found at emission wavelength of 1336.7 nm. The peak spontaneous emission rate per energy interval per volume is $7.21 \times 10^{27} \text{ s}^{-1} \text{ cm}^{-3} \text{ eV}^{-1}$ at 1329.55 nm wavelength. Later, a genetic algorithm based optimization process has been performed to obtain the maximum spontaneous emission rate and maximum optical gain for the structure taking well width, barrier width, injection carrier density and SCH width are taken as variables into consideration. From the characterization, it has been found that the device will provide good amplification for TE-polarization light. This structure shows a good amount of spontaneous emission rate for lasing action with respect to the other structures published previously. Moreover, it shows a good improvement of material gain which will provide better LED and LASER action. A higher differential gain has been found for this structure which will provide higher modulation bandwidth and lower frequency chirp. Besides, the structure shows good amount of optical gain with respect to recombination current density. All these performances make this structure promising for LASER application at around 1330nm emission wavelength.

TABLE OF CONTENTS

Approval Certificate	i
Declaration	ii
Acknowledgement	iii
Abstract	iv
Table of Contents	v
List of Figure	vii
List of Tables	xii

Chapter One: Introduction

1.1 Background	1
1.2 Laser	2
1.3 Semiconductor Laser	3
1.4 Nitride Semiconductor Laser	3
1.5 Objectives of The Work	4
1.6 Organization of The Thesis	5

Chapter Two: Background Physics

2.1 Principle of Operation of a Laser	6
2.1.1 Matter-Energy Interaction	7
2.1.2 Pumping Process and Population Inversion	8
2.1.3 Optical Feedback System	9
2.2 General Theory of a Diode Laser	10
2.3 Different Structures of a Diode Laser	12
2.3.1 Homojunction Diode Lasers	13
2.3.2 Heterojunction Laser	13
2.3.3 Double Heterostructure Laser	15
2.3.4 Quantum Well Lasers	16
2.3.5 Separate Confinement Heterostructure	18
2.3.6 Multiple Quantum Well Lasers	18
2.4 Long Wavelength Semiconductor Laser	18
2.5 Nitride Semiconductor Laser/LED	19

Chapter Three: Device Physics and Numerical Model

3.1 Introduction	24
3.2 Crystal and Energy Band Symmetry	25

3.2.1 Crystal Symmetry	25
3.2.2 Energy Band Symmetry	25
3.3 Crystal Structure of Nitride Semiconductor	27
3.4 Strain in Nitride Semiconductor	29
3.5 Piezoelectric Effect	34
3.6 Electronic Band Structures Formation with Strain Effects	36
3.7 Poisson's Equation	43
3.8 Characteristic Equations of the Optical Properties	45
3.9 Optimization using Genetic Algorithm	49
3.9.1 GA's Parameters	51
 Chapter Four: Design of the Structure and Validation of Numerical Model	
4.1 Design of the Laser Structure and Selection of Material	53
4.2 Band Energy Profile of the Laser Structure	56
4.3 Work Flow of Numerical Model	57
4.4 Validation of the Numerical Model	59
 Chapter Five: Analysis of the Laser Characteristics	
5.1 Calculation of Electronic Band Structure	64
5.2 Calculation of the optical transition matrix elements	70
5.3 Calculation of Optical Properties of the Designed Structure	72
5.4 Optimization of the Laser Parameters	83
 Chapter Six: Conclusion and Future work	
6.1 Conclusion of the Work	85
6.2 Scope of Future Works	87
 References	90

LIST OF FIGURES

Figure 2.1	Schematic diagrams illustrating fundamental concept of a laser. (a) Gain medium with optical input and output, (b) increase in gain in a round-trip through gain medium, (c) gain medium with permanent optical source, and (d) optical output through anti-reflecting facet of the laser.	6
Figure 2.2	Integral Parts of a typical laser oscillator showing the laser gain medium, the mirrors of the cavity, energy pumping towards the medium and coming output of the laser beam from one of the mirror.	7
Figure 2.3	Illustrative diagrams of the three matter-energy interaction mechanisms (a) stimulated emission, (b) spontaneous emission, and (c) absorption.	8
Figure 2.4	Illustrative diagrams showing the stimulated matter-energy interaction mechanisms.	8
Figure 2.5	Three and four level lasing system showing the pumping and decay system.	9
Figure 2.6	Plot of energy vs. wavenumber for direct and indirect band gap materials showing the emission of photon and phonon.	11
Figure 2.7	Diode laser structures showing emission process in active region.	11
Figure 2.8	Major categories of edge-emitting diode lasers with their different layers and corresponding materials. Three structures are shown with their respective light confinement.	15
Figure 2.9	Schematic diagram of a typical structure of a Double hetero-structure semiconductor injection laser showing its all layers, injection current and output light from laser.	16
Figure 2.10	A single quantum well (top) is surrounded by thicker layers of higher Bandgap material. Forming layers with lower refractive index on top and bottom produces a separate carrier and optical confinement heterostructure (SCH). Grading the refractive index of the confinement layer produces the graded-index and separate carrier and optical confinement heterostructure (GRINSCH) laser. Multiple quantum wells also can be stacked in the active layer, as shown at bottom.	17
Figure 2.11	Plot of path loss (dB/km) vs. wavelength produced by the laser structure. Figure shows the minima region at around 1550 nm range.	19
Figure 2.12	Orientation of crystal planes exposed to the epitaxial growth in polar (c-plane) and nonpolar (m-plane) direction with corresponding energy band diagrams and the position of electron and hole wavefunctions.	22
Figure 3.1	(a) An illustration of a 2D lattice which is the same after being translated by a in either x or y direction. (b) Diagram of point symmetry for the 2D lattice.	24
Figure 3.2	The first Brillouin zone or Brillouin zone for (a) a 2D lattice shown in figure 3.1a, and (b) a FCC lattice, with a lattice constant a .	25

Figure 3.3	Energy band-gap range for nitride semiconductor binaries materials and their ternaries along with the wavelength range.	27
Figure 3.4	Wurtzite nitride semiconductor crystal structure showing relative atom positions and corresponding axes and planes.	27
Figure 3.5	Schematic illustration of the diagonal strain components on the crystal structure. In the literature an intuitive notation is occasionally seen replacing the indices 1, 2 and 3 with x, y and z, e.g. $\epsilon_{11} \rightarrow \epsilon_{xx}$.	28
Figure 3.6	Directions of the stress components acting on a crystal lattice.	29
Figure 3.7	Schematic illustration of a substrate with two mismatched layers, (a) shows the free-standing unstrained layers with lattice constants smaller $a_l < a_0$ (material A) and larger $a_l > a_0$ (material B) than the lattice constant of the substrate and (b) shows the situation when either of the materials is grown on the substrate, i.e. material A is under tensile strain and material B is under compressive strain as their lattice constants are forced to be equal to the lattice constant of the substrate.	31
Figure 3.8	Illustration of the conduction band edge of a quantum well with a strain induced energy band shift while the original conduction band discontinuity is E_c .	32
Figure 3.9	Schematic diagram showing the bulk band structures of (a) an unstrained GaN wurtzite semiconductor and (b) a compressively strained GaN layer.	33
Figure 3.10	Illustration of the charge separation in GaN grown along the [0001] direction which causes the appearance of an uncompensated polarization. The left hand diagram shows the unstrained crystal lattice, and on the right the atomic positions when under strain.	34
Figure 3.11	Schematic diagram of a multilayer structure based on piezoelectric material.	37
Figure 3.12	Schematic diagram of typical induced internal electric fields in a quantum well and barrier region based on piezoelectric materials.	38
Figure 3.13	Elaborate illustration of electronic band energies (both conduction and valence band edge) for different sign of Δ_1 for GaN (left side) and AlN (right side).	40
Figure 3.14	A typical doped single quantum well structure showing only conduction band profile.	42
Figure 3.15	The work flow diagram of the Genetic algorithm based optimization operation.	50
Figure 4.1	Polarization induced red-shift and reduction of oscillator strength in optical devices.	52
Figure 4.2	Energy band profile of InN-InGaN quantum well structure with strain effect. Red line represents the conduction band edge and blue line is the valence band edge.	55

Figure 4.3	Energy band profile of InN-InGaN quantum well structure with strain effect and polarization induced internal electric field. Black line represents the conduction band edge and red line is the valence band edge.	55
Figure 4.4	Numerical flow chart of the simulation process for self-consistent model of 6-band $\mathbf{k}\cdot\mathbf{p}$ Hamiltonian for wurtzite nitride semiconductor quantum well active region.	56
Figure 4.5	Comparison between the performed result (left) and published result (right) for valence band energy of 26Å GaN well layer with Al _{0.3} Ga _{0.7} N barriers.	59
Figure 4.6	Illustration of comparison between valence band energy levels of 50Å GaN - 50Å Al _{0.3} Ga _{0.7} N Quantum well structure. Left figure is performed with our developed model and right figure is published in [55].	60
Figure 4.7	Comparison between obtained (left) and published (right) result of normalized momentum-matrix elements for the first conduction (Cl) subband to the HH1, the LHI, and the CH1 subband transitions for TE polarization (on the x-y plane, which is perpendicular to the c axis (=z axis)) for a well width $L_z = 26$ Å.	60
Figure 4.8	Comparison between obtained (left) and published (right) result of normalized momentum-matrix elements for the first conduction (Cl) subband to the HH1, the LHI, and the CH1 subband transitions for TM polarization (on the z axis) for a well width $L_z = 26$ Å.	61
Figure 4.9	Illustration of gain co-efficient and spontaneous emission rate spectrum of GaN-AlGaIn for 26Å well width. Left figure is performed with our developed model and right figure is published in [55].	61
Figure 4.10	Illustration of gain co-efficient and spontaneous emission rate spectrum of GaN-AlGaIn for 50Å well width. Left figure is performed with our developed model and right figure is published in [55].	62
Figure 4.11	Illustration of comparison between performed (left) and published (right) result of hole energy levels of 30Å Al _{0.8} Ga _{0.2} N / 3Å GaN QW for T = 300K. Device structure is shown in right figure.	62
Figure 4.12	Illustration of optical gain for TE polarization and TM polarization of 30Å Al _x Ga _{1-x} N / 3Å GaN delta layer with AlN barriers at T = 300K for 5×10^{19} cm ⁻³ injection carrier density. The left figure has been performed with our developed numerical model and the right figure has been published in [78].	63
Figure 5.1	Obtained conduction subband energy for the laser structure with respect to wave vector, k_t . Here 8 conduction subbands are illustrated.	65
Figure 5.2	Obtained valence subband energy for the laser structure with respect to wave vector, k_t . Here only 8 valence subbands are illustrated with their subband characteristics.	65

Figure 5.3	Obtained valence subband energy of lower Hamiltonian for the laser structure with respect to wave vector, k_x . Here only 8 valence subbands are illustrated with their subband characteristics.	66
Figure 5.4	Weight functions of the envelop function of Upper Hamiltonian are shown.	66
Figure 5.5	Conduction subband energy levels with their corresponding wave functions formed in the quantum well of conduction band.	67
Figure 5.6	E-k diagram for InN-InGaN-GaN quantum well laser structure.	68
Figure 5.7	Energy band profile of the designed structure from the self-consistent analysis along with the quasi Fermi level.	68
Figure 5.8	Four envelop functions obtained from the solution of $k.p$ based Hamiltonian for the designed laser structure for first valence subband at $k = 1$. (a) gm^1 , (b) gm^4 , (c) gm^2 and (d) gm^5 .	69
Figure 5.9	Illustration of electron hole wave functions overlap integral with respect to device length.	70
Figure 5.10	Square of momentum matrix elements of the TE-polarization for InN (12 Å) / $In_{0.25}Ga_{0.75}N$ (10 Å) SQW at carrier density of $4 \times 10^{19} \text{ cm}^{-3}$.	71
Figure 5.11	Square of momentum matrix elements of the TM-polarization for InN (12 Å) / $In_{0.25}Ga_{0.75}N$ (10 Å) SQW at carrier density of $4 \times 10^{19} \text{ cm}^{-3}$.	72
Figure 5.12	Spontaneous emission rate for TE polarization for InN-InGaN quantum well structure at $3 \times 10^{19} \text{ cm}^{-3}$ carrier density at $T=300 \text{ K}$.	73
Figure 5.13	Spontaneous emission rate for TE polarization for InN-InGaN quantum well structure at $6 \times 10^{19} \text{ cm}^{-3}$ carrier density at $T=300 \text{ K}$.	73
Figure 5.14	Spontaneous emission rate for TM polarization at $3 \times 10^{19} \text{ cm}^{-3}$ carrier density at $T=300 \text{ K}$.	74
Figure 5.15	Spontaneous emission rate for TM polarization at $6 \times 10^{19} \text{ cm}^{-3}$ carrier density at $T=300 \text{ K}$.	74
Figure 5.16	TE-polarized optical gain spectrum of 12Å InN-InGaN quantum well with GaN layer for carrier density of $3 \times 10^{19} \text{ cm}^{-3}$ at $T = 300 \text{ K}$.	75
Figure 5.17	TE-polarized optical gain spectrum of 12Å InN-InGaN quantum well with GaN layer for carrier density of $6 \times 10^{19} \text{ cm}^{-3}$ at $T = 300 \text{ K}$.	76
Figure 5.18	Optical gain spectrum of TM polarization for InN-InGaN QW structure with GaN layer for carrier density of $3 \times 10^{19} \text{ cm}^{-3}$ at $T = 300 \text{ K}$.	76
Figure 5.19	Optical gain spectrum of TM polarization for InN-InGaN QW structure with GaN layer for carrier density of $6 \times 10^{19} \text{ cm}^{-3}$ at $T = 300 \text{ K}$.	77
Figure 5.20	TE polarized optical gain spectra of strained 12Å InN- $In_{0.25}Ga_{0.75}N$ quantum well with GaN layer for carrier density (n) from $2 \times 10^{19} \text{ cm}^{-3}$ up to $6 \times 10^{19} \text{ cm}^{-3}$ at $T = 300 \text{ K}$.	77
Figure 5.21	TE polarized optical gain spectra with respect to emission wavelength of strained 12Å InN- $In_{0.25}Ga_{0.75}N$ quantum well with GaN layer for carrier density (n) from $2 \times 10^{19} \text{ cm}^{-3}$ up to $6 \times 10^{19} \text{ cm}^{-3}$ at $T = 300 \text{ K}$.	78

Figure 5.22	Spontaneous emission spectrum of 12Å InN-In _{0.25} Ga _{0.75} N quantum well with GaN layer for carrier density (n) form $3 \times 10^{19} \text{cm}^{-3}$ at T = 300 K.	79
Figure 5.23	Spontaneous emission spectrum of 12Å InN-In _{0.25} Ga _{0.75} N quantum well with GaN layer for carrier density (n) form $6 \times 10^{19} \text{cm}^{-3}$ at T = 300 K.	79
Figure 5.24	Spontaneous emission spectra of strained 12Å InN-In _{0.25} Ga _{0.75} N quantum well with GaN layer for carrier density (n) form $2 \times 10^{19} \text{cm}^{-3}$ up to $6 \times 10^{19} \text{cm}^{-3}$ at T = 300 K.	80
Figure 5.25	Spontaneous emission spectra with respect to emission wavelength of strained 12Å InN-In _{0.25} Ga _{0.75} N quantum well with GaN layer for carrier density (n) form $2 \times 10^{19} \text{cm}^{-3}$ up to $6 \times 10^{19} \text{cm}^{-3}$ at T = 300 K.	80
Figure 5.26	Spontaneous emission radiative recombination rate per unit volume as a function of carrier density at 300 K for 12Å InN-In _{0.25} Ga _{0.75} N quantum well.	81
Figure 5.27	Peak material gain as a function of carrier density at 300 K for the designed laser structure.	82
Figure 5.28	Material gain or optical gain versus radiative current density of InN-InGaN quantum well structure.	83

LIST OF TABLES

Table 2.1	Different communication system with their respective bit rates	19
Table 3.1	Comparison between the heuristic optimization techniques	50
Table 4.1	The material parameter Table for GaN, AlN and InN	53

Chapter One

Introduction

1.1 Background

It took many years to put the key concepts of laser physics together into a working laser. The basic idea of the stimulated emission of radiation was originated by Albert Einstein in 1916 [1]. In 1939, V. A. Fabrikant in his Doctor of Science (Habilitation) Thesis pointed out that population inversion should lead to light wave amplification and suggested the use of second kind of collisions to achieve such an inversion [2]. Fundamental theory of the laser was first proposed by Schawlow and Townes, Bell Laboratories researchers in 1958 [1]. In 1964, Townes, Basov and Prokhorov are awarded the Nobel Prize in physics for their fundamental work in the field of quantum electronics, which has led to the construction of oscillators and amplifiers based on the maser-laser-principle [1-2]. The early 1960s saw an amazing and rapid proliferation of laser types, followed by years of experimentation with assiduous efforts. In May 16, 1960, Theodore H. Maiman, a physicist at Hughes Research Laboratories in Malibu, California, constructed the first laser using a cylinder of synthetic ruby measuring 1 cm in diameter and 2 cm long, with the silver-coated ends to make them reflective and able to serve as a Fabry–Perot resonator. Maiman used photographic flashlamps as the laser’s pump source [1-3]. In 1962, Robert N. Hall invented the semiconductor injection laser [4], a device now used in all compact disk players and laser printers, and most optical fiber communications systems. Robert Hall and his group at General Electric (Schenectady, NY) published the first report of laser action in a semiconductor (GaAs) in September 1962. Nathan M.I. *et al.* groups at IBM (Yorktown Heights, NY) [5] and Quist T.M. *et al.* groups of the Massachusetts Institute of Technology (Cambridge, MA) [6], reported their successes at the same time. Soon after, researchers reported lasing in a variety of materials in the near-IR wavelengths. Visible coherent light emission was obtained from GaAsP by Holonyak N. and Bevacqua S.F. [7]. The first experimental results on stimulated emission at electron beam pumping from a CdS crystal have been reported in 1964 [8].

Modern semiconductor lasers incorporate a heterostructure in which the active layer is surrounded by higher bandgap material. In 1963, the team of Rudolf Kazarinov and Zhores Alferov of Ioffe Institute in Leningrad, USSR [9], and Herbert Kroemer of the University of California, Santa Barbara [10], independently proposed ideas to build modern semiconductor lasers from heterostructure devices. In 1967, J.M. Woodall *et al.* became successful in growing heterostructures of GaAs and AlGaAs by liquid phase epitaxy (LPE) [11]. In 1970, researchers (Alferov Zh.I. *et al.*) at the Ioffe Institute in Leningrad, USSR, made the first double-heterostructure laser [12] and achieved CW operation at room temperature. Their success was followed almost immediately by a nearly identical but independently conceived design from Bell Labs (Murray Hill, NJ) by Hayashi *et al.* [13]. The double heterostructure became the basic framework for all future development. The role of the heterostructure in the early laser was

described as providing a barrier that blocked the diffusion of electrons. Without grading of interfaces and depletion effects, the heterostructure acts as a potential well for electrons in the conduction band and holes in the valence band. At that stage, researchers tried to model the performance of the extremely thin lasers where spatial quantization occurred. The first work in this effort was that of L. Esaki and R. Tsu of IBM in 1970 [14], who considered carrier transport in a superlattice, an additional periodic potential formed in a semiconductor by doping or alloy composition and having a period of order 100\AA . They concluded that a parabolic band would break into mini-bands separated by small forbidden gaps and having Brillouin zones associated with the period. In 1971, Kazarinov and R.A. Suris of the Ioffe Institute analyzed the effect of current transport through a superlattice [15]. They showed that the transport between wells would consist of tunneling through the barrier layers separating the wells. In 1972, Charles H. Henry invents the quantum-well laser [2-3], which requires much less current to reach lasing threshold than conventional diode lasers and which is exceedingly more efficient. Holonyak at the University of Illinois at Urbana-Champaign first demonstrated the quantum-well laser in 1978 [16]. But practical interest to lasers of such type appeared from 1982, when technology became more precise.

Recently, nitride lasers and LEDs have gotten a great importance for their better performance in visible wavelength spectrum and their wide range of applications. In 1971, Pankove *et al.* reported the first GaN-based light emitting diode (LED) [17]. In 1971, Giretmet first demonstrated the laser design using quaternary compounds (GaInAsP) [2]. Lasers with distributed feedback (DFB) and Bragg reflectors (DBR) has been reported by Fiztekh in 1974 [2]. Later in 1979, Kenichi Iga from Japan showed the idea of vertical cavity surface emitting laser (VCSEL) [18]. In 1994, the first semiconductor laser that can simultaneously emit light at multiple widely separated wavelengths known as quantum cascade laser (QCL), has been invented at Bell Labs by the team of Federico Capasso [19]. Shuji Nakamura, now professor of University of California, Santa Barbara, has announced the development of a gallium-nitride (GaN) laser that emits bright blue-violet light in pulsed operation in 1995 [20]. After the successful fabrication and demonstration of blue laser, researchers has reported the other nitride based laser systems for other visible wavelengths. In 2014, Nakamura has awarded for Nobel Prize in physics for his invention of the blue-laser.

1.2 Laser

Laser, an acronym for light amplification by the stimulated emission of radiation, is a quantum generator of coherent optical radiation in the infrared, visible, or ultraviolet regions of the electromagnetic spectrum (from around 300 nm to 3300 nm). It employs stimulated (induced) radiation of atoms and resonant feedback (cavity) [1-3]. There are three key components of the quantum generators: the matter gain medium with the energy level structure in which radiation can be generated in the desired frequency range, methods for achieving population inversion, and the electrodynamic system where radiation interacts with the gain medium. It amplifies light and produces a highly directional, high-intensity beam that most often has a very pure frequency or wavelength [1-3].

1.3 Semiconductor Laser

Semiconductor lasers are made by using semiconductor gain media, where optical gain is usually achieved by stimulated emission at an interband or intersubband transition under conditions of a high carrier density in the conduction band [21]. Compared to all laser types, semiconductor lasers are compact, reliable and last a long time. Such lasers consist of two basic components, an optical amplifier and a resonator. The amplifier is made from a direct-bandgap semiconductor material. These are compounds based on the Group III and Group V elements in the periodic table. Alloys of these materials are formed onto the substrates as layered structures containing precise amounts of other materials. The resonator continuously recirculates light through the amplifier and helps to focus it. This component usually consists of a waveguide and two plane-parallel mirrors. These mirrors are coated with a material to increase or decrease reflectivity and to improve resistance from being damaged from the high power densities. The performance and cost of a semiconductor laser depends on its output power, brightness, and operating lifetime. Power is important because it determines the maximum throughput or feed rate of a process. High brightness, or the ability to focus laser output to a small spot, determines power efficiency. Lifetime is important because the longer a laser lasts, the less it costs to operate, which is especially critical in industrial applications.

1.4 Nitride Semiconductor Laser

Early research programs on nitride semiconductor laser were abandoned due to fundamental material problems. There was no suitable bulk-crystal technology for producing GaN substrates. Epitaxy was done on highly lattice-mismatched substrates. The resulting heteroepitaxial films exhibited a high defect density and poor surface morphology. Besides, the high n-type background doping, coupled with the deep ionization levels of common acceptors, resulted in an inability to grow p-type materials [17]. During the mid-1980s, these problems began to be overcome, due to the rigorous work of Isamu Akasaki at Nagoya and Meijo Universities and Shuji Nakamura at Nichia Chemical Company in Japan. The use of AlN or GaN nucleation layers facilitated the growth of high-quality GaN films on sapphire substrates by metalorganic chemical vapor deposition (MOCVD). Finally, Nakamura *et al.* succeeded, in 1995, in manufacturing the first nitride-based laser diode with continuous-wave room-temperature emission at 417 nm wavelength [22]. Blue and green nitride LEDs are now widely used, for instance, in full-color displays and in traffic signals. Nitride laser diodes are key components in emerging high-definition DVD players. Other promising application areas are printing, sensors, communication, and medical equipment. However, despite intense research efforts worldwide, there still remains a strong need for a more detailed understanding of microscopic physical processes in nitride devices [17]. Numerical simulation can help to investigate those processes and to establish quantitative links between material properties and measured device performance. Nitride materials provide some unique features for optoelectronic devices. Depending on the alloy composition, the direct bandgap of nitride materials varies from about 0.7 eV to 6.2 eV, covering a wide wavelength range from red

through yellow and green to blue and ultraviolet. While other compound semiconductors, such as GaAs and InP, are grown in the zinc blende crystal system, nitride devices are grown in the hexagonal (wurtzite) crystal system. This leads to unique material properties, such as built-in electric fields due to spontaneous and piezoelectric polarization. Sapphire (Al_2O_3) or SiC are often used as substrates for GaN growth, which exhibit slightly different lattice constants a of 0.476 nm and 0.308 nm, respectively. The lattice-mismatched epitaxial growth causes a large number of dislocations in nitride devices, with dislocation densities that are more than five orders of magnitude higher than in other compound semiconductor devices. Another unique property of nitrides is the high activation energy for acceptor (Mg) doping of about 170 meV. It requires high doping densities near 10^{20} cm^{-3} to achieve free hole concentrations of about 10^{18} cm^{-3} . The high doping density causes an extremely low hole mobility on the order of $10 \text{ cm}^2\text{V}^{-1}\text{s}^{-1}$. On the other hand, the high GaN electron mobility of up to $2000 \text{ cm}^2\text{V}^{-1}\text{s}^{-1}$ and the large critical breakdown field of more than 3MVcm^{-1} are advantageous in high-speed and high power electronics. The thermal conductivity in GaN is more than three times higher than in GaAs. These materials have high melting points (strong bond with N) [17, 23].

1.5 Objectives of The Work

Recently, wurtzite-strained nitride semiconductors have been studied intensively for lasers and LEDs [24], power electronics [25], thermoelectricity [26], solar cells [27], terahertz photonics [28] and high frequency electronic devices [29] due its higher lifetimes of nitride semiconductor materials [23]. Moreover, strained laser structure provides lower threshold current, better temperature performance and higher speed. Due to the strain, valence subbands are rearrange among themselves. Like for compressive strain HH (heavy hole) valence subband goes above the LH (light hole) and for tensile strain opposite arrangement is occurred. Generally compressive strain gives TE polarization when tensile gives TM polarization. In case of strain, only 10% lattice mismatch is allowed otherwise dislocations will form and makes serious strain relaxations. Most of studies of nitride based quantum well structures cover a wide wavelength range from Infra-red to ultra violet due to their successful applications in numerous optoelectronic devices. For designing the nitride based quantum well semiconductor lasers and LEDs, intersubband device structures along with interband device structures are mostly studied. Most of the studies are performed for the wavelength range from infra-red to ultraviolet. Design of interband structures are hardly proposed above these wavelength range in recent published works. Above this range, 1330nm and 1550nm are the most popular wavelengths. In modern optical communication, these wavelengths are mainly used for short distance and long distance communication respectively due to lowest dispersion and lowest path loss of a signal [30]. In this work, a wurtzite-strained nitride based quantum well laser structure, an interband optoelectronic device structure has been proposed and characterized at 1330nm wavelength. After characterization of the structure, optoelectronic characteristics has been optimized using a genetic algorithm based optimization tool. For attaining the desired wavelength range, InN is used as the quantum well (QW) material along with InGaN barriers material [31]. Here, GaN has been used as separate confinement heterostructure (SCH)

for providing better electrical and optical confinement. For the analysis of electronic properties of the proposed structure, the calculation of the band energy has been performed by solving single band effective mass equation for conduction band and by solving the 6×6 $k.p$ Hamiltonian for valence band [32][33]. And for obtaining the optical properties including optical gain, spontaneous emission spectrum etc. a developed simulation model has been performed. To optimize the optical gain and spontaneous emission rate, genetic algorithms, a technique inspired by biological evolution [34], has been utilized by varying the physical parameters of the structure. Therefore, the objectives and aims of the thesis are:

- To design a wurtzite-strained nitride semiconductor based quantum well laser structure at around 1330nm wavelength.
- To develop a $k.p$ method based simulation model to determine the band structure for any wurtzite-strained nitride semiconductor based quantum well lasers.
- To develop a simulation model to obtain the optical characteristics of any quantum well laser structure.
- To perform the simulation models to obtain the laser characteristics for the laser structure.
- To optimize the attained characteristics using Genetic Algorithm based optimization tool.

1.6 Organization of The Thesis

Chapter One of the thesis introduces the topic of the thesis. Historical background of the thesis work is described in this chapter chronologically. The motivation behind this thesis work is also written in this chapter. An outline of the specific objectives of the work is also included.

Chapter Two presents the theoretical aspects of a generalized laser structure as well as semiconductor laser which is extended to wurtzite strained nitride semiconductor laser. All relevant terminologies about the designed laser are presented elaborately in this chapter. Design parameters and process as well as analysis process for the designed laser are also illustrate in this chapter.

Chapter Three illustrates the mathematical model for the proposed laser structure. In this section, model for characterization of both electronic and optical properties is also presented along with the optimization model for the structure.

Chapter Four presents the validation of the developed numerical model with selection of the material for the structure. **Chapter Five** represents the analysis of the performed results. The summary of the simulation performance and comparison of performance with other published works are demonstrated in this chapter with figures and results obtained from the simulation.

Chapter Six briefly summarizes the overall research work and highlights some scopes of future work related to this work.

Chapter Two

Background Physics

2.1 Principle of Operation of a Laser

A laser is an optical frequency oscillator constructed from an optical frequency amplifier with positive feedback. Light waves, which are amplified in passing through the amplifier, are returned through the amplifier by the reflectors and grow in intensity. This intensity growth does not continue indefinitely because the amplifier saturates. The arrangement of mirrors (and sometimes other components) that provides the feedback is generally referred to as the laser cavity or resonator [35]. The function of a laser can be illustrated with an analogy of the light from a bulb. Normally, a burning bulb radiates light in all directions, and therefore illuminates various objects equally if they are equidistant from the source. A laser takes light that would normally be emitted in all directions, such as from a source, and concentrates that light into a single direction. Thus, if the light radiating in all directions from a bulb were concentrated into a single beam of the diameter of the pupil of human eye (approximately of 3 mm), and if a person was standing at a distance of 1 m from the bulb, then the light intensity would be 1,000,000 times as bright as the light that a person normally see radiating from the bulb. That is essentially the underlying concept of the operation of a laser [36].

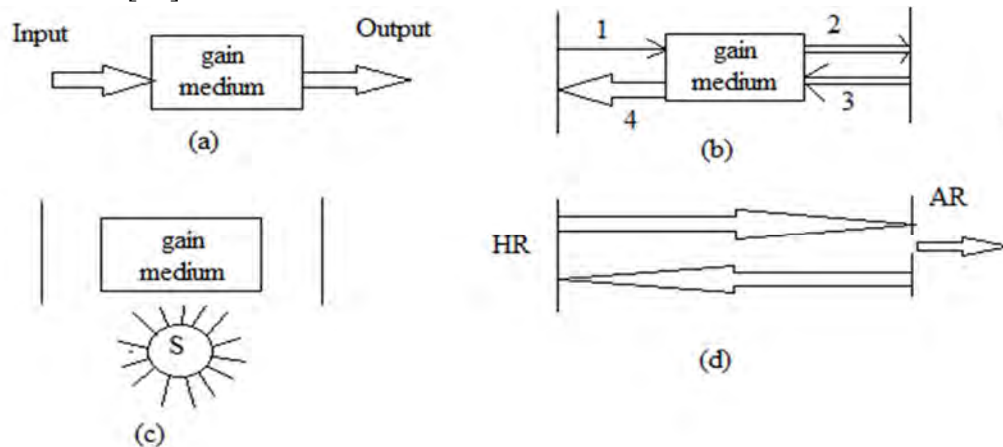


Figure 2.1: Schematic diagrams illustrating fundamental concept of a laser. (a) Gain medium with optical input and output, (b) increase in gain in a round-trip through gain medium, (c) gain medium with permanent optical source, and (d) optical output through anti-reflecting facet of the laser [36].

The simple laser action can be illustrated with Figure 2.1, which illustrates the four key elements of a laser. First, a collection of atoms or other material generates and amplifies a light signal directed through it. The amplifying material is usually enclosed by a highly reflecting cavity that will hold the amplified light, in effect redirecting it through the medium for repeated amplifications. Some provision must be made for replenishing the energy of the amplifier that is being converted to light energy. And some means must be arranged for extracting in the form of a light beam at least part of the light stored in the cavity [21]. The essential elements of a laser

device, as shown in Figure 2.2, are thus: (i) a laser medium consisting of an appropriate collection of atoms, molecules, ions, or in some instances a semiconducting crystal; (ii) a pumping process to excite these atoms into higher quantum-mechanical energy levels; and (iii) suitable optical feedback elements that allow a beam of radiation to either pass once through the laser medium (in a laser amplifier) or bounce back and forth repeatedly through the laser medium (in an oscillator).

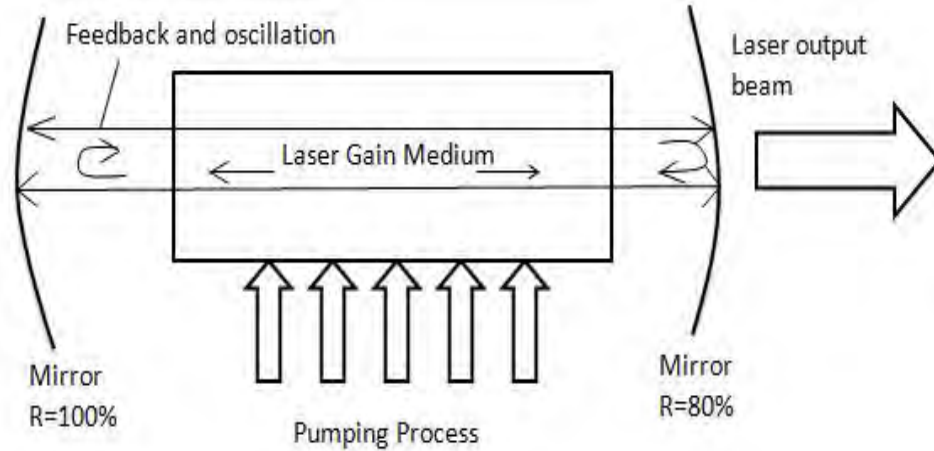


Figure 2.2: Integral Parts of a typical laser oscillator showing the laser gain medium, the mirrors of the cavity, energy pumping towards the medium and coming output of the laser beam from one of the mirror [36].

In laser system, laser gain indicates the net increase in number of photons with the transition energy. Gain is measured by the percentage of increase in photons per pass through the laser gain medium. To obtain the higher gain in lasing action, selecting proper material for gain medium is one of the most important factors in laser system. Other factors are population inversion, pumping process and feedback system whose are discussed at later sections.

2.1.1 Matter-Energy Interaction

Generally, there are three types of matter-energy interaction that occur in each atom of the material: spontaneous emission, stimulated emission and absorption. These correspond to the changes in the energy state of an atom being accompanied by the absorption or emission of a photon whose energy corresponds to the change in the atom's energy state. The first requirement on the laser material is that its atoms have an energy structure in which the decay between two energy states is accompanied by the emission of a radiated photon in the optical spectrum. The frequency of the photon is [36]:

$$\nu = \frac{E_2 - E_1}{h}, \quad (2.1)$$

where, E_1 and E_2 are atomic energy levels and h is Planck's constant. The interactions are illustrated in Figure 2.3 and is described as follows [1]:

- (i) Spontaneous emission occurs when the decay of an excited atom to a lower energy state results in the release of an electromagnetic wave of random phase and direction.
- (ii) Stimulated emission occurs when a photon incident on an excited atom forces it to release an identical photon of matching phase and direction resulting in two photons, the exciting photon and the emitted photon.
- (iii) Absorption occurs when a photon is absorbed by an atom, raising the atom to a higher energy state.

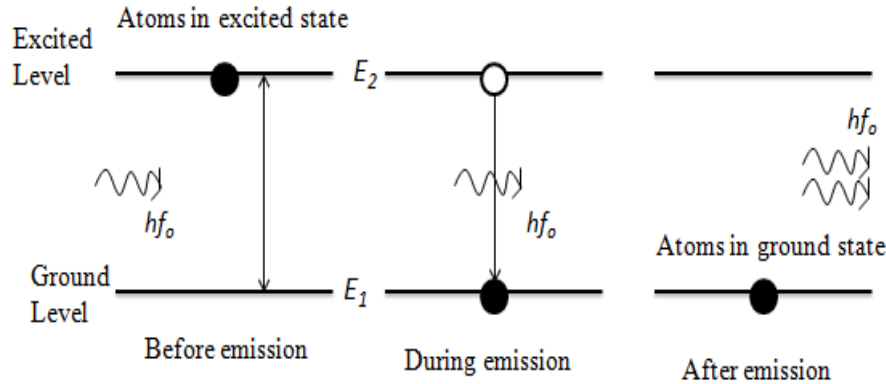


Figure 2.3: Illustrative diagrams of the three matter-energy interaction mechanisms (a) stimulated emission, (b) spontaneous emission, and (c) absorption [36].

For a wave travelling through a material, stimulated emission acts as an optical amplifier via a cascade of coherent photons travelling in the same direction. Spontaneous emission acts as a source of noise on the amplifier since the emitted wave is independent of any incident wave and the surrounding atoms. It also has the undesirable effect of removing potential excited atoms from the stimulated emission process. Absorption is naturally a loss mechanism, removing photons from the amplification process [3], [21-23], and [37].

2.1.2 Pumping Process and Population Inversion

Stimulated emission must be the dominant matter-energy interaction for optical gain to occur. The matter-energy interactions are governed probabilistically, and a high probability of stimulated emission requires that atoms be in the higher energy state and that incident photons are present to seed the stimulated emission. The situation in which the majority of atoms are excited is referred to as a population inversion; this is an unnatural situation under ordinary conditions. Materials naturally lie in thermal equilibrium, meaning that increasing energy states are less populated than the lower energy states. The transition cross sections for absorption and for stimulated emission must then be the same (for any given wavelength), and net gain can occur only when the population inversion is attained. The transition conditions are illustrated through the following Figure 2.4.

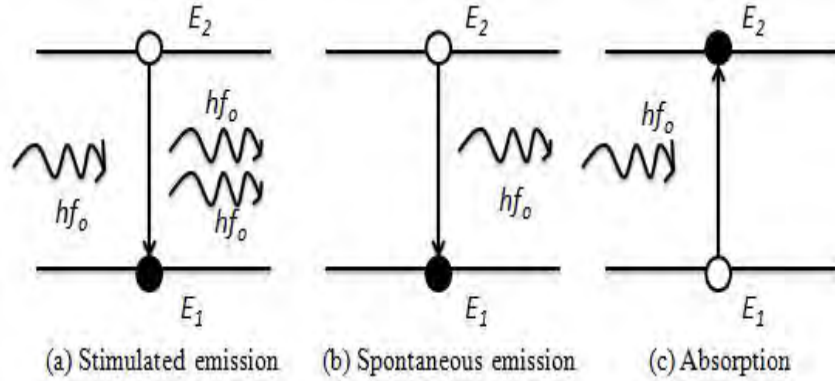


Figure 2.4: Illustrative diagrams showing the stimulated matter-energy interaction mechanisms [36-37].

Population inversion is a state which deviates from thermal equilibrium: in thermal equilibrium, the population of the lower level is always higher, and net gain can never occur. Formally, population inversion is sometimes described as a state with a negative temperature. It is achieved by pumping process which may be electrical or optical.

A pumping process is that required to excite the atoms into their higher quantum-mechanical energy levels. It is a way to invert the laser medium to cause spontaneous and stimulated emission. There are two types of pumping: three and four-level pumping shown in Figure 2.5. Two level pumping suffers from de-excitation of species from upper level to lower level during the process. In three and four level system, there is a meta-stable level where the species are stayed a lit bit longer time as they have a tendency to radiate back to lower energy level. So, effective radiation occurs between the intermediate energy levels [22].

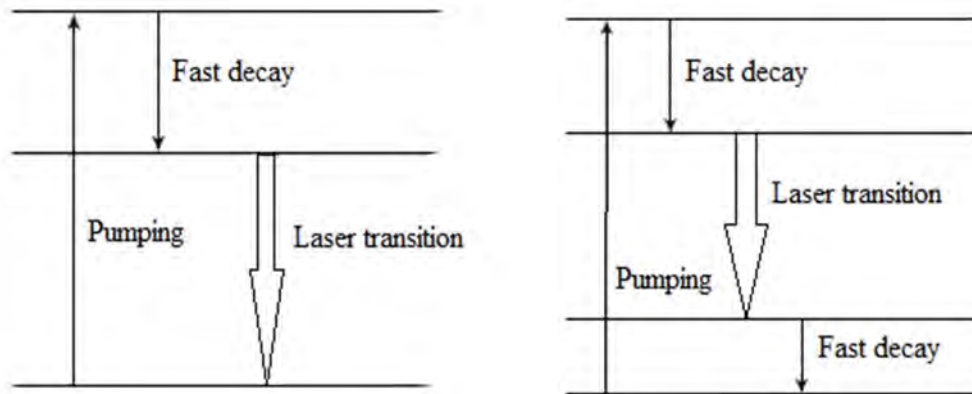


Figure 2.5: Three and four level lasing system showing the pumping and decay system [22].

Besides the optical and electrical pumping process, chemical pumping process is also used for population inversion. This process is suitable for gas laser where gas mixtures are highly reactive and explosive. Electrical pumping is used for gas and semiconductor lasers while optical pumping is used for solid state and liquid lasers.

2.1.3 Optical Feedback System

In order for stimulated emission to dominate, incident photons must initiate the process, which introduces the final requirement for lasing: the positive optical feedback. By placing reflective surfaces at the ends of the material, photons will be reflected back and forth along the cavity, forcing the excited atoms to decay via stimulated emission. Since the reflective surfaces are parallel to one another, the positive feedback causes dominant wave amplification along the normal axis, hence the directional beam characteristic of lasers. Furthermore, the feedback increases utilization of the gain within the cavity [21].

A laser with a positive-feedback system, in theory could amplify itself to infinity, but practically cavity losses limit the positive feedback and the degree of amplification. Making one of the ends partially reflective allows the transmission of a proportion of the propagating wave as the laser beam. If the round-trip laser gain minus mirror losses is less than unity, this radiation will decrease in intensity on each pass, and will die away after a few bounces. But, if the total round-trip gain, including laser gain and mirror losses, is greater than unity, this noise radiation will build up in amplitude exponentially on each successive round trip; and will eventually grow into a coherent self-sustained oscillation inside the laser cavity formed by the two end mirrors. The threshold condition for the build-up of laser oscillation is thus that the total round-trip gain or net laser gain minus net cavity and coupling losses—must have a magnitude greater than unity [21].

Net gain greater than net loss for a circulating wave thus leads to signal build-up at the transition frequency within the laser cavity. This exponential growth will continue until the signal amplitude becomes sufficiently large that it begins to "burn up" some of the population inversion, and partially saturate the laser gain. Steady-state oscillation within a laser cavity, just as in any other steady-state oscillator, then requires that net gain just exactly equal net losses, or that the total round-trip gain exactly equal unity, so that the re-circulating signal neither grows nor decays on each round trip, but stays constant in amplitude. Figure 2.1(b) and 2.2 illustrates that a small amount of spontaneous emission at lasing frequency starts a round-trip through laser medium and amplifies by a small amount. This radiation again reflects from one end mirror and passes through the medium for further amplification.

2.2 General Theory of a Diode Laser

According to semiconductor physics, in the crystal semiconductor materials show three distinct energy bands which are known as conduction, valance and forbidden energy band. Transition of an electron can take place in semiconductor between conduction band to valance band and vice versa. In this transition, radiation of energy takes place but it is of two natures: radiative and non-radiative shown in Figure 2.6. For laser, radiative emission is needed which can only found from direct band gap material (means the maxima of valance band and the minima of conduction band are situated in same k). Usual elemental semiconductors have indirect band gaps [3], [21].

Hence compounds formed by the combination of elements from the third and fifth groups of the Periodic Table, referred to as III-V compounds, are usually used. Common laser materials are GaAs, AlGaAs, InGaAs and InGaAsP depending upon the desired lasing wavelength. More recently, III-nitride compounds such as GaN/AlGaIn and InGaIn/AlGaIn have been used to achieve emission in the blue and ultraviolet regions. In semiconductor devices, when an electric field is applied, current in a diode laser is carried by electrons in conduction band, and by holes in valence band within the crystal lattice. The semiconductor is doped with impurities to control the type and density of current carriers. It is sometimes called a junction laser because of the junction or an injection laser to describe the process of current injection. Application of forward biasing in p-n junction create population inversion between two bands; it lowers internal potential barriers and causes carrier injection from one side of the junction to the other. At the junction, excess electrons fall to lower energy states, i.e., holes in the valence band. Figure 2.7 shows the process, called electron-hole recombination. The electrical result of forward-biasing a semiconductor diode is current flow, with the recombination of electrons and holes releasing energy at the junction. In silicon diodes, most energy is released as heat, and no light is produced. In LEDs and diode lasers, much of the energy is released as photons with energy roughly equivalent to the band gap—the energy difference between the conduction and valence bands—as shown in Figure 2.6 [3].

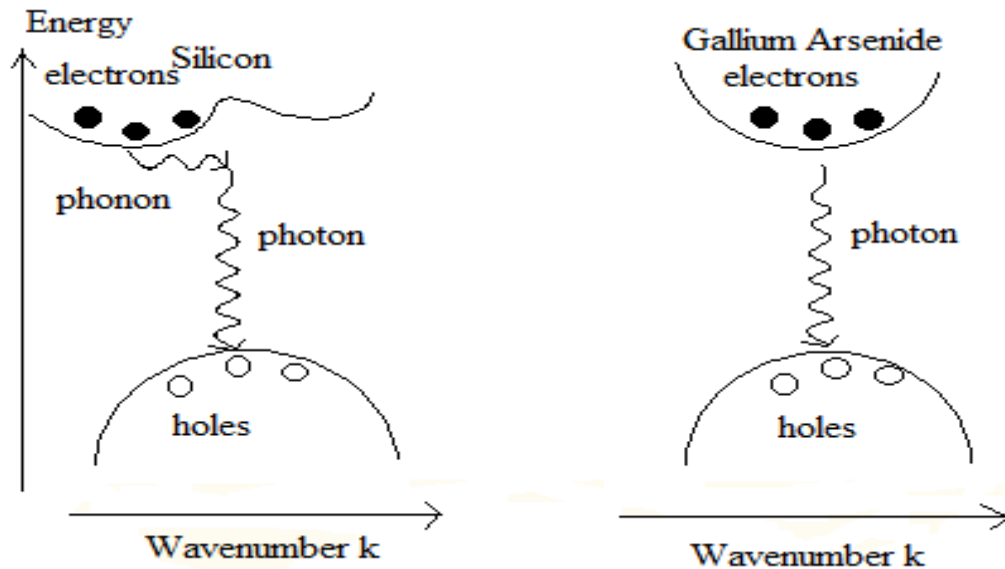


Figure 2.6: Plot of energy vs. wavenumber for direct and indirect band gap materials showing the emission of photon and phonon [3].

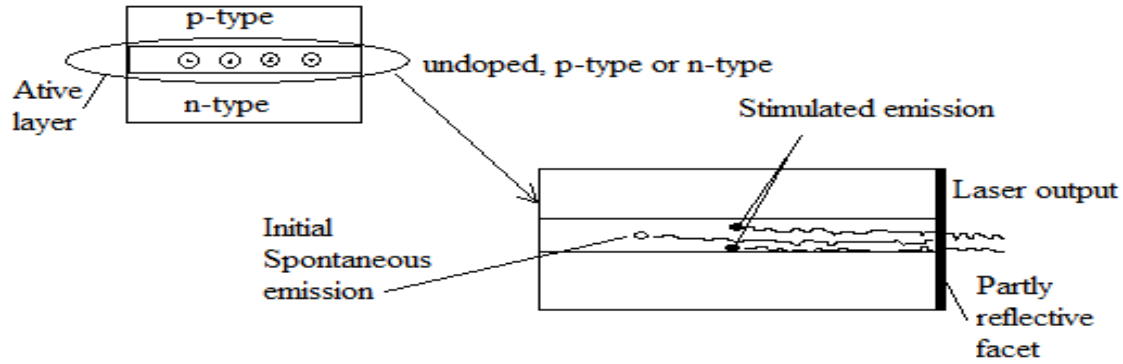


Figure 2.7: Diode laser structures showing emission process in active region [3].

A diode laser will produce stimulated emission only if enough current is passing through the junction to produce a population inversion. This is called threshold current. It is a figure of merit for diode lasers; the lower the threshold current, the less energy is dissipated in the device and the higher its efficiency. The critical physical parameter is the current density, measured in amperes per square centimeter of junction area. If the current density is below the threshold, a diode laser functions like an LED, producing spontaneous emission. Threshold current usually is defined by extrapolating the linear part of the laser output-vs.-current curve back zero-output line [37].

Simple consideration concerning carrier statistics shows that an important requirement to obtain population inversion is that the forward bias voltage V must satisfy [21]

$$eV > \hbar\omega \quad (2.2)$$

The two key elements needed to produce stimulated emission from a diode laser are a population inversion and optical feedback. The optical feedback comes from reflective structures which form the diode laser resonator. In traditional edge emitting diode lasers, facets cut on each end of the active junction layer reflect light back into the cavity [21], [37]. The band gap depends on the crystalline structure and chemical composition of the semiconductor material, so diode laser wavelengths depend on their composition [38]. Only part of the electrical energy used by a diode laser emerges in the laser beam; the rest is dissipated as heat. The need to minimize and remove this waste heat constrains diode laser operation, particularly because operating characteristics degrade as temperature increases. Heat dissipation once was so severe problem that early diode lasers were limited to pulsed and/or low-temperature operation. Great improvements have made semiconductor lasers the most efficient types available, leading to much higher output powers and shorter wavelengths, but heat dissipation remains an important consideration. In comparison with other categories of lasers, semiconductor injection lasers offer the following advantages. These are as bellow [3].

- (i) Semiconductor lasers are extremely compact and of light weight even with heat sink and power supply to drive the laser.
- (ii) The semiconductor lasers can be driven by the injection of a current in milli-ampere range with few voltages. The conversion efficiency from electrical energy to optical energy is much higher here.
- (iii) Many semiconductor lasers can oscillate continuously at or near room temperature.
- (iv) By choosing appropriate materials and composition, it can produce wide ranges of light form infrared to whole visible regions.
- (v) It has a wide range of gain bandwidth.
- (vi) It can produce ultra-short pulse of sub nanosecond to picoseconds range.

Despite of its huge advantages, it suffers from some important drawbacks. These are [3]:

- (i) Semiconductor lasers are very sensitive to temperature. With the change of temperature, the wavelength, threshold current and optical power also changes.
- (ii) The lasers utilize high-density carriers, and therefore fluctuation in the carrier density affects the refractive index of the active region. Since the lasers have a short resonator length and use facet mirrors of low reflectivity, the oscillation is affected sensitively by perturbations caused by external feedback. As a result, semiconductor lasers often involve various noise and instability problems.

The light come out of the laser are suffered from divergence problem. External mirror is needed to obtain the collimated beam.

2.3 Different Structures of a Diode Laser

A diode laser is usually make in p-i-n structure where an intrinsic bulk semiconductor is sandwiched between an n and a p type semiconductor material with nearly matched lattice constant. In practice, the structure contains additional layers for some advantages. These layers usually are sandwiched between other layers of different composition to improve its operation. Diode lasers have both in-plane and vertical plane structures with respect to light plane. Gain in semiconductor lasers is very high, so only a small length of active medium is needed. Typical edge-emitting laser chips have active layers about 500 μm long, and virtually all are within a factor of 3 of that length. High-speed edge emitters may be as small as 50 to 100 μm . The active layers normally are under 1 μm thick, but considerably wider [3].

Diode laser fabrication starts with a substrate of a binary semiconductor (usually GaAs or InP) with a controlled impurity level. Additional layers may be formed by diffusing different impurities into selected areas of the substrate surface. Typically, layers are formed by epitaxial growth of new material on top of the substrate (which itself may be etched in selected regions to control the geometries of the added layers). Various epitaxial growth techniques allow the deposition of extremely thin layers of precise geometry, with each layer having a distinct composition. The

combination of multiple layers and surface patterns controls current flow, guides laser light, and produces laser oscillation. The two end facets of the laser chip are polished or cleaved to form a smooth surface that reflects some light back into the semiconductor [3], [36]. In diode laser, for efficient operation it is important to confine the light to the active layer where carriers combine to emit light. So, different structures are developed for better confinement of light to the active region. Two major classes of diode lasers are defined by the compositions of the layers adjacent to the active layer [3], [21], [36].

2.3.1 Homojunction Diode Lasers

These are made entirely of a single semiconductor compound, typically GaAs, with different doping at different parts. The junction layer is the interface between n - and p -doped regions of the same material. This structure was used in the first diode lasers, but it provided little vertical confinement of the laser light. This makes it so inefficient that it can operate only in pulsed mode with cryogenic cooling, so it is no longer used.

2.3.2 Heterojunction Laser

The recent progress in modern crystal growth techniques such as molecular beam epitaxy (MBE) and metal-organic chemical vapor deposition (MOCVD), has demonstrated that it is possible to grow semiconductors of different atomic compositions on top of another semiconductor substrate with monolayer precision. This opens up extremely exciting possibilities of the so-called "band-gap engineering" [53]. For example, aluminum arsenide (AlAs) has a similar lattice constant as gallium arsenide (GaAs). We can grow a few atomic layers of AlAs on top of a gallium arsenide substrate, then grow alternate layers of GaAs and AlAs. We can also grow a ternary compound such as $\text{Al}_x\text{Ga}_{1-x}\text{As}$ (where the aluminum mole fraction x can be between 0 and 1) on a GaAs substrate and form a heterojunction (Figure 2.8). Interesting applications have been found using heterojunction structures. For example, when the wide-gap $\text{Al}_x\text{Ga}_{1-x}\text{As}$ is doped by donors, the free electrons from the ionized donor tend to fall to the conduction band of the GaAs region because of the lower potential energy on that side; the band diagram is shown in Figure 2.8. An applied field in a direction parallel to the junction interface will create a conduction current. Since these electrons conduct in a channel on the GaAs region, which is undoped, the amount of impurity scatterings can be reduced. Therefore, the electron mobility can be enhanced.

For optoelectronic device applications, heterojunction structures play important roles. For example, when semiconductor lasers were invented, they had to be cooled down to cryogenic temperature (77 K), and the lasers could lase only in a pulsed mode. These lasers had large threshold current densities, which means that a large amount of current has to be injected before the lasers could start lasing. With the introduction of the heterojunction semiconductor lasers, the concept of carrier and photon confinements makes room temperature cw operation possible, because the electrons and holes, once injected by the electrodes on both sides of the wide-band gap p - n regions, will be confined in the central GaAs region where the band gap is smaller,

resulting in a smaller potential energy for the electrons in the conduction band as well as a smaller potential energy for holes in the valence band. Note that the energy for the holes is measured downward, which is opposite to that of the electrons. For the photons, it turns out that the optical refractive index of the narrow band-gap material (GaAs) is larger than that of the wide-band gap material ($\text{Al}_x\text{Ga}_{1-x}\text{As}$). Therefore, the photons can be confined in the active region as well. This double confinement of both carriers and photons makes the stimulated emission process more efficient and leads to the room-temperature operation of laser diodes.

The control of the mole fractions of different atoms also makes the band-gap engineering extremely exciting. For example, by controlling the mole fraction of gallium and indium in an $\text{In}_{1-x}\text{Ga}_x\text{As}$ material, a wide tunable range of band gap is possible since InAs has a 0.354 eV band gap and GaAs has a 1.424 eV band gap at room temperature. At $x=0.47$, the $\text{In}_{1-x}\text{Ga}_x\text{As}$ alloy has a band gap of 0.75 eV and is lattice-matched to the InP substrate. The lattice constant of the ternary alloy has a linear dependence on the mole fraction [38]:

$$a(A_xB_{1-x}C) = xa(AC) + (1 - x)a(BC), \quad (2.3)$$

where $a(AB)$ is the lattice constant of the binary compound AB and $a(BC)$ is that of the compound BC. This linear interpolation formula works very well for the lattice constant, but not for the band gap. For the band-gap dependence, a quadratic dependence on the mole fraction x is usually required [38]. For $\text{Al}_x\text{Ga}_{1-x}\text{As}$ ternary compounds with $0 \leq x < 0.4$, the following linear formula is commonly used at room temperature [38]:

$$E_g(\text{Al}_x\text{Ga}_{1-x}\text{As}) = 1.424 + 1.247x. \quad (2.4)$$

Most ternary compounds require a quadratic term. From the above formula, we can calculate the conduction and valence band-edge discontinuities of a heterojunction.

- (i) **Single-heterojunction lasers:** In these lasers shown in Figure 2.8, the active layer is sandwiched between two layers of different composition, which have different band gaps. The refractive index difference helps confine the light to the active layer, giving single-heterojunction lasers much better performance than homojunction lasers. Single-heterojunction lasers can produce pulses with high peak power at room temperature. However, they cannot operate continuously or at high duty cycles.
- (ii) **Double-heterojunction lasers:** In these lasers shown in Figure 2.8, the active layers are sandwiched between two layers of different material. This confines the laser light on both top and bottom of the active layer, making double-heterojunction lasers much more efficient than single-heterojunction types. The double-heterojunction diode laser was the first type capable of continuous operation at room temperature, and it has become the prevalent type for most applications.

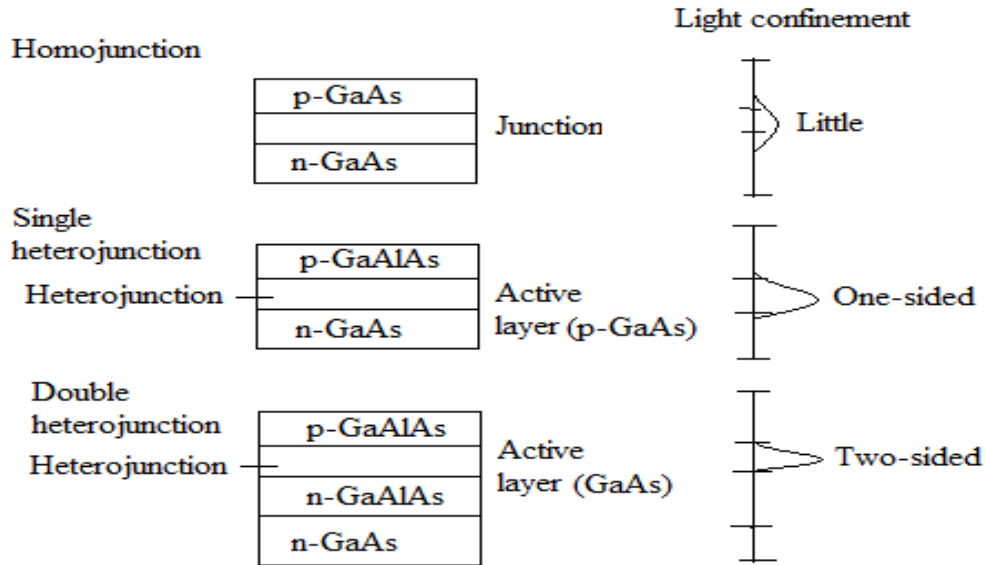


Figure 2.8: Major categories of edge-emitting diode lasers with their different layers and corresponding materials. Three structures are shown with their respective light confinement [1], [36].

2.3.3 Double Heterostructure Laser

The first oscillation of injection lasers was obtained in a p–n junction structure consisting of single-crystal material GaAs, a diode with a homo-structure. The laser, however, required current injection of a very large density (greater than 50 kA/cm^2) for lasing, and therefore lasing was limited to pulse oscillation at low temperatures. Continuous oscillation at room temperature and practical performances were accomplished in lasers of double hetero-structure (DH). Nowadays, semiconductor lasers usually mean DH lasers. The structure is schematically illustrated in Figure 2.9 following. The structure is fabricated by multilayer epitaxial on a substrate. The DH structure offers two functions that are very effective for reduction in the current required for laser operation. The first is carrier confinement. As shown in Figure 2.9, the difference in the bandgap energy gives rise to formation of barriers in electron potential, and therefore the injected carriers are confined within the active layer at high densities without diffusion from the junctions. Thus the population inversion required for light amplification can be accomplished with current injection of relatively small density (about 1 kA/cm^2). The second function is optical waveguiding. The cladding layers with larger bandgap energy are almost transparent for optical wavelengths where amplification is obtained in the active layer and the refractive index of the cladding layers is lower than that of the active layer, as shown in Figure 2.9.

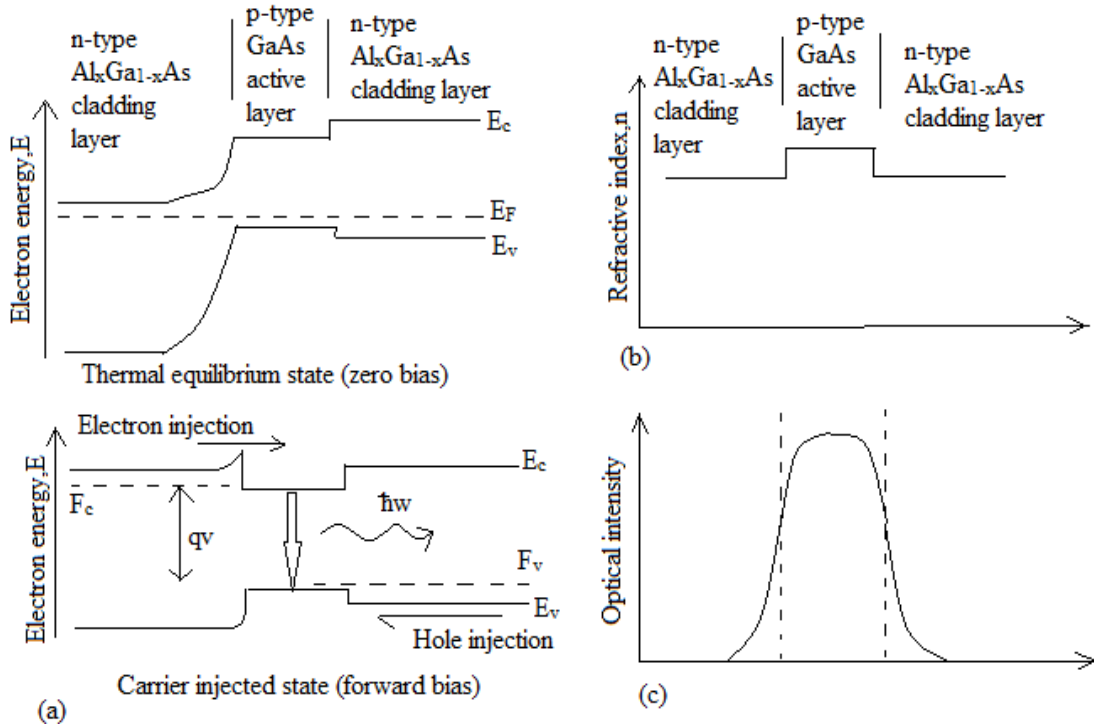


Figure 2.9: Confinement of carriers and optical wave in a DH semiconductor laser. (a) Energy band diagram, (b) refractive index distribution, and (c) optical intensity distribution [36].

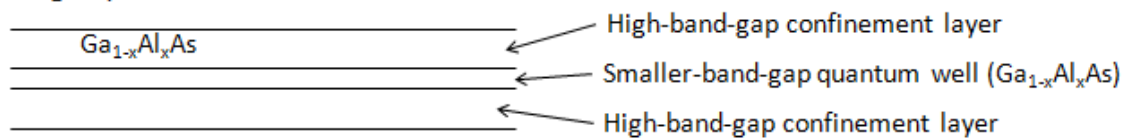
Accordingly, the optical wave is confined in the high index active layer through successive total internal reflection at the interfaces with the cladding layers and propagates along the plane of the active layer. The DH laser therefore has a room temperature threshold current density two orders of magnitude smaller than the homojunction device [3].

2.3.4 Quantum Well Lasers

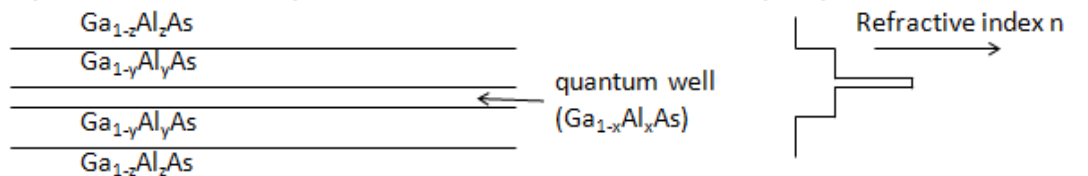
When very thin layers of heterojunction structures are grown with a layer thickness thinner than the coherent length of the conduction band electrons, quantum size effects occur. These include the quantization of the subband energies with corresponding wave-functions (Figure 2.10). The success in the growth of quantum-well structures makes a study of the introductory quantum physics realizable in these man-made semiconductor materials. Due to the quasi-two-dimensional confinement of electrons and holes in the quantum wells, many electronic and optical properties of these structures differ significantly from those of the bulk materials. Many interesting quantum mechanical phenomena using quantum-well structures and their applications have been predicted and confirmed experimentally [8]. For a simple quantum-well potential, we have the well model. These quantized energy levels appear in the optical absorption and gain spectra with exciting applications to electro-absorption modulators, quantum well lasers, and photodetectors. Enhanced absorption occurs when the optical energy is close to the difference between the conduction and hole subband levels. The density of states in the quasi-two dimensional structure is also different from that of bulk semiconductor. A significant discovery is that room temperature observation of

these quantum mechanical phenomena can be observed. When an electric field is applied through the quantum-well region using a diode structure, the potential profiles are tilted and the positions of the quantized subbands are shifted. Therefore, the optical absorption spectrum can be changed

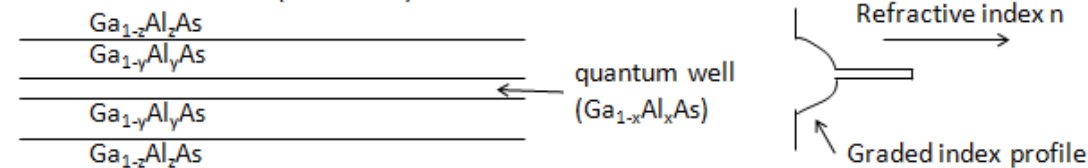
Single quantum well



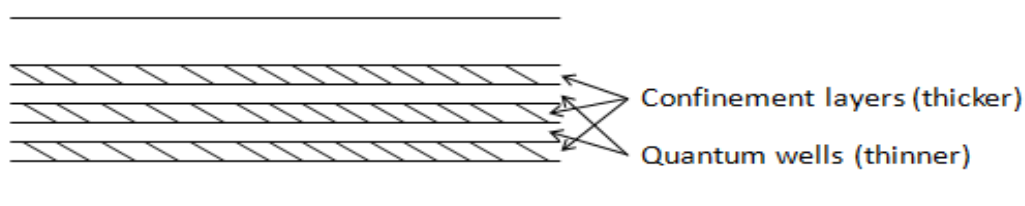
Separate carrier and optical confinement heterostructure (SCH)



Graded-index SCH (GRINSCH)



Multiple quantum well hetero-structure



by an electric field bias. This makes

practical applications of electro-absorption modulators using these quantum-well structures.

Figure 2.10: A single quantum well (top) is surrounded by thicker layers of higher Bandgap material. Forming layers with lower refractive index on top and bottom produces a separate carrier and optical confinement heterostructure (SCH). Grading the refractive index of the confinement layer produces the graded-index and separate carrier and optical confinement heterostructure (GRINSCH) laser. Multiple quantum wells also can be stacked in the active layer, as shown at bottom [1].

With the invention of double hetero-structure lasers, light confinement problem was reduced greatly. But carrier's confinement factor was not yet improved so much. Moreover, to increase the

differential gain and reducing temperature dependence on gain more improvement was done on active region. Quantum well laser was the most possible solution of these existing problems [3]. Basically, the role of the hetero-structure in the early lasers was described as providing a barrier that blocked the diffusion of electrons. The hetero-structure acts as a potential well for electrons in the conduction band and holes in the valence band. Laser scientists then did experiment on the thickness of active layer. They first pointed out that threshold current could be reduced by introducing separate layers for optical confinement. Increased differential gain is also achieved along with reduced temperature dependence of the gain. The thinness of the QW layer means that it cannot effectively confine the beam. The figures of different kinds of quantum well lasers are illustrated in Figure 2.10 [3], [21].

2.3.5 Separate Confinement Heterostructure

The problem with the simple quantum well diode described above is that the thin layer is simply too small to effectively confine the light. To compensate the confinement problem, extra semiconductor layers with lower refractive index layers than the center three are added to confine the light. This is referred to as a separate confinement hetero-structure (SCH) laser diode. This is used for better confinement of light in active region. These layers adjacent to the quantum-well structure confine the laser light vertically. In the design of a separate confinement hetero-structure (SCH), the layers adjacent to the quantum well have a refractive index intermediate between that of the quantum well and the surrounding material, forming a waveguide. Alternatively, the refractive indexes of the surrounding layers may be graded forming a graded-index. Separate confinement hetero-structure also provides better carrier confinement. Almost all commercial laser diodes produced since the 1990s have been of this type. The entire laser diodes investigated under the Ultra-bright project was SCH lasers [3], [21].

2.3.6 Multiple Quantum Well Lasers

Multiple quantum well lasers (shown in Figure 2.10) are promising candidates for use in high speed integrated optics and optical communications because of its significant superiority in performance over conventional DH structures. This MQW provides better carrier and photon confinement in active region than single quantum well (SQW) laser. As a result, MQW lasers provide better performance than SQW lasers. Performance of MQW is varied with the number of wells as well as thickness of the well. Barrier regions are used in between the consecutive wells. The band offset of the barrier and quantum well region create the barrier height for the carriers. The index profile provides the light confinement. The advantages are of MQW over bulk and SQW laser as bellow [3], [21].

- (i) Provides good confinement
- (ii) Strain hetero-junction can be made for bandwidth modulation
- (iii) Optical loss is lower than the two
- (iv) Number of modes are lower than two

- (v) Dispersion lower
- (vi) Low threshold current

2.4 Long Wavelength Semiconductor Laser

Semiconductor diode lasers with wavelengths longer than 1.1 micrometers (μm) are used primarily for fiber-optic communications because of their high bit rate with respect to the distance. The comparison between laser used in communication and other systems is showed at the Table 2.1. Lasers for communication purpose can be made at a broad range of wavelengths but most work has concentrated on two windows of silica optical fibers: 1.31 μm , where step-index single-mode fibers have zero wavelength dispersion and loss of about 0.5 decibel per kilometer (dB/km), and 1.55 μm , where silica fibers have their lowest loss, about 0.15 dB/km. InGaAsP lasers have been designed with properties such as high modulation bandwidth and narrow spectral linewidth needed for high performance long-distance fiber-optic systems [21].

Table 2.1: Different communication system with their respective bit rates

System	Bit rate distance product (bit/s)-km
Old optical communication	1
Telegraph	10
Telephone	10^3
Coaxial Cable	10^5
Microwaves	10^6
Laser light in open air	10^9

In communication system, long wavelength semiconductor lasers are coupled with optical fiber. Typically, lasers are used to produce the single frequency signal with low path loss and dispersion given in Figure 2.11. From that point of view, laser of 1330 nm and 1550 nm wavelength are the significant laser for communication purpose.

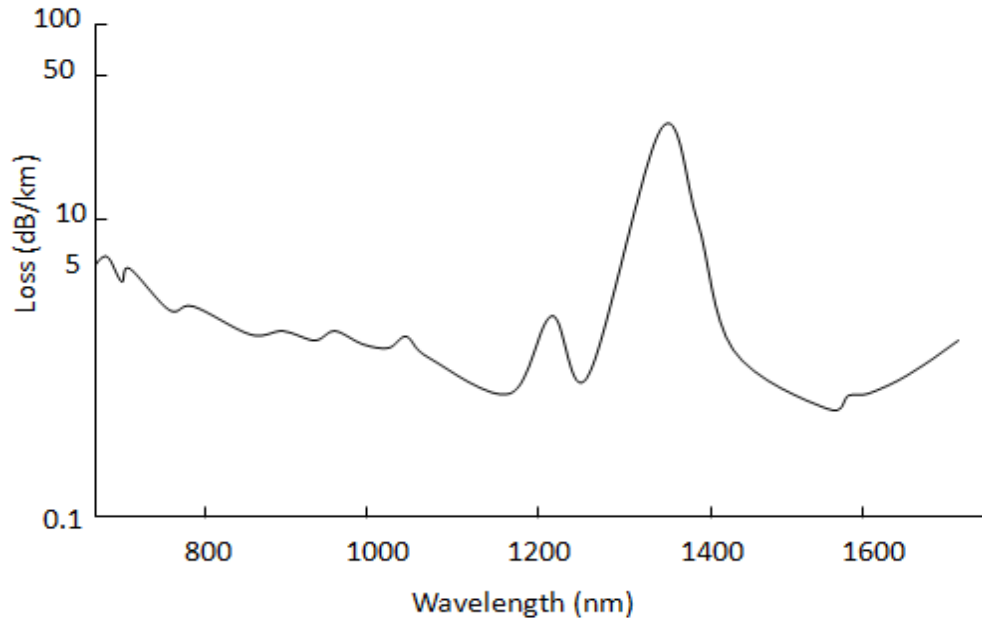


Figure 2.11: Plot of path loss (dB/km) vs. wavelength produced by the laser structure. Figure shows the minima region at around 1550 nm range [1], [21].

2.5 Nitride Semiconductor Laser/LED

The III-nitride semiconductors are presently of high interest for optoelectronic device applications such as laser diodes (LDs) in the blue and ultraviolet spectral region. The optimal properties of nitride semiconductor is essential for commercial applications and laser design. Now, blue to violet vertical-cavity surface-emitting lasers (VCSELs) based on the nitride system are available. Incorporation of quantum dots (QDs) as active medium in LDs and VCSELs gives a superior device performance concerning threshold current and temperature stability. On the other hand, LEDs were regarded as a perfect light source for displays because of its high brightness, durability and limited power consumption. Rapid development of the above-mentioned applications increased the importance of these materials that emit blue light efficiently. Therefore, shifting the energy of laser emission toward higher values was looked forward. Moreover, optical storage systems and display technology were potential application areas whose were even more desirable and profitable from a commercial point of view. The diffraction limit which is inversely proportional to the square of the wavelength and a focusing spot size, gives the conclusion that a shorter wavelength can be focused more sharply. Another benefit from blue-shifting of laser emission is that many biochemical reagents, pollutants and drugs have optimum response frequency in a spectral region covering a wavelength range between 380-490 nm [39]. They can

also be used for light detection in the same spectral band. The majority of efforts are focused on the fabrication of UV and visible light emitters: both lasers and LEDs. The most important and interesting applications of the light emitters include disinfection and sterilization of surfaces and utensils, water disinfection and decontamination, UV curing processes in industry, phototherapy, and medical diagnostics. Three primary colors (red, green and blue) are needed for efficient white-light emitters and for full-color displays or a future type of LD-based TV. III-V compounds such as AlGaAs or GaInP are generally advantageous in the red color range. And, II-VI materials are promising green and blue light emitters. Finally GaN, AlN and InN and their ternaries became the materials of choice for short-wavelength optoelectronics [40]. The room-temperature band gap energy of nitride compounds varies between 0.7 eV for pure InN through 3.4 eV for GaN up to 6.2 eV for AlN and can be easily controlled by alloy composition. This material systems have direct band gap and covers the large spectrum of emission wavelengths from infrared to near ultraviolet. This material systems is also characterized with an excellent thermal conductivity ($1.3 \text{ Wcm}^{-1}\text{K}^{-1}$ for GaN versus $0.55 \text{ Wcm}^{-1}\text{K}^{-1}$ for GaAs) as well as a physical and chemical stability, which are equally important for practical applications.

The first major problem of nitride-related technology was a lack for a proper, lattice-matched substrate for the subsequent deposition of III-nitride compounds. Although GaN was synthesized for the first time, it was extremely difficult to obtain large, high quality bulk GaN crystals due to its thermodynamic properties. III-nitride compounds could not be grown from a stoichiometric melt by the Czochralski or Bridgman methods commonly used in other material systems. Eventually, Sapphire became the most important one, despite the lack of a total compatibility to GaN in terms of a lattice constant and the thermal expansion coefficient. First high quality GaN layers on sapphire were obtained by Hydride Vapor Phase Epitaxy (HVPE). High concentration of electrons in GaN crystals was revealed due to unintentional contamination with oxygen. Therefore, the attempts to achieve p-type conductivity failed. High background electron concentration, passivation of acceptors by hydrogen atoms and a low mobility of holes made it extremely difficult to obtain the net p-type conductivity in GaN. The development of the nitride technology was hampered for almost two decades. During the mid-80's, the development of MOCVD technique marked the next milestone in the nitride technology. The usage of low temperature AlN and GaN buffer layers led to a successful growth of high quality GaN films with mirror-like flat surfaces in spite of a 15% lattice mismatch between a sapphire substrate and GaN. Another breakthrough was achieved by overcoming difficulties with obtaining p-type conductivity in GaN. Unavailability of p-type GaN films hampered the development of nitride-based devices until 1989 when Amano *et al.* obtained p-type GaN films using Mg as an acceptor impurity. Their approach to obtain p-type conductivity from initially highly resistive material was based on post-growth irradiation by a low-energy electron beam (LEEB). The research was followed by a demonstration of the first III-nitride system based p-n junction light emitting diode (LED). From the beginning, Mg was the most promising candidate for an effective acceptor impurity. However, large concentration of dopants was required due to the relatively high ionization energy at room temperature. Additionally, the MOCVD growth of the device structure taking place in ammonia

atmosphere promoted the formation of electrically inactive Mg-H complexes. The origin of the acceptor compensation mechanism was not correctly recognized until Nakamura *et al.* obtained p-type GaN films using post-growth thermal annealing in nitrogen atmosphere instead of ammonia. LEEBI treatment was not necessary anymore. Formation of neutral Mg-H complexes was identified as a major mechanism of acceptor compensation responsible for a resistivity increase of p-type films grown in ammonia atmosphere. The discovery was further confirmed by theoretical calculations by Neugebauer *et al.*.

Further improvement of the MOCVD technique, led to the deposition of a high quality InGaN films designed to form the active region of the blue light emitting devices. Using a novel two-flow MOCVD reactor Nakamura *et al.* managed to grow an InGaN multiple quantum well (MQW) structure with enhanced photoluminescence intensity. This was the starting point for the mass production technology of blue and green light emitting diodes (LEDs) deposited on the sapphire substrate. After optimizing the growth technology and improving a structure design, the first room temperature (RT) pulse-operated LD was demonstrated followed by fabrication of the first III-nitride based LD working in continuous wave (CW) regime. Further improvements concerning a demonstration of strained AlGaIn/GaN superlattices allowing for thicker cladding layers and low defect density GaN substrates achieved by epitaxial lateral overgrowth (ELO) which enabled considerable prolongation of the device's lifetime and led to the successful commercialization of the entire production technology. Unlike the other III-V semiconductors like GaAs or InP, GaN and its alloys are grown mostly in the hexagonal symmetry of wurtzite. Although a zinc-blende structure can be successfully obtained experimentally through the use of cubic substrates like Si or GaAs, its character is metastable and leads to a significantly lower crystal quality. Unfortunately, crystals grown in hexagonal symmetry are subject to strong polarization induced electric fields along c-axis. They are negligible in other III-V compounds crystallizing a zinc blende structure due to the high symmetry of the crystal along [001] nonpolar axis, which defines a growth direction for these materials. In case of the nitrides, the electric fields cannot be ignored.

There are two phenomena inducing material polarization in the wurtzite-symmetry nitrides. The first one originates from an intrinsic asymmetry of the bonding in the equilibrium crystal structure. Lower symmetry of the wurtzite induces a net displacement of the negative charge towards nitrogen along [0001] direction leading to the formation of *spontaneous polarization*. The other component of the internal electric field is induced by a mechanical stress and originates in a lattice mismatch between a GaN substrate and InGaIn-based QWs. As a result of this mismatch, QWs in the active region are subject to compressive biaxial strain induced in a junction plane [41, 42]. In order to retain the volume of a unit cell, additional distortion along c-axis appears leading to *piezoelectric polarization*. Piezoelectric constants are an order of magnitude higher in GaN than in GaAs. Strain modifies the valence-band structure of nitride devices in a way that can negatively affect the emitted light polarization properties. To complicate matters, light emitted from an active multi-quantum-well structure can switch its polarization from transverse electric (TE) to transverse magnetic (TM), depending on the amount of residual strain present in the active layer—which

further depends on the choice of substrate. When the emitted light is TM-polarized, it is difficult to extract along the c-axis (the growth direction). This leads to decreased light-extraction efficiency, and thus lower overall external quantum efficiency (EQE). The total polarization present within a crystal is the sum of the spontaneous polarization and piezoelectric polarization. Electric field induced this way is directed towards Ga-face of a GaN substrate. However, in order to obtain the entire electric field across quantum wells sandwiched between p- and n-type layers of a laser stack, one needs not to forget about a junction electric field which is pointed in opposite direction since n-type layers are deposited on GaN substrate at first. The total amount of internal electric fields range within 1-2 MV/cm for a typical QW In content of less than 10%. This phenomena was shown originally by means of *ab-initio* calculations and was then confirmed by experimental evidence [43].

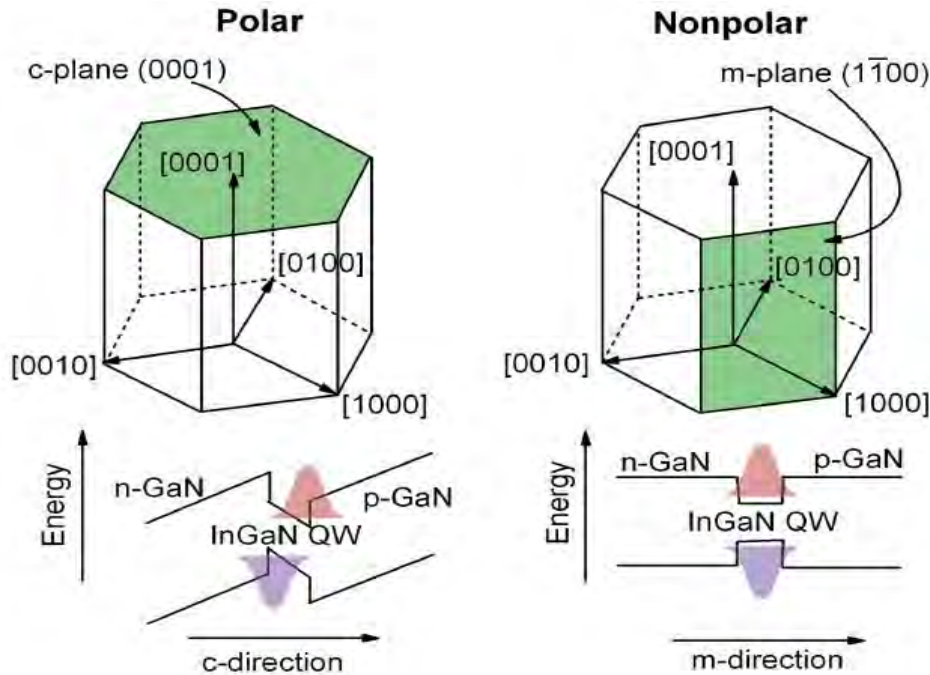


Figure 2.14: Orientation of crystal planes exposed to the epitaxial growth in polar (c-plane) and nonpolar (m-plane) direction with corresponding energy band diagrams and the position of electron and hole wavefunctions [43].

Polarization difference between the adjacent atomic layers implies a net spatial separation of charge. As a result a bound charge appears on each interface. This surface charge is a source of a step-like change in electric field as predicted by the *Gauss law*. The total electric field change across a certain volume of polarized material can be taken into account by summing all contributions across interfaces between atomic layers of different polarity. Presence of the electric field induces a spatial separation of electron and hole envelope wavefunctions towards triangular potential minima at opposite interfaces of a QW (Figure 2.14). Limited spatial overlap results in reduction of oscillator strength which in turn deteriorates radiative recombination rate and consequently optical gain which retards device's performance [44]. It is commonly agreed that internal fields in quantum wells can be efficiently screened either by heavy barrier doping with Si donors or by high carrier injection [45]. Although both conditions are satisfied in case of laser

diodes, the QW thickness is usually kept within an effective Bohr radius a^*_B , which remains in the range of a few nanometers and prevents the reduction of a spatial wavefunction overlap. Apart from spatial separation of charge across quantum wells, large electric fields induce band profile bending that shifts the emission towards lower energy in a current-dependent way and is often referred to as a *quantum confined Stark effect*. The problem internal electric fields becomes more pronounced for active regions comprising of thick InGaN QWs with a high indium content designed for an operation in a blue-green spectral range. For this reason the operation of InGaN laser devices is limited by now to wavelengths shorter than 482nm [46].

The promising way to overcome these limitations is the epitaxial growth along crystallographic directions which reduce $(11\bar{2}2)$ [47] or even totally eliminate internal piezoelectric fields $((1\bar{1}00)$ m-plane [48] or $((11\bar{2}0)$ a-plane [49]). There are, however, some serious challenges that need to be dealt with:

- availability of large-area, low-cost nonpolar and semipolar GaN substrates
- elimination of nonradiative recombination sites
- efficient doping technology taking into account its dependence on the crystal orientation and the growth surface
- Reliability and lifetime of devices grown on different crystal orientations.

The combined impact of a large bandgap energy, high resistivity of p-type layers and p-type contact electrode together with a high density of electronic states require applying high voltage and high injection current in order to achieve the population inversion. Significant amount of the electrical power applied to the device's terminals is responsible for the pronounced heat generation. If the thermal stability of a given laser diode is not sufficient, self-heating limits considerably its performance. Excess heat triggers the carrier escape from the active region. As a result, special design considerations and different laser mounting schemes need to be taken into account in order to achieve CW operation within a reasonable range of driving currents. Optical confinement of the guided mode and the total internal propagation loss are important parameters characterizing a resonant cavity. They cannot be omitted as the former defines the lasing threshold and the latter influences the external quantum efficiency. Thus the optimized structure of the optical waveguide providing the best overlap of the cavity mode with the active region as well as the lowest possible propagation loss is a crucial task for finding the optimum design for a laser device. The above-mentioned difficulties, often remaining unresolved in case of III-nitride laser technology, make the modern devices still far from the optimum.

Chapter Three

Device Physics and Numerical Model

3.1 Introduction

Over the last decade, optical fiber communication has become the choice for the worldwide communication network. Semiconductor based light sources and detectors are critically important to this emerging technology. Progress in optoelectronics has expanded not so much by device scaling as by new device physics. A semiconductor heterostructure can have a quantum confinement in one dimension, two dimensions, or three dimensions [50]. Laser operation in a quantum wells was first demonstrated in 1974. AlGaAs/GaAs was the first heterostructure ever made. The most commonly used method, in particular with optoelectronic device modeling, is based upon the conventional Luttinger-Kohn (LK) model. While a competing first principles approach was already developed in the 80's and 90's by Burt and Foreman (BF). BF theory are relevant to modeling optoelectronic devices to calculate the physical properties like band structures, optical momentum matrix elements etc. The ***k.p*** theory relies heavily on the use of momentum matrix elements. Using symmetry arguments we can show that many of these matrix elements are zero, and many of them are equal. This dramatically reduces the number of non-zero matrix elements that show up in the ***k.p*** equations. The reduced number of these matrix elements also allows us to treat them as fitting parameters, and to get their empirical values. In this chapter, we discuss the ***k.p*** theory in the formulation of Burt. Later we discuss the calculation of the momentum matrix elements (MME). This is a tough task, since the full eigenfunctions are never found, and only the eigenfunctions of the folded down Hamiltonian are available. The formula for calculating the MME is derived in the greatest detail, and the effects of using the Burt Hamiltonian or the symmetrized one are shown.

A recent one-dimensional theory predicted the remarkable existence of an inversion regime when the localization of the electron states can be reversed [51]. The calculation of intervalence subband optical transitions in quantum wells has been demonstrated by Chang and James (CJ) in 1989. It established that these transitions can have both TE and TM polarizations. Szmulowicz generalized the CJ equation to allow for position-dependent ***k.p*** parameters. The III-V nitride semiconductors, with wurtzite (WZ) crystal structure, have received a great deal of attention in recent years. The detailed band structure of these materials was studied after the discovery (in 1993) of blue light emission of WZ GaN on sapphire. In this Chapter, we analyze a WZ quantum well, using a 6-band ***k.p*** method. We derive the Hamiltonian and we calculate the band structure, using a formulation of the multiband envelope function theory. Besides crystal structure modification, strain and break of crystal symmetry of nitride semiconductor material system also brings certain modifications in their band structure. That's why, the band structure calculation of the nitride semiconductor device includes these effects. Details explanations are illustrated in the following sections.

3.2 Crystal and Energy Band Symmetry

3.2.1 Crystal Symmetry

The arranging order of the atoms in the process of crystal formation determines the symmetry properties of the crystal. There are two systems of symmetry existed in a semiconductor crystal. One is the translational symmetry for the periodicity of the atomic arrangement in solids. The other is the point symmetry. Point symmetry refers to the operations that keep the crystal unchanged, but with the exclusion of the translational symmetry [52]. They include rotations, inversions, and reflections. Translational symmetry constrains the operations of the point symmetry, because the periodical lattice must be the same after rotation operations. In Figure 3.1 the illustration of the symmetry has been shown.

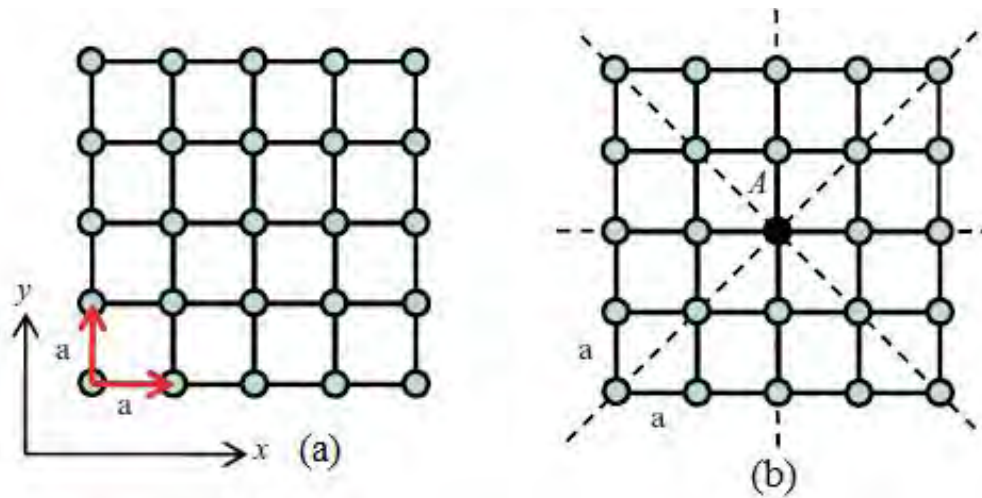


Figure 3.1 (a) An illustration of a 2D lattice which is the same after being translated by a in either x or y direction. (b) Diagram of point symmetry for the 2D lattice [52].

These symmetry properties have profound effects that determine the essential properties of a crystal. The semiconductor electronic properties are strongly dependent on crystal symmetry.

3.2.2 Energy Band Symmetry

Solving the quantum mechanical problem and finding the electronic states and energies in solids is very difficult and time-consuming because of the complex nature of the electric interaction in solids. However, symmetry has fundamental effects on band structures such as the $E-k$ relations in the k -space. Some important properties of the band structures can be acquired without complicated band calculations, and by studying the crystal symmetry alone. Translational symmetry restricts the electronic wave functions in a crystal to be Bloch waves. Bloch waves are plane waves modulated by periodic functions whose periodicity follows the crystal periodicity. This effect imposes a fundamental law on electronic states in solids. It is first important to understand that the band structure is constructed in the reciprocal space, which can be obtained by

a Fourier transformation of the real crystal lattice. If position vector of a lattice is \mathbf{r} with a periodicity of \mathbf{R} . The Fourier analysis of the crystal lattice is [53]:

$$f(\mathbf{r}) = \sum_{\mathbf{G}} f_{\mathbf{G}} \exp(i\mathbf{G} \cdot \mathbf{r}), \quad (3.1)$$

where the \mathbf{G} 's are vectors, as:

$$\exp(i\mathbf{G} \cdot \mathbf{r}) = \exp(i(G_x x + G_y y + G_z z)). \quad (3.2)$$

The set of all wave vectors \mathbf{G} that yield plane waves with the periodicity of a given Bravais lattice is known as its reciprocal lattice. From the periodicity properties it can infer [52, 53]:

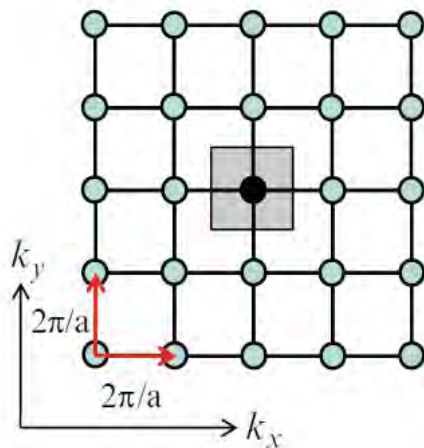
$$f(\mathbf{r}) = f(\mathbf{r} + \mathbf{R}), \quad (3.3)$$

and

$$\exp(i\mathbf{G} \cdot \mathbf{R}) = 1. \quad (3.4)$$

So, the reciprocal lattice is the set of vectors \mathbf{G} in Fourier space that satisfy the above requirement. The reciprocal space of a real lattice is also a lattice. The reciprocal lattice for the lattice shown in Figure 3.1a is also a 2D lattice with unit vector $2\pi/a$ shown in Figure 3.2a. The reciprocal lattice for an FCC lattice is a body-centered cubic (BCC) lattice. The traditional illustration of an energy band structure is to plot the energy levels in the first Brillouin zone. Wigner-Seitz cell of reciprocal lattice called the “First Brillouin Zone” or just “Brillouin Zone” which is geometrically a primitive cell of the reciprocal lattice, and conventionally defined as the space enclosed by planes perpendicular to and bisecting the lines connecting a reciprocal lattice point and its neighbors. The first Brillouin zone for the reciprocal lattice in Figure 3.2a is shown as the shaded area. The Brillouin zone for a FCC lattice is shown in Figure 3.2b. In this figure, the Γ point is the symbol for the center, the X point $(0, 2\pi/a, 0)$ labels the center of the square surfaces, the L point $2\pi/a (0.5, 0.5, 0.5)$ labels the center of the hexagonal surfaces. The line that connects the Γ point to the X point is labeled as Δ , and the direction from Γ to L is called Λ .

a



b

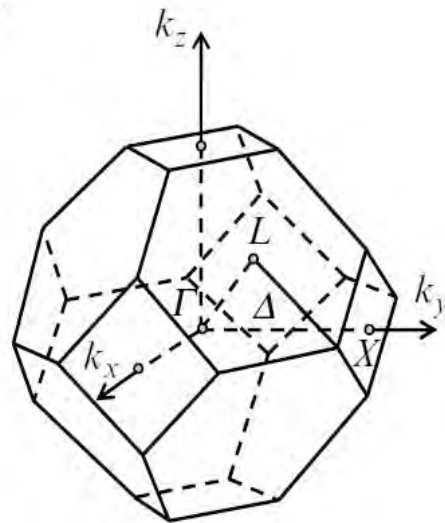


Figure 3.2 The first Brillouin zone or Brillouin zone for (a) a 2D lattice shown in figure 3.1a, and (b) a FCC lattice, with a lattice constant a [52].

The band structure, like the E - k diagram, describes the relation of the electron energy versus wave vector k from the origin of the Brillouin zone to the zone edge. k -space study of the band structure is importance because an electron has 6 dimensions; 3 real space dimensions, and 3 momentum space dimensions. An electron moves in solids in a form of Bloch waves, and k is its wave vector. In effective mass theory, $\hbar k$ is the momentum of the electron in solids, where \hbar is the Plank constant.

The center of any type of Brillouin zone is labeled as Γ . Without consideration of spin, the highest order of the valence band degeneracy normally equals the number of coordinates transformed by the symmetry operations. This is due to the fact that most semiconductor valence bands have p -characteristics. Cubic symmetry results in a threefold degeneracy at the Γ point without inclusion of spin because of the equivalency of the x , y , z directions in the Brillouin zone, and the energy diagrams along these directions are the same. However, their corresponding wave functions are linearly independent. In the valence bands of semiconductors other than cubic semiconductors, the x , y , and z directions are not all equivalent, and this results in the existence of the effective crystal field. In this case, the degeneracy order of the valence bands is less than three. Spin has very special rotational symmetry, and with spin-orbit interaction, the valence bands of cubic semiconductors include doubly degenerate heavy-hole and light-hole bands and one split-off band resulting from spin-orbit interaction, while hexagonal semiconductors have three split valence bands with each doubly (spin) degenerate at the Γ point resulting from both the spin-orbit interaction and nonzero crystal field.

Semiconductors having lower symmetry always have lower degeneracy orders, except sometimes they may have accidental degeneracy, like at the point of energy level crossing, which is not determined by symmetry. Besides the degeneracy at the same k point, there exists another kind of degeneracy, the star degeneracy. In this case, energies are the same at different k points that can be transformed into each other through some symmetry operations and become equivalent. But due to the cubic symmetry, the energies at these equivalent points must be the same, and these states are degenerate. When crystal symmetry changes, star degeneracy is also partially or fully lifted. The dependence of the band degeneracy on crystal symmetry clearly states the origin of the band splitting with strain. Shear strain reduces the crystal symmetry; its defined band degeneracy is lifted, and thus the originally degenerate energy levels are split.

3.3 Crystal Structure of Nitride Semiconductor

Many compound semiconductors, such as GaAs and InP, are grown in the zinc blende crystal system, while nitride devices are grown in the hexagonal (wurtzite) crystal system along with zinc blende crystal structure. Energy gaps (E_g) for the wurtzite nitride semiconductors and their alloys span the wide range from 0.7 to 6.2 eV or, in optical terms, from the near-infrared to the ultraviolet

(shown in Figure 3.3). Elaborate wurtzite nitride semiconductor crystal structure has been depicted in the Figure 3.4.

This leads to unique material properties, such as built-in electric fields due to spontaneous and piezoelectric polarization. The lattice-mismatched epitaxial growth causes a large number of dislocations in nitride devices, with dislocation densities that are more than five orders of magnitude higher than in other compound semiconductor devices. This phenomena can understood from the strain-stress relationship for the semiconductor material system.

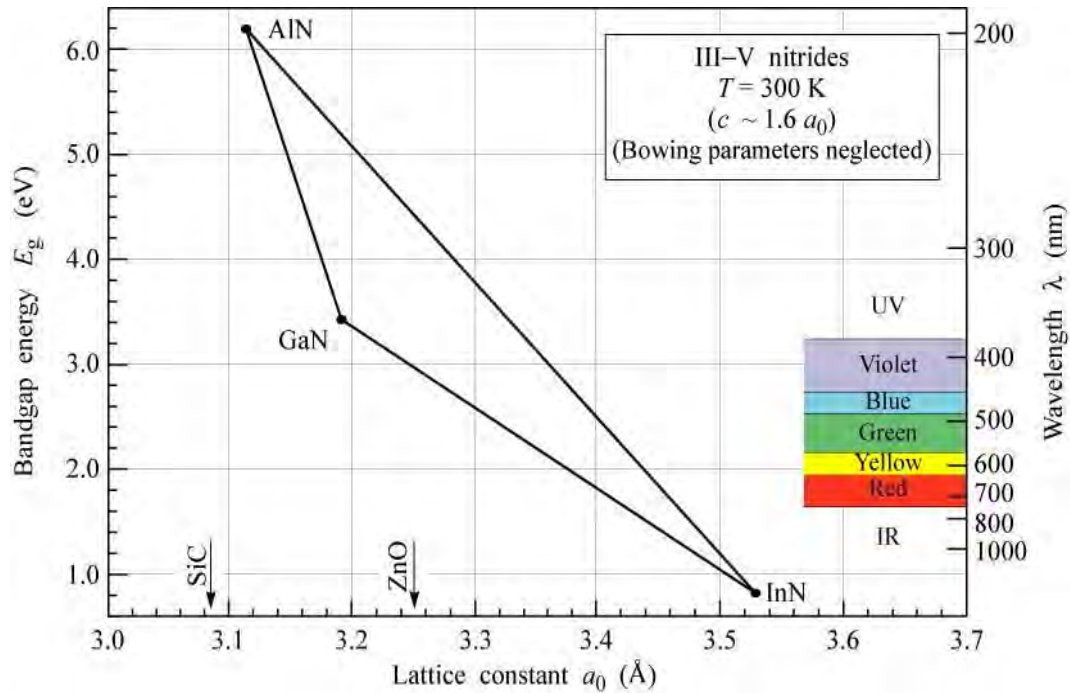


Figure 3.3: Energy band-gap range for nitride semiconductor binaries materials and their ternaries along with the wavelength range.

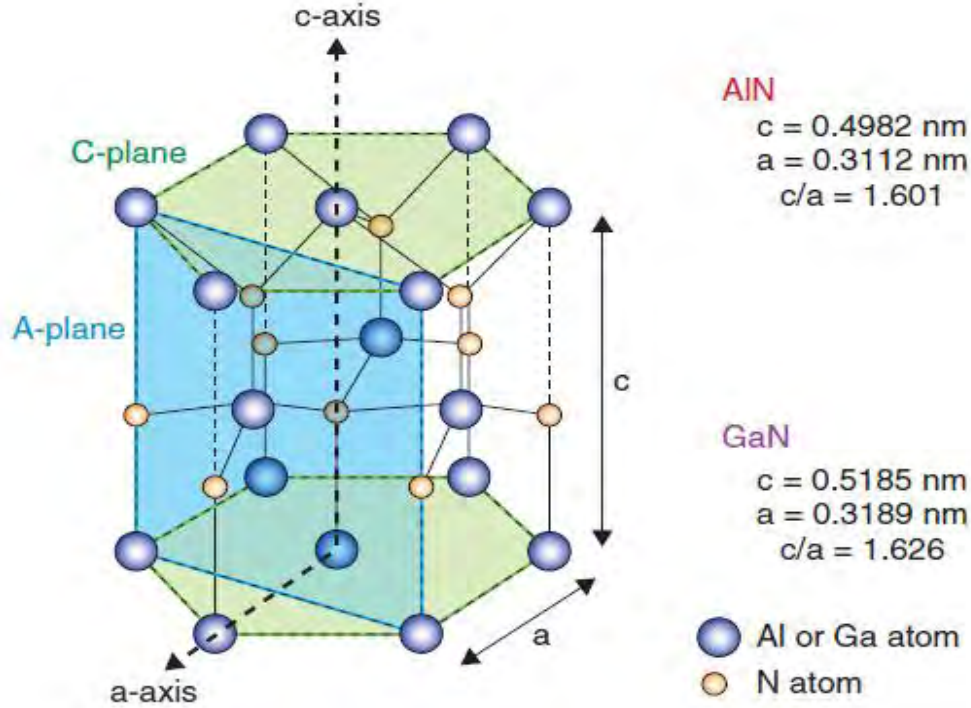


Figure 3.4: Wurtzite nitride semiconductor crystal structure showing relative atom positions and corresponding axes and planes.

3.4 Strain in Nitride Semiconductor

Strain in crystals is created by deformation of lattice points and is defined as relative lattice displacement. A mechanical force acting on a crystal lattice changes the relative positions of the lattice points. This can be characterized by a vector, \bar{u} which defines the relative displacement of an atom into a new position, $\hat{r} = \bar{r} + \bar{u}$ in some arbitrary Cartesian coordinate system. If the lattice points return to their original positions after the force is removed then the deformation is described as elastic. Knowing the relative displacements of each lattice site, the state of the crystal deformation can be described by strain components defining a second-rank tensor [54] as:

$$\epsilon_{ij} = \frac{1}{2} \left(\frac{\partial u_i}{\partial x_j} + \frac{\partial u_j}{\partial x_i} \right), \quad i, j = 1, 2, 3 \quad (3.5)$$

where u_1 , u_2 , and u_3 are the relative displacements of the crystal lattice points along the x_1 , x_2 and x_3 axes, respectively. The diagonal components represent extensions per unit length along the x_1 , x_2 and x_3 directions and are usually referred as 'stretches' showing in Figure 3.5, while the off-diagonal components, ϵ_{ij} are related to 'rotations'. The strain tensor is symmetrical and dimensionless ($\epsilon_{ij} = \epsilon_{ji}$) and can be written as [50]:

$$\bar{\epsilon} = \begin{pmatrix} \epsilon_{11} & \epsilon_{12} & \epsilon_{13} \\ \epsilon_{21} & \epsilon_{22} & \epsilon_{23} \\ \epsilon_{31} & \epsilon_{32} & \epsilon_{33} \end{pmatrix}. \quad (3.6)$$

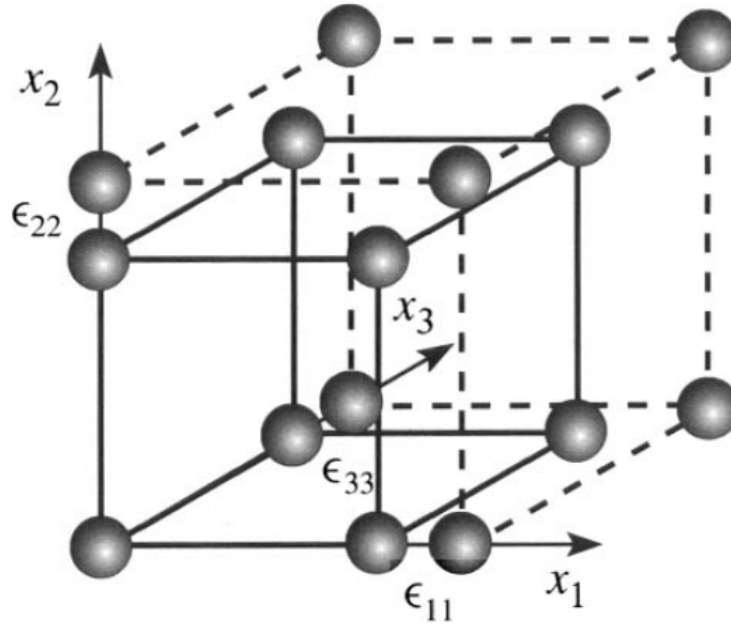


Figure 3.5: Schematic illustration of the diagonal strain components on the crystal structure. In the literature an intuitive notation is occasionally seen replacing the indices 1, 2 and 3 with x , y and z , e.g. $\epsilon_{11} \rightarrow \epsilon_{xx}$ [50].

If an external force is acted on a crystal or if part of a crystal is applying a force on a neighboring part, the crystal is said to be in the state of 'stress'. The stress is usually defined as the force per unit area of the crystal. Stress (shown in Figure 3.6) is commonly presented as a function of strain and Hooke's law [50]:

$$\sigma_{ij} = \sum_{k=1}^3 \sum_{l=1}^3 C_{ijkl} \epsilon_{kl}, \quad (3.7)$$

where C_{ijkl} are the 'elastic stiffness constants' and also form a fourth-rank tensor.

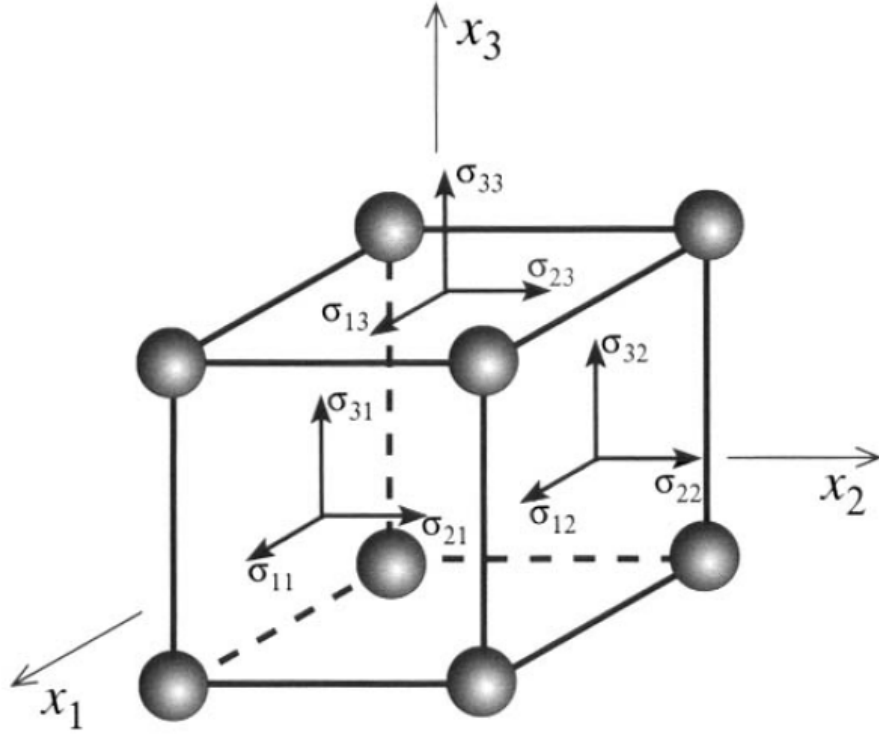


Figure 3.6: Directions of the stress components acting on a crystal lattice [50].

Hooke's law given by equation (3.7) in the matrix notation takes a simplified form [88, 102]:

$$\sigma_i = \sum_{k=1}^6 C_{ik} \epsilon_k \quad (3.8)$$

or equivalently [50]:

$$\begin{bmatrix} \sigma_1 \\ \sigma_2 \\ \sigma_3 \\ \sigma_4 \\ \sigma_5 \\ \sigma_6 \end{bmatrix} = \begin{bmatrix} C_{11} & C_{12} & C_{13} & C_{14} & C_{15} & C_{16} \\ C_{21} & C_{22} & C_{23} & C_{24} & C_{25} & C_{26} \\ C_{31} & C_{32} & C_{33} & C_{34} & C_{35} & C_{36} \\ C_{41} & C_{42} & C_{43} & C_{44} & C_{45} & C_{46} \\ C_{51} & C_{52} & C_{53} & C_{54} & C_{55} & C_{56} \\ C_{61} & C_{62} & C_{63} & C_{64} & C_{65} & C_{66} \end{bmatrix} \begin{bmatrix} \epsilon_1 \\ \epsilon_2 \\ \epsilon_3 \\ \epsilon_4 \\ \epsilon_5 \\ \epsilon_6 \end{bmatrix}, \quad (3.9)$$

where C_{ik} is now the elastic stiffness matrix. In order to define the elastic properties of the crystal 36 independent elastic stiffness constants are required. However, crystal lattices commonly exhibit certain symmetries which can be employed to reduce the number of constants necessary to describe their elastic behavior. The number of independent matrix components for the most used semiconductors are: 3 for the cubic (e.g. GaAs) and 5 for the hexagonal (e.g. wurtzite GaN) crystal geometries. Hence, the C matrices for the hexagonal semiconductors are given as [50]:

$$\begin{bmatrix} C_{11} & C_{12} & C_{13} & 0 & 0 & 0 \\ C_{12} & C_{11} & C_{13} & 0 & 0 & 0 \\ C_{13} & C_{13} & C_{33} & 0 & 0 & 0 \\ 0 & 0 & 0 & C_{44} & 0 & 0 \\ 0 & 0 & 0 & 0 & C_{44} & 0 \\ 0 & 0 & 0 & 0 & 0 & \frac{1}{2}(C_{11} - C_{12}) \end{bmatrix}. \quad (3.10)$$

If a thin epitaxial layer (i.e. GaN) (to form a quantum well) is pseudomorphically grown along the c axis on a much thicker substrate (i.e. $\text{Al}_x\text{Ga}_{1-x}\text{N}$) (usually assumed to be infinitely thick in comparison to the epitaxial layer) then the lattice constant (a_l) in the growth plane (perpendicular to the growth direction) of the layer will be forced to change to try and equal the lattice constant of the substrate (a_0). As a consequence, the crystal lattice is under biaxial stress along the growth interface and while no force is applied along the growth direction the crystal is able to relax freely along that direction. Therefore, the stress has only two diagonal components while last diagonal element and the shear components are zero. The biaxial stress results an in-plane strain. Growth which allows the lattice constant of the epitaxial layer to fully match the substrate is usually referred as pseudomorphic growth. Though no stress exists in the growth direction the lattice constant is still forced to change due to the 'Poisson effect'. If the compressive strain forces the in-plane lattice constant to reduce then the lattice constant in the growth direction will increase and vice versa for tensile strain. Hence, strain exists in the growth direction as well. The ratio that determines the increase or decrease of the lattice constant due to the in-plane stress is called Poisson's ratio (ν) and it connects the in-plane and the perpendicular strains. In case of hexagonal crystal structure, from the general stress-strain relationship the elements of the strain tensor in the well region can be easily calculated as [50, 55]:

$$\epsilon_{xx} = \epsilon_{yy} = \frac{a_0 - a_l}{a_l}, \quad (3.11)$$

$$\epsilon_{zz} = -\frac{2C_{13}}{C_{33}}\epsilon_{xx}, \quad (3.12)$$

and

$$\epsilon_{xy} = \epsilon_{yz} = \epsilon_{zx} = 0. \quad (3.13)$$

In quantum well systems, the in-plane strain is usually, $\epsilon = 2\%$ for an AlN layer grown on a GaN substrate. However, some materials and their alloys have very similar lattice constants such as the GaAs/AlGaAs system for which $\epsilon < 0.1\%$ allowing them to be considered as unstrained. The lattice constant of the epitaxial layer can be either larger or smaller than the lattice constant of the substrate defining a compressive ($\epsilon_{xx} < 0$) or a tensile ($\epsilon_{xx} > 0$) strain, respectively. Both kinds of strain has been depicted in the Figure 3.7. A compressive strain will therefore force the lattice constant in the plane to shrink conversely tensile strain will force it to expand. It is also reasonable to assume that the strain in the thin semiconductor layers is homogeneous and therefore constant throughout the layer.

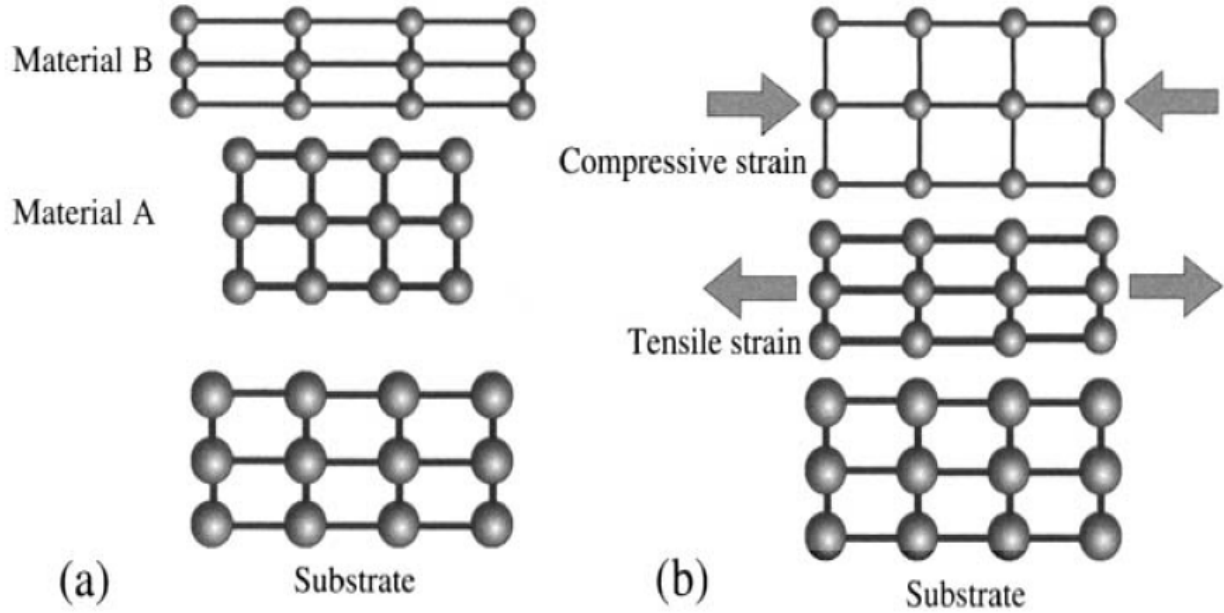


Figure 3.7: Schematic illustration of a substrate with two mismatched layers, (a) shows the free-standing unstrained layers with lattice constants smaller $a_l < a_0$ (material A) and larger $a_l > a_0$ (material B) than the lattice constant of the substrate and (b) shows the situation when either of the materials is grown on the substrate, i.e. material A is under tensile strain and material B is under compressive strain as their lattice constants are forced to be equal to the lattice constant of the substrate [50].

If the epitaxial layer width is larger than some critical thickness the layer relaxes in the plane restoring its original lattice constant. This is a violent process producing a large number of defects and imperfections in the growth surface. The formation of defects and the existence of a critical thickness can be understood in term of the elastic energy. The strained layer system possesses a certain additional elastic energy which is a function of the layer thickness (approximately a product of the elastic energy density, the area and the layer width). If for a specific layer width the strain energy exceeds the energy required for the generation of defects, then the system will tend to relax to a new state with lower strain energy forming imperfections in the growth plane. The width of the layer for which this relaxation process occurs is commonly referred to as the 'critical thickness'. Therefore, pseudomorphic growth is a necessary condition for the fabrication of good quality layers with a small number of intrinsic defects.

The strain in epitaxial layers changes the crystal lattice geometry by perturbing its size and symmetry. This results in a change of the electronic structure in particular a modification of the conduction and valence band edges and therefore a corresponding shift in the energy levels. If the strain is assumed to be small, which is the case in semiconductor quantum wells ($\sim 1\%$), first order perturbation theory can be used to calculate the band shift. The Hamiltonian under strain can be expressed as the sum of the unperturbed Hamiltonian (H_0) and the strain induced contribution (H_ϵ) [50]:

$$H = H_0 + H_\epsilon. \quad (3.14)$$

From perturbation theory it follows that the energy shift due to strain can be expressed in terms of the deformation potential components representing the matrix elements of the relative band shift due to strain as [50, 55]:

$$\delta E_c = \sum_{ij} D_{ij} \epsilon_{ij}. \quad (3.15)$$

Here, the D_{ij} forms a second-rank tensor though the matrix representation is commonly used. The number of non-zero D_{ij} components is dependent on the crystal symmetry and the type of band minimum. For the conduction band F point in cubic semiconductors all the off-diagonal deformation potential components vanish ($D_{ij} = 0$) leaving only three equal diagonal constants $D_{11} = D_{22} = D_{33} = a_c$ (the isotropic case) which are usually determined by fitting to experimental data.

Hexagonal crystals exhibit much less symmetry than cubic ones. Consequently, a certain anisotropic behavior can be expected and this is reflected in the different deformation potential constants. For example, GaN in the growth plane has identical deformation potential constants $D_{11} = D_{22} = a_{c\perp}$ whilst in the growth direction the constant $D_{33} = a_{c\parallel}$ is almost three times larger. This energy shift is also known as the hydrostatic energy shift which is zero in the barrier regions. The total conduction band shift in GaN then follows as [50]:

$$\delta E_c^{hex} = a_{c\perp}(\epsilon_1 + \epsilon_2) + a_{c\parallel} \epsilon_3. \quad (3.16)$$

The conduction band shift depends significantly on the material deformation potential constants and the lattice mismatch, and can be up to a few hundreds of meV shown in Figure 3.8. In some literature, it is assumed that $a_{c\parallel} = a_{c\perp}$ for simplicity and assumed a value of -4.08 eV from a recent fit to the available experimental data. It is interesting to see that although the wurtzite AlGaIn layer grown on GaN is highly strained in the growth plane, because of the anisotropy of the hexagonal crystals the overall shift is smaller.

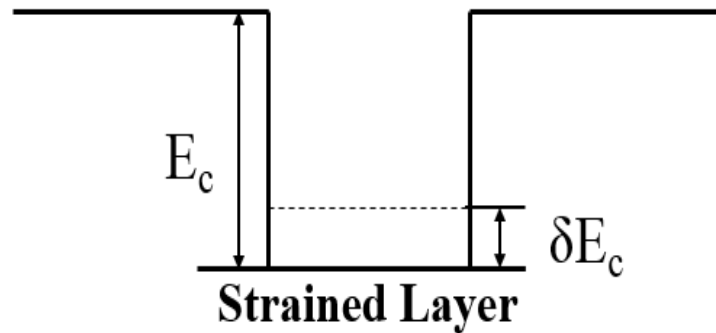


Figure 3.8: Illustration of the conduction band edge of a quantum well with a strain induced energy band shift while the original conduction band discontinuity is E_c [50].

For GaN quantum well layer sandwiched between $\text{Al}_x\text{Ga}_{1-x}\text{N}$ barrier layers, the interband deformation potential is negative, the band gap increases with an increasing compressive strain, as shown in Figure 3.9. The conduction-band edge is shifted upward for compressive strain.

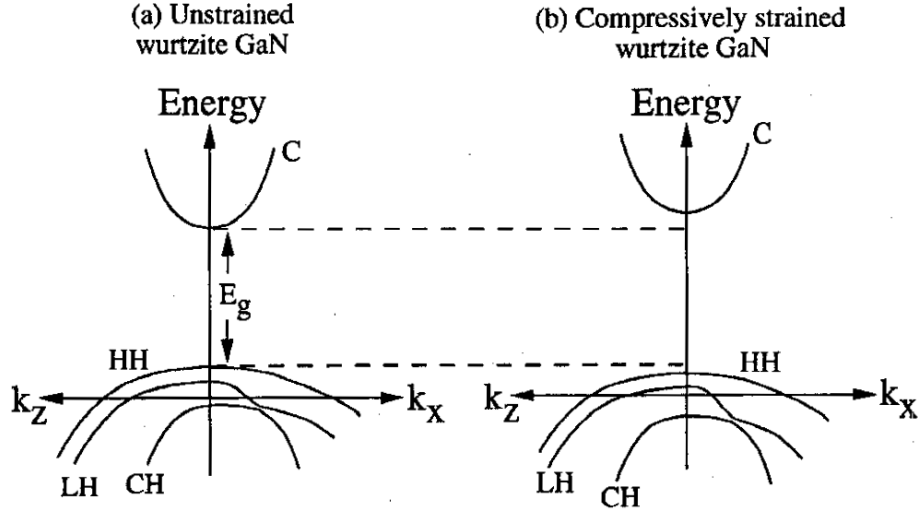


Figure 3.9: Schematic diagram showing the bulk band structures of (a) an unstrained GaN wurtzite semiconductor and (b) a compressively strained GaN layer [55].

3.5 Piezoelectric Effect

Certain types of crystal materials exhibit a behavior such that under stress, an extra electric charge gathers on their surfaces often named as sheet charge. The effect is called 'piezoelectricity' and is a consequence of a non-compensated electric polarization generated in the volume of the crystal. Piezoelectric behavior is exhibited in quartz, Rochelle Salt and Tourmaline, as well as in cubic and hexagonal semiconductors such as InGaAs and GaN. The piezoelectric (PZ) effect in strained semiconductor layers allows for the possibility of incorporating important PZ fields of the order of $\sim 100 \text{ kVcm}^{-1}$ which modify profoundly the optical and electrical properties in a hetero-structure. After the first works that established and characterized the PZ effect in strained heterostructures, many researchers intrigued by this new tool of hetero-structure design explored and evaluated the usefulness of the effect in a wide variety of optoelectronic devices. Specifically, large photo-induced optical non-linearities in (111) quantum wells (QWs) were predicted and thoroughly examined in a number of references [56]. GaN heterostructures with a wurtzite crystal structure pseudomorphically grown in the (0001) orientation have a large strain-induced piezoelectric field [57]. It was shown that the optical gain in QW lasers is largely reduced due to the piezoelectric field at relatively low carrier densities [58].

The piezoelectric effect arises from stress-induced charge polarization in a crystal that lacks a center of inversion. The changes in the crystal lattice geometry due to stress act to separate the charges and break the local electrostatic neutrality in the crystal, a schematic diagram illustrating this effect for wurtzite GaN is given in Figure 3.10. The uncompensated positive and negative charges induce a global polarization vector, the properties of which are defined by the material and the nature of the applied stress. The polarization is related to stress through the piezoelectric tensor [50]:

$$\mathbf{P} = [\mathbf{e}] \mathbf{e}_{\text{strain}}. \quad (3.17)$$

where \mathbf{P} is the polarization vector and \mathbf{e}_{strain} is the strain written as a six component vector. Thus the piezoelectric tensor is a 3x6 matrix. For zinc blende semiconductors, the piezoelectric tensor only has one non-vanishing tensor element, e_{14} , and the polarization induced by strain is then given by [50]:

$$\begin{pmatrix} P_x \\ P_y \\ P_z \end{pmatrix} = \begin{pmatrix} 0 & 0 & 0 & e_{14} & 0 & 0 \\ 0 & 0 & 0 & 0 & e_{14} & 0 \\ 0 & 0 & 0 & 0 & 0 & e_{14} \end{pmatrix} \begin{pmatrix} e_{xx} \\ e_{yy} \\ e_{zz} \\ e_{yz} \\ e_{zx} \\ e_{xy} \end{pmatrix}. \quad (3.18)$$

Because of the special form of the piezoelectric tensor, only the shear strain generates the piezoelectricity. Again, the applied electric field across the piezoelectric material can generate strain.

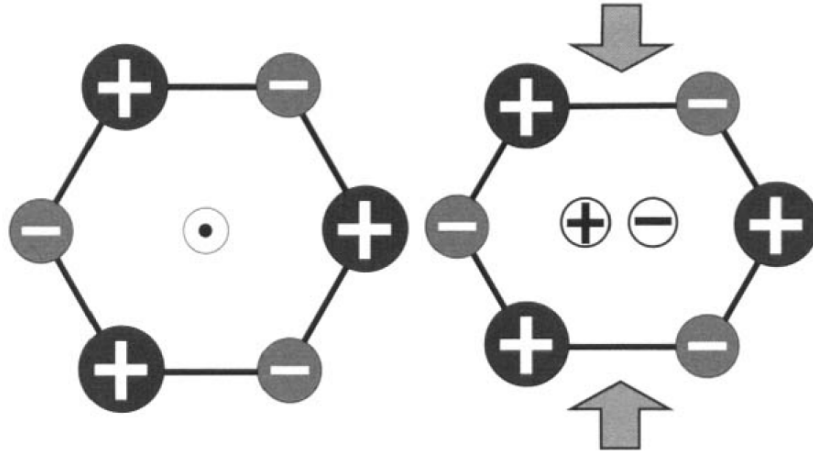


Figure 3.10: Illustration of the charge separation in GaN grown along the [0001] direction which causes the appearance of an uncompensated polarization. The left hand diagram shows the unstrained crystal lattice, and on the right the atomic positions when under strain [50].

For the other semiconductors lacking inversion symmetry, the piezoelectric tensor may have more than one non-vanishing component. In wurtzite semiconductors such as GaN, there are three nonvanishing components, e_{13} , e_{33} , and e_{15} . Piezoelectric effect may play an important role in semiconductor transport. In an AlGaIn/GaN heterostructure, the spontaneous polarization and the piezoelectric effect can induce large density of electrons even when there is no doping [59-60]. Piezoelectricity induced band bending can greatly change the potential profile, and thus alter the charge distribution and transport properties [61-62]. This is a common case in GaN-based HEMTs where the induced charge can significantly influence the electronic properties of devices. Furthermore, in quantum well structures the piezoelectric polarization can have a significant effect on the band profile through the electric fields induced. In some literature, the relationship of piezoelectric and stress with the total induced polarization is shown as [50]:

$$P_i = \sum_{k=1}^6 d_{ik} \sigma_k, \quad (3.19)$$

where d_{ik} is the piezoelectric modulus. The piezoelectric polarization is a vector which is described by three components, i.e. \mathbf{P}_1 and \mathbf{P}_2 in the growth plane and \mathbf{P}_3 along the growth direction. As for the case of the elastic constants, the symmetry in the crystals reduces the number of independent elements of the d matrix. For cubic and hexagonal crystal geometries the number of independent moduli relies on the crystal class e.g. one modulus for InGaAs and three moduli for wurtzite GaN. So it is stress induced symmetry breaking in a crystal which leads to a piezoelectric polarization, hence the underlying symmetry of the crystal is important.

3.6 Electronic Band Structures Formation with Strain Effects

To calculate the electronic band structure with strain effects, Tight-binding method and $\mathbf{k}\cdot\mathbf{p}$ method both provide a great framework to understand strain effects on band structures as well as band formation from atomic orbitals. First the tight-binding method is introduced visualizes the semiconductor bonding and strain effects. Although it is possible to calculate the semiconductor band structure accurately using tight-binding method, high-precision quantitative calculations based on tight-binding method require a large number of basis states, and the dimension of the Hamiltonian matrix needed to diagonalize to obtain the band structure is usually high. The consequences are long computer hours and difficulties to analyze the final results such as electronic wave function mixing. So for band calculation, the $\mathbf{k}\cdot\mathbf{p}$ method which usually has a much lower dimension Hamiltonian matrix to diagonalize and treats with high precision the strained bands at band edges where most carriers are located, is more familiar. Through $\mathbf{k}\cdot\mathbf{p}$ calculations, detailed band shifts and warping with strain are computed and presented finally.

The electronic wave function plays a more fundamental role than the band energy itself in the process of band formation, because after all, energy bands are created by atomic orbital overlap. Among energy bands, the conduction band states are mostly s-like in character (the microscopic 'Bloch' wave function has the symmetry of an atomic s orbital), while the valence band states are mostly p-like in character. There are three degenerate p-type atomic orbitals, the symmetry of which is denoted as x , y , and z , which stems from the direction along which the orbitals are aligned. It is therefore natural that all three of them will take part in valence band state wave functions. There are two valence bands degenerate at the center of the Brillouin zone (the Γ -point), and close by (a few tens to a few hundreds of meV below) there is a third band. The first two are called heavy-hole (HH) and light-hole (LH) bands, and they cease to be degenerate for finite values of the wave vector $\mathbf{k} = (k_x, k_y, k_z)$: the energy of the former descends at a slower rate as the wave vector moves away from the Γ -point, which corresponds to a larger effective mass, hence the name. The third band is called the spin-orbit split-off (SO) band or crystal-split-off hole (CH) band in case of hexagonal structure.

Hydrostatic strain reduces the atomic distance uniformly in the entire crystal, and thus the bandwidth is increased in all directions. Shear strain can increase the interatomic distance in some direction and reduce the interatomic distance in some other directions. In such cases, the bandwidth

shifts are different among different directions. Also, the electron effective mass variations are different for different directions. Under biaxial stress, the four bonds (in case of Si) all rotate toward or away from the x - y plane depending on whether it is compressive or tensile. For biaxial tension, all the four bonds are equivalent and rotate toward the x - y plane. With such a rotation, the weight of the p_x and p_y orbitals in the bonds increases and that of the p_z -orbital decreases. Along the [001] direction, this results in increased overlap integrals between in-plane orbitals and lowered HH bands and decreased overlap integrals between the p_z orbitals and ascended LH bands. Along the [100] and [010] direction, the LH band is lowered because it is composed mainly of the p_x and p_y orbitals, respectively, and the topmost bands are HH bands. Under such a band alteration, there is no pure HH or LH band. The top valence band under biaxial tension is LH-like out-of-plane and HH-like in-plane along z . Under compressive stress, the bonds that project along the [110] direction are shortened and pushed together and the bonds that project along the $[\bar{1}10]$ direction are elongated and pulled apart.

In the case of position-dependent potentials, states in quantum wells will be 'mixtures', with *all* the bulk bands contributing to their wave functions. The contribution of a particular bulk band to a quantized state generally depends on its energy spacing from that band: the smaller the energy, the larger the relative contribution will be. When two or more bands are degenerate, or almost degenerate, states in their vicinity are likely to have similar contributions from these bands. Generally, the Hamiltonians which describe states in such situations are matrices, or systems of coupled Schrodinger equations, which will deliver the possible energies and wave functions expressed as a set of envelope functions (which vary slowly over a crystalline unit cell), themselves representing the amplitudes of the corresponding basis states (usually the bulk bands). For this reason the method is known as the 'multiband envelope function', or 'multiband effective mass method' and, because the interaction of bulk bands is described via the $\mathbf{k}\cdot\mathbf{p}$ perturbation, it is also known as the $\mathbf{k}\cdot\mathbf{p}$ method. Using the $\mathbf{k}\cdot\mathbf{p}$ method one can obtain analytical expressions for the band dispersion and the effective masses. It allows the extrapolation of the band structure over the entire Brillouin zone from the energy gaps and optical matrix elements at the zone center. The $\mathbf{k}\cdot\mathbf{p}$ method can be derived from the one-electron Schrodinger equation given in (3.21), when the electronic state is non-degenerate and only weakly interacting with all other states.

$$H \psi_{n,k}(r) = E_{n,k} \psi_{n,k}(r), \quad (3.20)$$

with the Hamiltonian as

$$H = \frac{p^2}{2m_0} + V(r) + \frac{\hbar}{4m_0^2c^2} (\boldsymbol{\sigma} \times \nabla V) \cdot \mathbf{p}, \quad (3.21)$$

where

$$\mathbf{p} = -i\hbar \nabla. \quad (3.22)$$

Using the Bloch theorem the solutions of equation (3.21) are expressed, in the reduced zone scheme, as

$$\psi_{n,k}(r) = e^{i\mathbf{k}\cdot\mathbf{r}} u_{n,k}(r). \quad (3.23)$$

Since

$$(-i\hbar\nabla)e^{i\mathbf{k}\cdot\mathbf{r}} u_{n,k}(r) = \hbar\mathbf{k}e^{i\mathbf{k}\cdot\mathbf{r}} u_{n,k}(r) + e^{i\mathbf{k}\cdot\mathbf{r}} (-i\hbar\nabla)u_{n,k}(r), \quad (3.24)$$

and

$$(-i\hbar\nabla)^2 e^{i\mathbf{k}\cdot\mathbf{r}} u_{n,k}(r) = \hbar^2 k^2 e^{i\mathbf{k}\cdot\mathbf{r}} u_{n,k}(r) + 2\hbar\mathbf{k} \cdot e^{i\mathbf{k}\cdot\mathbf{r}} (-i\hbar\nabla)u_{n,k}(r) + e^{i\mathbf{k}\cdot\mathbf{r}} (-i\hbar\nabla)^2 u_{n,k}(r). \quad (3.25)$$

Substituting equation 3.23 into 3.21 we get the simplified $\mathbf{k}\cdot\mathbf{p}$ model for 1-band [32]:

$$\left(\frac{\hbar^2 k^2}{2m_0} + \frac{2\hbar\mathbf{k}\cdot\mathbf{p}}{2m_0} + \frac{p^2}{2m_0} + V(r) + \frac{\hbar}{4m_0^2 c^2} (\boldsymbol{\sigma} \times \nabla V) \cdot (\hbar\mathbf{k} + \mathbf{p}) \right) u_{n,k}(r) = E_{n,k} u_{n,k}(r). \quad (3.26)$$

While the $\mathbf{k}\cdot\mathbf{p}$ theory has been frequently used to model the valence band of semiconductors, one can apply it to model the impact of strain on the conduction band minimum. We only applied $\mathbf{k}\cdot\mathbf{p}$ method on valence band calculation. Here, the conduction bands has been characterized by a parabolic-band model, and the effective-mass Hamiltonian can be written as [55]

$$H^c(k_t, k_z) = \left(\frac{\hbar^2}{2} \right) \left(\frac{k_t^2}{m_e^t} + \frac{k_z^2}{m_e^z} \right) + E_c^0(z) + P_{c\epsilon}(z) + P_{pz}(z), \quad (3.27)$$

where, the wave vectors are $\mathbf{k}_t = -i\nabla_t$, $\mathbf{k}_z = -i\partial/\partial z$ and the magnitude of the in-plane wave vector in the k_x - k_y plane can be expressed as $k_t = \sqrt{k_x^2 + k_y^2}$. m_e^t and m_e^z are the effective masses perpendicular (t) and parallel (z) to the growth axis respectively. $E_c^0(z)$ in above equation is the QW potential profile of the unstrained conduction band edge. In well region, conduction band edge of well material is considered as the value of $E_c^0(z)$ and for barrier, barrier material band edge is taken as the reference. The hydrostatic energy shift in the conduction band, $P_{c\epsilon}(z)$ is zero in the barrier regions and is expressed as equation in 3.16 due to the strain in the well region. The numerical model takes into account the electric field resulting from both the spontaneous and piezoelectric polarization fields. The spontaneous polarization uses the linear interpolation described in ref. [122]. The piezoelectric polarization can be expressed as follows [63]

$$P_{pz} = 2d_{31} \left(C_{11} + C_{12} - \frac{2C_{13}^2}{C_{33}} \right) \epsilon_{xx}, \quad (3.28)$$

where d_{31} and C 's are piezoelectric coefficient and elastic stiffness coefficients respectively. The existence of both built-in polarization fields in wurtzite III-Nitride semiconductors leads to energy band bending. The electrostatic fields in each layer j th as a result of total polarization fields can be expressed as [50, 63]

$$E_j = \frac{\sum_k \frac{l_k P_k}{\epsilon_k} - P_j \sum_k \frac{l_k}{\epsilon_k}}{\epsilon_j \sum_k \frac{l_k}{\epsilon_k}}, \quad (3.29)$$

Where P is the total macroscopic polarization, ϵ is the static dielectric constant, and l is the thickness of each layers (k th, j th). The subscripts k and j correspond to the k th and l th layers. To ensure zero average electric field in the layers, note that the electric field expression in (12) needs to satisfy the periodic boundary conditions as follows [63]:

$$\sum_k l_k E_k = 0. \quad (3.30)$$

The induced internal electric field due to the piezoelectric polarization effect is depicted in Figure 3.11 and Figure 3.12.

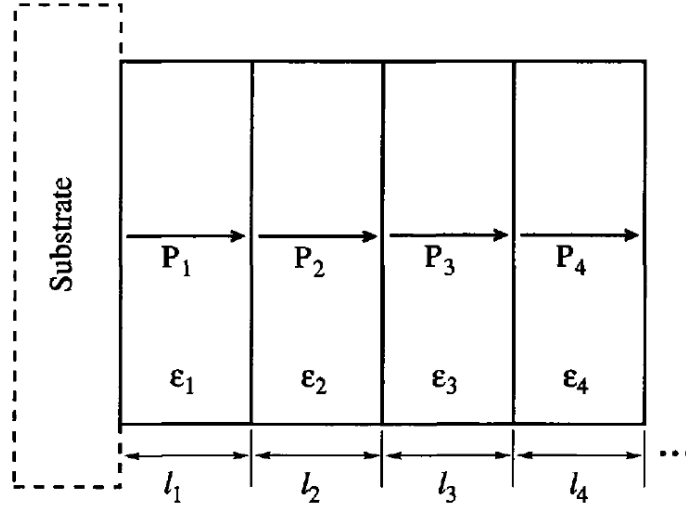


Figure 3.11: Schematic diagram of a multilayer structure based on piezoelectric material [50].

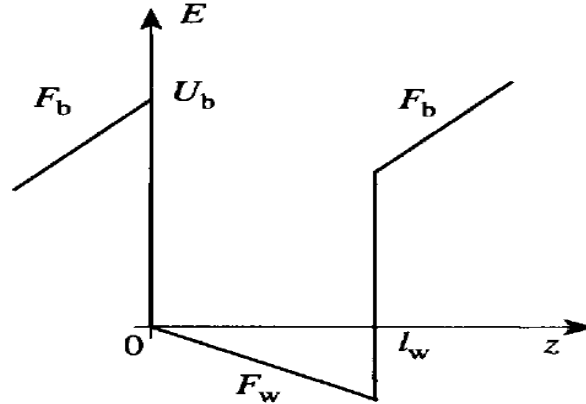


Figure 3.12: schematic diagram of typical induced internal electric fields in a quantum well and barrier region based on piezoelectric materials [50].

The wave function of the n th conduction subband can be written as [63]

$$\Psi_{n,k_t}^{c\eta}(z) = \frac{e^{ik_t \cdot r_t}}{\sqrt{A}} \phi_n(z) |\zeta, \eta\rangle, \quad (3.31)$$

where k_t is the transverse wave vector, r_t is the two dimensional position vector and A is the area of the quantum well in the x - y plane, $\phi_n(z)$ is the envelope function for the z -dependent part of

the n th conduction subband, and η is the electron spin (either upspin (\uparrow) or downspin (\downarrow)). The conduction-band-edge energy $E_n^c = E_n^c(k_t = 0)$ is determined by solving the effective-mass equation for electrons [63]

$$H^c(k_t = 0, k_z = -i \partial / \partial z) \phi_n(z) = E_n^c \phi_n(z), \quad (3.32)$$

with the envelope function normalized as

$$\int dz |\phi_n(z)|^2 = 1. \quad (3.33)$$

Here the following conduction band energy is used [63]

$$E_n^c(k_t) \approx E_n^c(k_t = 0) + \frac{\hbar^2 k_t^2}{2m_{e,\omega}^t} \quad (3.34)$$

to obtain the conduction-band structure, where $m_{e,\omega}^t$ is the electron effective mass in the well region parallel to the quantum well. The bulk valence-band structure can be determined by finding the eigenvalues of [63]

$$\det[H_{ij}^v(\mathbf{k}) - \delta_{ij} E^v(\mathbf{k})] = 0, \quad (3.35)$$

where \mathbf{k} is a real wave vector and the envelope functions are plane waves with the same wave vector \mathbf{k} . The Hamiltonian for the valence-band structure to calculate the hole wave function has been derived recently by the $\mathbf{k} \cdot \mathbf{p}$ method, and the matrix elements are defined consistently using chosen basis functions. The numerical model takes into account the valence band mixing, strain effect, spontaneous and piezoelectric polarization. Because of the large bandgap of the III–Nitride materials, the coupling between the conduction and valence bands is neglected. In this model, many-body Coulomb effects and carrier screening effect [64] are not taken into account. We found that the six-by-six Hamiltonian can be block-diagonalized using a unitary transformation [63]

$$H_{6 \times 6}^v(k) = \begin{bmatrix} H_{3 \times 3}^U(k) & 0 \\ 0 & H_{3 \times 3}^L(k) \end{bmatrix}, \quad (3.36)$$

where, $H_{3 \times 3}^U(k)$ and $H_{3 \times 3}^L(k)$ are 3×3 matrices defined as [62]

$$H^U = \begin{bmatrix} F & K_t & -iH_t \\ K_t & G & \Delta - iH_t \\ iH_t & \Delta + iH_t & \lambda \end{bmatrix}, \quad (3.37)$$

and

$$H^L = \begin{bmatrix} F & K_t & iH_t \\ K_t & G & \Delta + iH_t \\ -iH_t & \Delta - iH_t & \lambda \end{bmatrix}, \quad (3.38)$$

Note that the relations hold: $H^U = (H^L)^* = (H^L)^t$ and the reference energy, E_v^0 , which should appear in all the diagonal terms of the matrices, has been set to zero for a bulk semiconductor. The matrix

elements contain the general expressions for a strained wurtzite semiconductor are shown as follows [63]:

$$\begin{aligned}
F &= \Delta_1 + \Delta_2 + \lambda + \theta, \quad G = \Delta_1 - \Delta_2 + \lambda + \theta, \\
\lambda &= \lambda_k + \lambda_\epsilon, \\
\lambda_k &= \frac{\hbar^2}{2m_0} (A_1 k_z^2 + A_2 k_t^2), \quad \lambda_\epsilon = D_1 \epsilon_{zz} + D_2 (\epsilon_{xx} + \epsilon_{yy}), \\
\theta &= \theta_k + \theta_\epsilon, \\
\theta_k &= \frac{\hbar^2}{2m_0} (A_3 k_z^2 + A_4 k_t^2), \quad \theta_\epsilon = D_3 \epsilon_{zz} + D_4 (\epsilon_{xx} + \epsilon_{yy}), \\
K_t &= \frac{\hbar^2}{2m_0} A_5 k_t^2, \quad H_t = \frac{\hbar^2}{2m_0} A_6 k_t k_z.
\end{aligned} \tag{3.39}$$

Note that the bases for the Hamiltonian $H_{6 \times 6}^v$ in equation 3.32 are defined as [63]

$$\begin{aligned}
|1\rangle &= \alpha^* |Y_{11} \uparrow\rangle + \alpha |Y_{1-1} \downarrow\rangle \\
|2\rangle &= \beta |Y_{1-1} \uparrow\rangle + \beta^* |Y_{11} \downarrow\rangle \\
|3\rangle &= \beta^* |Y_{10} \uparrow\rangle + \beta |Y_{10} \downarrow\rangle \\
|4\rangle &= \alpha^* |Y_{11} \uparrow\rangle - \alpha |Y_{1-1} \downarrow\rangle \\
|5\rangle &= \beta |Y_{1-1} \uparrow\rangle - \beta^* |Y_{11} \downarrow\rangle \\
|6\rangle &= -\beta^* |Y_{10} \uparrow\rangle + \beta |Y_{10} \downarrow\rangle \\
Y_{11} &= \frac{-1}{\sqrt{2}} |X + iY\rangle, \quad Y_{10} = |Z\rangle, \quad Y_{1-1} = \frac{1}{\sqrt{2}} |X - iY\rangle,
\end{aligned} \tag{3.40}$$

where

$$\alpha = \frac{1}{\sqrt{2}} e^{i\left(\frac{3\pi}{4} + \frac{3\phi}{2}\right)}, \quad \beta = \frac{1}{\sqrt{2}} e^{i\left(\frac{\pi}{4} + \frac{\phi}{2}\right)}, \tag{3.41}$$

where $\phi = \tan^{-1}(k_x/k_y)$ is the azimuthal angle in the k_x - k_y , plane and covers a range between 0 and 2π . The wave functions Y_{lm} ($l = 1, m = -1, 0, 1$) in (3.36) are the spherical harmonics of the p state of hydrogen atom in Cartesian coordinates. The A_i s are the band-structure parameters, which play the same role as the Luttinger parameters, γ_1 , γ_2 , and γ_3 , of zincblende crystals. Δ_1 is the crystal-field split energy and is caused by the anisotropy of the wurtzite symmetry. It is the difference between the eigenvalues of the unperturbed Hamiltonian, H_0 , of the X -like (or Y -like) states and the Z -like states before the spin-orbit coupling effect is included, $\langle X|H_0|X\rangle = \langle Y|H_0|Y\rangle = E_v + \Delta_1$, and $\langle Z|H_0|Z\rangle = E_v$. E_v is the reference energy. Δ_2 and Δ_3 account for spin-orbit interactions. It should be pointed out that under the cubic approximation [65], the following relations hold among the parameters A_i s and Δ_i s [63]:

$$A_1 - A_2 = -A_3 = 2A_4, \quad A_3 + 4A_5 = \sqrt{2}A_6, \quad D_1 - D_2 = -D_3 = 2D_4, \quad \Delta_2 = \Delta_3. \tag{3.42}$$

Therefore, five band-structure parameters such as A_1 , A_2 , A_5 , Δ_1 , and Δ_2 , plus two deformation potentials D_1 and D_2 , are necessary for the calculation of the valence band structures. Sometimes, the spin-orbit split energy $\Delta_{so} = 3\Delta_2 = 3\Delta_3$ is used. The valence-band-edge energies for unstrained

layers can be obtained by finding the eigenvalues of the three-by-three Hamiltonians in 3.37 and 3.38, evaluated at the zone center ($\mathbf{k} = 0$) [55]

$$\begin{aligned} E_{HH} &= E_v^0 + \Delta_1 + \Delta_2, \\ E_{LH} &= E_v^0 + \frac{\Delta_1 - \Delta_2}{2} + \sqrt{\left(\frac{\Delta_1 - \Delta_2}{2}\right)^2 + 2\Delta_3^2}, \\ E_{CH} &= E_v^0 + \frac{\Delta_1 - \Delta_2}{2} - \sqrt{\left(\frac{\Delta_1 - \Delta_2}{2}\right)^2 + 2\Delta_3^2}. \end{aligned} \quad (3.43)$$

The conduction band edge is above the top valence band edge by a bandgap energy E_g . It can be seen from Figure 3.13 that the top valence band for GaN is E_{HH} , since Δ_1 is positive. Therefore the conduction band-edge is taken as [55]

$$E_c^0 = E_{HH} + E_g = E_v^0 + \Delta_1 + \Delta_2 + E_g. \quad (3.44)$$

For AlN, the topmost valence band is E_{LH} , since Δ_1 is negative. So for AlN, Therefore the conduction band-edge is [55]

$$E_c^0 = E_{LH} + E_g. \quad (3.45)$$

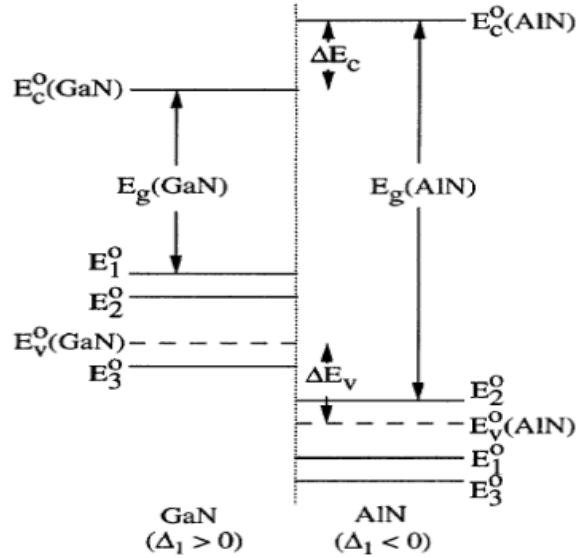


Figure 3.13: Elaborate illustration of electronic band energies (both conduction and valence band edge) for different sign of Δ_1 for GaN (left side) and AlN (right side) [55].

Generally, it is decided that a layer under either a compressive or tensile strain depending on the substrate materials, with the convention that the in-plane strain ϵ_{xx} is negative for compression and positive for tension. The conduction band edge energy with strain effects in a layer is [55]

$$\begin{aligned} E_{HH} &= E_v^0 + \Delta_1 + \Delta_2 + \theta_\epsilon + \lambda_\epsilon, \\ E_{LH} &= E_v^0 + \frac{\Delta_1 - \Delta_2 + \theta_\epsilon}{2} + \lambda_\epsilon + \sqrt{\left(\frac{\Delta_1 - \Delta_2 + \theta_\epsilon}{2}\right)^2 + 2\Delta_3^2}, \end{aligned}$$

$$E_{CH} = E_v^0 + \frac{\Delta_1 - \Delta_2 + \theta_\epsilon}{2} + \lambda_\epsilon - \sqrt{\left(\frac{\Delta_1 - \Delta_2 + \theta_\epsilon}{2}\right)^2 + 2\Delta_3^2}. \quad (3.46)$$

The conduction band-edge has a hydrostatic energy shift, $P_{c\epsilon}$, [55, 62]

$$E_c = E_c^0 + P_{c\epsilon} = E_c^0 + a_{cz}\epsilon_{zz} + a_{ct}(\epsilon_{xx} + \epsilon_{yy}), \quad (3.47)$$

where a_{cz} and a_{ct} are the deformation potentials in the conduction band. For example, if GaN is sandwiched between two thick $Al_xGa_{1-x}N$ layers, it is compressively strained because the lattice constant a of the GaN layer before deformation is larger than the lattice constant a_0 of $Al_xGa_{1-x}N$. Therefore ϵ_{xx} is negative, and the band-edge shifts will be positive for the conduction band and negative for the top valence bands. The bandgap with strain shift is determined by [55]

$$\begin{aligned} E_c - E_{HH} &= E_g + P_{c\epsilon} - (\lambda_\epsilon + \theta_\epsilon) \\ &= E_g + (a_{cz} - D_1 - D_3)\epsilon_{zz} + (a_{ct} - D_2 - D_4)(\epsilon_{xx} + \epsilon_{yy}). \end{aligned} \quad (3.48)$$

For a QW structure, the corresponding material parameters in the barrier and the well regions have to be used in the Hamiltonian. The band-edge discontinuities have to be added properly in the effective-mass equation. The hole wave function in a quantum well can be written as [55]

$$\Psi_m^U(z; k_t) = \frac{e^{ik_t r_t}}{\sqrt{A}} \left(g_m^{(1)}(z; k_t) |1\rangle + g_m^{(2)}(z; k_t) |2\rangle + g_m^{(3)}(z; k_t) |3\rangle \right), \quad (3.49)$$

and

$$\Psi_m^L(z; k_t) = \frac{e^{ik_t r_t}}{\sqrt{A}} \left(g_m^{(4)}(z; k_t) |4\rangle + g_m^{(5)}(z; k_t) |5\rangle + g_m^{(6)}(z; k_t) |6\rangle \right). \quad (3.50)$$

where $g_m^{(i)}$, $i = 1, 2, \dots, 6$ are the envelope functions of the m th valence subbands, which follow the normalization rules [55]

$$\sum_{i=1}^3 \int dz |g_m^{(i)}(z; k_t)|^2 = 1, \sum_{i=4}^6 \int dz |g_m^{(i)}(z; k_t)|^2 = 1. \quad (3.51)$$

The valence subband structure for the upper Hamiltonian $E_m^U(k_t)$ can be determined by solving

$$\sum_{j=1}^3 \left(H_{ij}^U \left(k_z = -i \frac{\partial}{\partial z} \right) + \delta_{ij} E_v^0(z) \right) g_m^{(j)}(z; k_t) = E_m^U(k_t) g_m^{(i)}(z; k_t) \quad (3.52)$$

for $i = 1, 2, 3$. Similarly, the band structure for the lower Hamiltonian, $E_m^L(k_t)$, can be obtained using $H_{ij}^L + \delta_{ij} E_v^0(z)$. $E_v^0(z)$ is the QW potential profile of the unstrained valence-band reference energy. The band-edge discontinuity for the valence band is $\Delta E_v^0 = Q_v \Delta E_g$ where ΔE_g is the bandgap difference between the unstrained well region material and barrier region material. The partition ratio, Q_v is taken from ref. [52] for the valence and conduction band. The strain-induced band edge shifts are taken into account in the diagonal terms of the Hamiltonian matrices. Since H^U and H^L differ only by a change of signs in front of all the terms with a single derivative with respect to z (i.e., $\partial/\partial z$ in H), it is easy to see that for a quantum well with a reflection symmetry

$E_v^0(z) = E_v^0(-z)$, the upper and lower Hamiltonians have the same valence-band structures $E_m^U(k_t) = E_m^L(k_t)$, and the wave functions are related by $g_m^{(1)}(z; k_t) = g_m^{(4)}(-z; k_t)$, $g_m^{(2)}(z; k_t) = g_m^{(5)}(-z; k_t)$, and $g_m^{(3)}(z; k_t) = g_m^{(6)}(-z; k_t)$.

3.7 Poisson's Equation

All of the techniques for solving the Schrodinger equation for any heterostructure need the known band-edge potential profile. All theoretical methods have concentrated solely on solving systems for a single charge carrier. In many devices such models would be inadequate as large numbers of charge carriers can be present in the conduction band seen in Figure 3.14. In order to decide whether typical carrier densities would give rise to a *significant* additional potential on top of the usual band-edge potential terms, it is necessary to solve the electrostatics characteristics of the system. The additional potential term $V_\rho(z)$ arising from the free carriers, or any other charge distribution ρ , can be expressed by using Poisson's equation [50]:

$$\nabla^2 V_\rho = -\frac{\rho}{\epsilon}, \quad (3.53)$$

where, ϵ is the permittivity of the material. The energy eigenvalues are calculated by considering the introduction of a further test electron into the system and incorporating the potential due to the carrier density already present into the standard Schrodinger equation, i.e. the potential term $V(z)$ in equations 3.21 or 3.26 becomes [50]:

$$V(z) \rightarrow V_{CB}(z) + V_\rho(z), \quad (3.54)$$

where V_{CB} represents the band edge potential at zero doping.

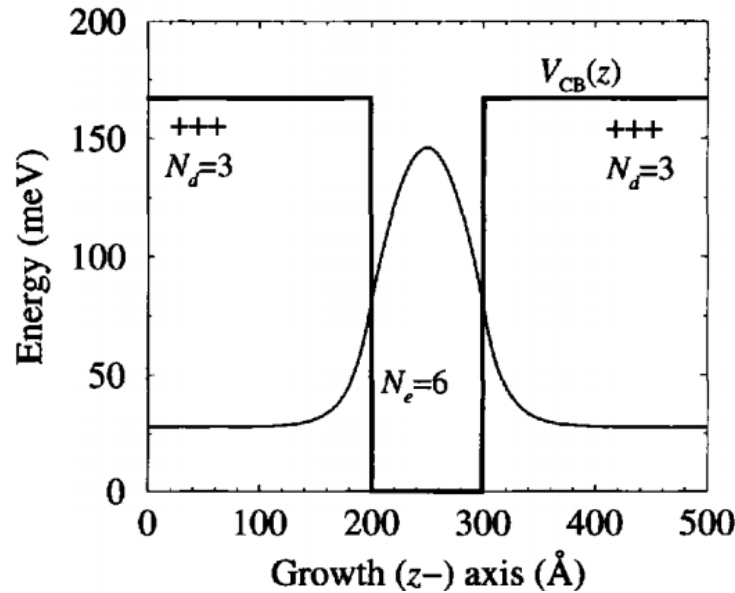


Figure 3.14: A typical doped single quantum well structure showing only conduction band profile [50].

The numerical method, described in detail earlier in this chapter, can be used without alteration to solve for this new potential, which will thus yield new energies and wave functions. The latter is an important point since the potential due to the charge distribution is itself dependent on the wave functions. Therefore, it is necessary to form a closed loop solving Schrodinger's equation, calculating the potential due to the resulting charge distribution, adding it to the original band edge potential, solving Schrodinger's equation again, and so on. The process is repeated until the energy eigenvalues converge; at this point the wave functions are simultaneously solutions to both Schrodinger's and Poisson's equations—the solutions are described as *self-consistent Schrodinger-Poisson solution*. The calculations of the Eigen energies and wave functions in our analysis are based on a self-consistent model by solving the Poisson equation expressed as follows [63]:

$$\frac{\partial}{\partial z} \left(\epsilon \frac{\partial V_{sc}}{\partial z} \right) = -\rho(z), \quad (3.55)$$

where V_{sc} incorporates the potential function including the effect of the spontaneous and piezoelectric polarizations and $\rho(z)$ is the charge distribution given by [63]

$$\rho(z) = |e| [p(z) - n(z)]. \quad (3.56)$$

The electron and hole concentrations are related to the wave functions of the n th conduction subband and the m th valence subband as well as their corresponding surface electron concentration (N_n) and surface hole concentration (P_m) as follows [63]:

$$n(z) = \sum_n |\phi_n(z)|^2 N_n \quad (3.57)$$

and

$$p(z) = \sum_m |g_m(z)|^2 P_m. \quad (3.58)$$

The surface electron concentration in the n th conduction band can be expressed as [63]

$$N_n = 2 \int_0^\infty \frac{2\pi k_t}{(2\pi)^2} \frac{1}{1 + e^{[E_{cn}(k_t) - E_c]/k_B T}} dk_t \quad (3.59)$$

and the surface hole concentration in the m th valence band is given by [63]

$$P_m = 2 \int_0^\infty \frac{2\pi k_t}{(2\pi)^2} \frac{1}{1 + e^{[E_v - E_{hm}(k_t)]/k_B T}} dk_t. \quad (3.60)$$

The inclusion of self-consistent electrostatic potential $V_{sc}(z)$ will modify both the total potential profiles for electrons [$U_e(z)$] and holes [$U_h(z)$] as follows [63]:

$$U_e(z) = U_0^e(z) - |e|V_{sc}(z) \quad (3.61)$$

and

$$U_h(z) = U_0^h(z) - |e|V_{sc}(z) \quad (3.62)$$

3.8 Characteristic Equations of the Optical Properties

The optical material gain coefficient of a quantum well can be calculated either from Fermi's golden rule, including a Lorentzian line-shape function or calculated from the spontaneous emission spectrum [66] using a fundamental relation between the spontaneous emission and gain spectra. Both methods are essentially the same. However, we adopt the latter because it gives more physical results below the band gap than the former model and the optical gain has a transparent energy at the quasi-Fermi level separation. The spontaneous emission rate per unit volume per energy interval at an optical energy $\hbar\omega$ is given by [55, 63]

$$r_{sp}^e(\hbar\omega) = \frac{n_r^2 \omega^2}{\pi^2 \hbar c^2} g_{sp}^e(\hbar\omega) \quad (3.63)$$

and

$$g_{sp}^e(\hbar\omega) = \frac{q^2 \pi}{n_r c \epsilon_0 m_0^2 \omega L_z} \sum_{\eta=\uparrow, \downarrow} \sum_{\sigma=U, L} \sum_{n, m} \int \frac{k_t dk_t}{2\pi} \int \frac{d\phi}{2\pi} |\hat{\mathbf{e}} \cdot \mathbf{M}_{nm}^{\eta\sigma}(k_t)|^2 \frac{f_n^c(k_t)(1-f_{\sigma m}^v(k_t))(\hbar\gamma/\pi)}{(E_{\sigma, nm}^{cv}(k_t) - \hbar\omega)^2 + (\hbar\gamma)^2}. \quad (3.64)$$

where q is the magnitude of the electron charge, m_0 is the electron rest mass in free space, c and ϵ_0 are the velocity of light and permittivity in free space, respectively, η is the electron spin, which can be either upspin (\uparrow) or downspin (\downarrow), $\hat{\mathbf{e}}$ is the polarization vector of the optical electric field, n_r and L_z are the refractive index and well width of the quantum well, and $\hbar\gamma$ is the half linewidth of the Lorentzian function ($\gamma = (0.1 \text{ ps})^{-1}$ is used in this work for simplicity). $M_{nm}^{\eta\sigma}(k_t) = \langle \Psi_{m, k_t}^{v\sigma} | \mathbf{p} | \Psi_{n, k_t}^{c\eta} \rangle$ is the momentum matrix element for transitions between the conduction-band state $\Psi_{n, k_t}^{c\eta}(z)$ and the valence-band state $\Psi_{m, k_t}^{v\sigma}(z)$, and \mathbf{p} is the momentum operator. For convenience, $g_{sp}^e(\hbar\omega)$ is defined to have the same dimension (1/cm) as the material gain coefficient. The expression [63]

$$E_{\sigma, nm}^{cv}(k_t) = E_n^c(k_t) - E_{\sigma, m}^v(k_t) \quad (3.65)$$

is the interband energy of the conduction band and the valence band. The Fermi-Dirac distributions for the electrons in the conduction and valence bands are [63]

$$f_n^c(k_t) = \frac{1}{1 + \exp\left(\frac{E_n^c(k_t) - F_c}{k_B T}\right)} \quad (3.66)$$

and

$$f_{\sigma m}^v(k_t) = \frac{1}{1 + \exp\left(\frac{E_{\sigma, m}^v(k_t) - F_v}{k_B T}\right)}, \quad (3.67)$$

where F_c and F_v are the quasi-Fermi levels for electrons and holes. The material gain can be determined from the spontaneous emission rate using [55, 63]

$$g(\hbar\omega) = g_{sp}^e(\hbar\omega) \left[1 - \exp\left(\frac{\hbar\omega - \Delta F}{k_B T}\right) \right], \quad (3.68)$$

where for TE polarization e represents x or y axis, which is perpendicular to the c axis and for TM polarization e represents z , which is parallel to the c axis. The modal gain $g_M = \Gamma_g$ is obtained by

multiplying the material gain by the optical confinement factor Γ . The separation of the quasi-Fermi levels, ΔF , depends on the injected carrier densities

$$\Delta F = F_c - F_v. \quad (3.69)$$

Using the expressions for the basis $|\mu_i^\sigma\rangle$ in (3.36), we obtain [55, 63]

$$|\hat{x} \cdot M_{nm}^{\eta U}(k_t)|^2 = \frac{|\langle S|p_x|X\rangle|^2}{4} \left\{ \left\langle \phi_n \left| g_m^{(1)} \right. \right\rangle^2 + \left\langle \phi_n \left| g_m^{(2)} \right. \right\rangle^2 + 2 \cos(2\phi) \left\langle \phi_n \left| g_m^{(1)} \right. \right\rangle \left\langle \phi_n \left| g_m^{(2)} \right. \right\rangle \right\}. \quad (3.70)$$

For η represents both upspin (\uparrow) and downspin (\downarrow) for electron, where we have used the following momentum matrix elements from the basis functions [55, 63]:

For TE- polarization (\hat{e} represents \hat{x} vector)

$$\begin{aligned} \langle S \uparrow | p_x | 1 \rangle &= -\frac{\alpha^*}{\sqrt{2}} \langle S | p_x | X \rangle \\ \langle S \uparrow | p_x | 2 \rangle &= \frac{\beta}{\sqrt{2}} \langle S | p_x | X \rangle \\ \langle S \uparrow | p_x | 3 \rangle &= 0 \\ \langle S \uparrow | p_x | 4 \rangle &= -\frac{\alpha^*}{\sqrt{2}} \langle S | p_x | X \rangle \\ \langle S \uparrow | p_x | 5 \rangle &= \frac{\beta}{\sqrt{2}} \langle S | p_x | X \rangle \\ \langle S \uparrow | p_x | 6 \rangle &= 0. \end{aligned} \quad (3.71)$$

For TM- polarization (\hat{e} represents \hat{z} vector)

$$\begin{aligned} \langle S \uparrow | p_x | 1 \rangle &= 0 \\ \langle S \uparrow | p_x | 2 \rangle &= 0 \\ \langle S \uparrow | p_x | 3 \rangle &= \beta^* \langle S | p_z | Z \rangle \\ \langle S \uparrow | p_x | 4 \rangle &= 0 \\ \langle S \uparrow | p_x | 5 \rangle &= 0 \\ \langle S \uparrow | p_x | 6 \rangle &= -\beta^* \langle S | p_z | Z \rangle. \end{aligned} \quad (3.72)$$

For considering upspin (\uparrow). Similar expressions can be derived for the downspin (\downarrow) in the conduction band. Since the only ϕ -dependent term in the integrand of (3.44) appears in the matrix elements, the integration of the $\cos(2\phi)$ term over ϕ vanishes. Then two scalar polarization dependent matrix elements has been obtained, which result from the ϕ integration of the momentum matrix elements [55, 63]:

For TE- polarization (\hat{e} represents \hat{x} or $\hat{y} \perp c$ axis):

$$\begin{aligned} |(M_x)_{nm}^\sigma(k_t)|^2 &= \frac{|\langle S|p_x|X\rangle|^2}{4} \left\{ \left\langle \phi_n \left| g_m^{(1)} \right. \right\rangle^2 + \left\langle \phi_n \left| g_m^{(2)} \right. \right\rangle^2 \right\} \text{ for } \sigma = U \\ &= \frac{|\langle S|p_x|X\rangle|^2}{4} \left\{ \left\langle \phi_n \left| g_m^{(4)} \right. \right\rangle^2 + \left\langle \phi_n \left| g_m^{(5)} \right. \right\rangle^2 \right\} \text{ for } \sigma = L \end{aligned} \quad (3.73)$$

For TM- polarization (\hat{e} represents $\hat{z} \parallel c$ axis):

$$\begin{aligned} |(M_z)_{nm}^\sigma(k_t)|^2 &= \frac{|S|p_x|Z|^2}{2} \left\langle \phi_n \left| g_m^{(3)} \right. \right\rangle^2 \text{ for } \sigma = U \\ &= \frac{|S|p_x|Z|^2}{2} \left\langle \phi_n \left| g_m^{(6)} \right. \right\rangle^2 \text{ for } \sigma = L \end{aligned} \quad (3.74)$$

Here, two equivalent energy parameters, E_{pz} and E_{px} , in terms of the band-edge momentum matrix elements has been defined as [63]

$$\frac{m_0 E_{pz}}{2} = \langle S|p_z|Z \rangle^2$$

and

$$\frac{m_0 E_{px}}{2} = \langle S|p_x|X \rangle^2. \quad (3.75)$$

for the interband transition in a similar way to that of the zinc-blende crystals [138], for which only one parameter is required. These energy parameters can be expressed in terms of the band-structure parameters by generalizing Kane's model to those for the wurtzite crystals, taking into account the hexagonal symmetry. We obtain [63]

$$E_{pz} = \left(\frac{m_0}{m_e^z} - 1 \right) \frac{(E_g + \Delta_1 + \Delta_2)(E_g + 2\Delta_2) - 2\Delta_3^2}{(E_g + 2\Delta_2)}$$

and

$$E_{px} = \left(\frac{m_0}{m_e^t} - 1 \right) \frac{E_g[(E_g + \Delta_1 + \Delta_2)(E_g + 2\Delta_2) - 2\Delta_3^2]}{(E_g + \Delta_1 + \Delta_2)(E_g + \Delta_2) - \Delta_3^2}. \quad (3.76)$$

The numerical values for the interband matrix elements can be calculated using the parameters from [17, 23, 38]. It should be pointed out that no experimental data for the magnitudes of the interband optical matrix elements are available due to the lack of a good calibration scheme; the above analytical model does provide a reasonable estimation for the interband matrix elements. The final expression for $g_{sp}^e(\hbar\omega)$ in the spontaneous emission rate is [63]

$$g_{sp}^e(\hbar\omega) = \frac{2q^2\pi}{n_r c \epsilon_0 m_0^2 \omega L_z} \sum_{\sigma=U,L} \sum_{n,m} \int \frac{k_t dk_t}{2\pi} |(M_e)_{nm}^\sigma(k_t)|^2 \frac{f_n^c(k_t)(1-f_{sm}^v(k_t))(\gamma/\pi)}{(E_{\sigma,nm}^{cv}(k_t) - \hbar\omega)^2 + \gamma^2}. \quad (3.77)$$

The total spontaneous emission rate per energy interval per unit volume, $r_{sp}(\hbar\omega)$ ($s^{-1}cm^{-3}eV^{-1}$), is given by [63]

$$r_{sp}(\hbar\omega) = \frac{n_e^2 \omega^2}{\pi^2 \hbar c^2} \frac{(2g_{sp}^x + g_{sp}^z)}{3}, \quad (3.78)$$

which uses the fact that the momentum-matrix element of the total spontaneous emission is the angular average of two TE-polarization components and one TM-polarization component [63]

$$|M_{sp}|^2 = \frac{1}{3}(2|M_x|^2 + |M_z|^2). \quad (3.79)$$

For a given injection level, the electron and hole concentrations are related by the charge neutrality condition

$$n + N_A = p + N_D, \quad (3.80)$$

where N_A and N_D are the ionized acceptor and donor concentrations, respectively, in the active region and are assumed to be zero for an undoped active layer. The electron concentration n and the hole concentration p are related to the quasi-Fermi levels, F_c , and F_v , in (3.46) and (3.47), by [63]

$$\begin{aligned} n &= \frac{2}{L_w} \sum_n \int \frac{k_t dk_t}{2\pi} f_n^c(k_t) \\ &= \frac{k_B T m_e^*}{\pi \hbar^2 L_w} \sum_n \ln[1 + e^{[F_c - E_n^c(0)]/k_B T}] \end{aligned} \quad (3.81)$$

and

$$p = \frac{1}{L_w} \sum_{\sigma=U,L} \sum_n \int \frac{k_t dk_t}{2\pi} (1 - f_{\sigma n}^v(k_t)). \quad (3.82)$$

The total spontaneous emission rate per unit volume ($s^{-1}cm^{-3}$) is obtained by integrating equation (3.58) over entire frequency range as follows [58]

$$R_{sp} = \int_0^\infty r_{sp}(\hbar\omega) d(\hbar\omega). \quad (3.83)$$

Thus, the radiative recombination current density (A/cm^2) is defined as [63]

$$J_{rad} = qdR_{sp}. \quad (3.84)$$

where, d is the active region length. In the calculations of the spontaneous emission spectra and optical gain for polar semiconductors, it is important to include all possible transitions between electron and hole confined states in the QW. As the polarization field-induced band bending in the III-Nitride QW leads to the breaking of the orthogonality condition between states with different quantum numbers, like $E_1^c - E_2^{HH}$, $E_2^c - E_1^{HH}$, and so on; transitions between such states – which are traditionally ‘forbidden’ [3] in nonpolar semiconductors – may have an appreciable transition probabilities as indicated by the nonzero values of their matrix elements, and therefore have to be included in the calculation [67].

3.9 Optimization using Genetic Algorithm

For optimization, several optimization algorithms are usually used by mathematicians, scientists and engineers. Among them, local search algorithms are prone to converge to a deceptive solution and are highly dependent on the starting point. Often the quality of the final solution is very

dependent upon the position of this starting point in the search space. The choice of a starting point plays a significant role in finding a good solution to the problem with a large number of local optima. In contrast, global techniques overcome these limitations, due to their ability to search into many valleys within the solution space. Moreover, Conventional search techniques are often incapable of optimizing non-linear multimodal functions. In such cases, a random search method might be required. However, undirected search techniques are extremely inefficient for large domains. On the other hand, a directed random search technique can efficiently and effectively find the global optimal solution in complex multi-dimensional search spaces [69].

Modern heuristic optimization techniques have aroused great interest among the scientific community in a wide variety of fields, because of their ability to solve multimodal and multidimensional discontinuous problems efficiently in a near optimal manner. Basically, these techniques try to mimic natural, biological or even cultural evolution, depending on the nature of the process. The most representative algorithms include simulated annealing (SA) [68], genetic algorithms (GA) [69-70], memetic algorithms and the relatively new particle swarm optimization (PSO) [71], ant colony optimization (ACO) [72], and cultural algorithms. In this work, genetic based optimization algorithm has been adopted for obtaining the optimal device performances which is adopted into many other works [73-74]. A GA is modelled on natural evolution in that the operators it employs are inspired by the natural evolution process. These operators, known as genetic operators, manipulate individuals in a population over several generations to improve their fitness gradually. The genetic algorithm as a multi-point optimization technique for multi-dimensional spaces. Since the genetic algorithm execution technique is not dependent on the error surface, it can be used to solve multi-dimensional, non-differential, non-continuous, and non-parametrical problems [69].

GA do not use much knowledge about the problem to be optimized and do not deal directly with the parameters of the problem. It works with codes which represent the parameters. It uses "mapping" to code each continuous variable into an internal binary string of fixed length. Such a mapping transforms the entire range of a continuous variable into a limited set of binary coded numbers. The bigger the binary string, the larger the search space. Obviously, to perform the mapping we need to set the minimum and maximum boundaries on the variable. There is no absolute assurance that a genetic algorithm will find a global optimum. It happens very often when the populations have a lot of subjects. Like other artificial intelligence techniques, the genetic algorithm cannot assure constant optimization response times. But among the all evolutionary algorithms, GA has some distinct features. The strength of GAs is in the parallel nature of their search. A GA implements a powerful form of hill climbing that preserves multiple solutions, eradicates unpromising solutions, and provides reasonable solutions. Through genetic operators, even weak solutions may continue to be part of the makeup of future candidate solutions. The genetic operators used are central to the success of the search. All GAs require some form of recombination, as this allows the creation of new solutions that have, by virtue of their parent's success, a higher probability of exhibiting a good performance. In practice, crossover is the

principal genetic operator, whereas mutation is used much less frequently. Crossover attempts to preserve the beneficial aspects of candidate solutions and to eliminate undesirable components, while the random nature of mutation is probably more likely to degrade a strong candidate solution than to improve it. Another source of the algorithm's power is the implicit parallelism inherent in the evolutionary metaphor. By restricting the reproduction of weak candidates, GAs eliminate not only that solution but also all of its descendants. This tends to make the algorithm likely to converge towards high quality solutions within a few generations [69]. Among the other popular optimization algorithms, PSO optimizes an objective function by undertaking a population-based search. The population consists of potential solutions, named particles, which are a metaphor of birds in flocks. These particles are randomly initialized and freely fly across the multidimensional search space. During flight, each particle updates its own velocity and position based on the best experience of its own and the entire population. The updating policy drives the particle swarm to move toward the region with the higher objective function value, and eventually all particles will gather around the point with the highest objective value. On the other hand, SA consists of a sequence of iterations. Each iteration consists of randomly changing the current solution to create a new solution in the neighborhood of the current solution. The neighborhood is defined by the choice of the generation mechanism. Once a new solution is created the corresponding change in the cost function is computed to decide whether the newly produced solution can be accepted as the current solution. If the change in the cost function is negative the newly produced solution is directly taken as the current solution. Whether this actually makes the algorithm better or worse, is not straightforward, but depends on the problem and the representation. Comparison between the optimization processes are shown in the following table 3.1.

Table 3.1: Comparison between the heuristic optimization techniques

Genetic Algorithm	Simulated Annealing	Particle Swarm Optimization
Faster computational effort than others.	Quick start with respect to GA	Performance depends on suitable selection of parameter
Higher accuracy to obtain better result.	Less amount of adjust parameters	No mixing of information
Fewer generations are needed to reach to optimum result.	Less accuracy to find out better result	Need more generations
Many adjust parameter with respect to others.	Cannot improve itself during running of generations	No elimination of population
Depend on genetic parameter	Only mutation takes place	Lower adjust parameter

Exchange information to get better solution		No genetic parameter
---	--	----------------------

3.9.1 GA's Parameters

Genetic Algorithms (GAs) are adaptive heuristic search algorithm based on the evolutionary ideas of natural selection and genetics. As such they represent an intelligent exploitation of a random search used to solve optimization problems. Although randomized, GAs are by no means random, instead they exploit historical information to direct the search into the region of better performance within the search space. The basic techniques of the GAs are designed to simulate processes in natural systems necessary for evolution, specially those follow the principles first laid down by Charles Darwin of "survival of the fittest". Since in nature, competition among individuals for scanty resources results in the fittest individuals dominating over the weaker ones. GAs simulate the survival of the fittest among individuals over consecutive generation for solving a problem. Each generation consists of a population of character strings that are analogous to the chromosome that we see in our DNA. Each individual represents a point in a search space and a possible solution. The individuals in the population are then made to go through a process of evolution.

As said earlier, GAs are initialized with a population of guesses within the search space rather than starting form a single point or guess. These choices are random and will be spread throughout the search space. Then, GA uses three operators, selection, crossover and mutation to direct the population over a series of time steps or generations towards convergence at the global optimum. Typically, the initial guesses are binary encodings of the true variables. “**Selection**” attempts to apply pressure upon the population in a manner similar to that of natural selection found in biological systems. Poorer performing individuals are discarded and better performing or fitter individuals have a greater than average chance of promoting the information they contain within the next generation [69].

“**Crossover**” allows solutions to exchange information in a way similar to that used by a natural organism undergoing reproduction. One method termed as single point crossover, is to choose pairs of individuals promoted by the selection operator, randomly choose a single point within the binary string and swap all the information between the two individuals. “**Mutation**” is used to randomly change the value of single bits within individual strings. Mutation is typically used very sparingly. After selection, crossover and mutation have been applied to the initial population, a new population will have been formed and the generational counter is increased by one. This process of selection, crossover and mutation is continued until a fixed number of generation s have elapsed or some form of convergence criterion has been met [69].

Fitness-proportional selection does not guarantee the selection of any particular individual including the fittest. Unless the fittest individual is occasionally not be selected as much fitter than

any other. Thus with fitness-proportional selection, the best solution to the problem that discovered so far, can be regularly thrown away. Though, it seems counterproductive, this can be advantageous for some problems because it slows the algorithm allowing it to explore more of the search space before convergence. The tradeoff between the exploration of the search space and the exploitation of discoveries made within the space is a recurrent theme in GA theory. The more exploitation that is made the faster the progress of the algorithm, but the greater the possibility of the algorithm failing to finally locate the true global optimum. For many applications the search speed can be greatly improved by not losing the best or elite member between generations. Ensuring the propagation of the elite member is termed elitism and requires that not only is the elite member selected, but a copy of it does not become disrupted by crossover or mutation [69]. The whole flowchart of the genetic algorithm has been depicted in the following Figure 3.15.

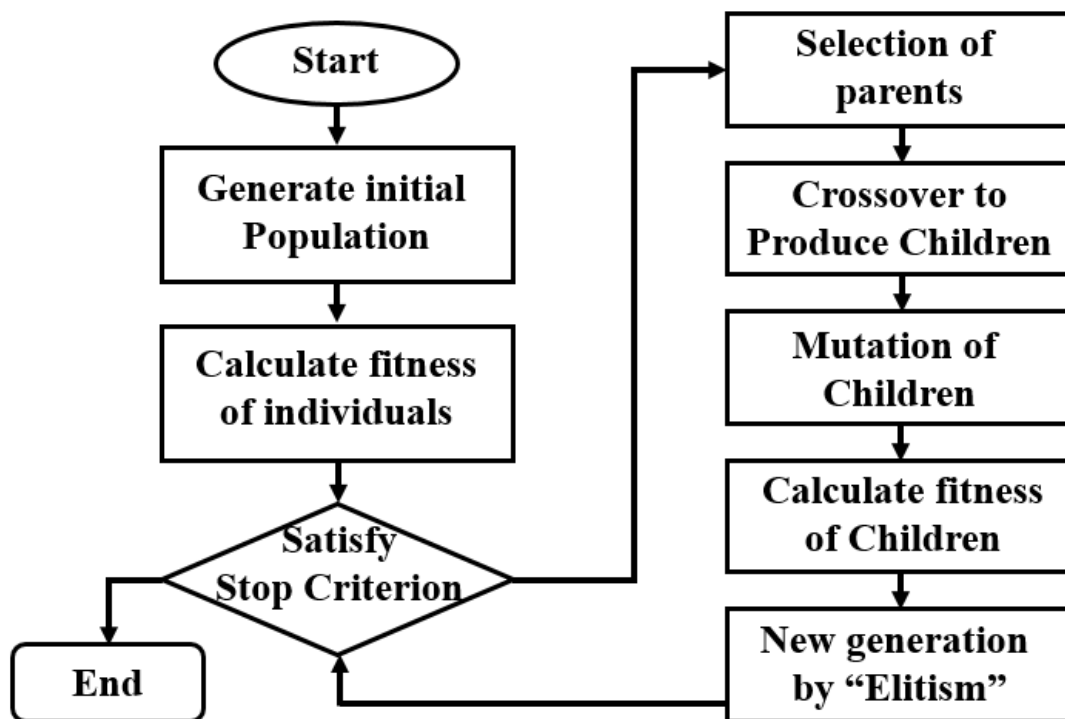


Figure 3.15: The work flow diagram of the Genetic algorithm based optimization operation.

Chapter Four

Design of the Structure and Validation of Numerical Model

4.1 Design of the Laser Structure and Selection of Material

In this work a wurzite strained nitride semiconductor based laser structure has been designed to obtain the wavelength output of communication wavelength. In previous chapters the device physics and the mathematical models are depicted elaborately. As in this work, our focus is to design an interband laser structure with wurtzite nitride based semiconductor materials, the output light wavelength depends on the transition energy gap between the conduction subbands and valence subbands. These subbands are calculated by solving the Hamiltonian matrix for conduction and valence band. In this work, a numerical method has been developed according to the theory described in chapter three. Before the evaluation of the energy subbands, we have to design a material system to obtain the desired wavelength of 1330nm. To obtain these parameter, in our design we have used InN as a well region materials. To obtain 1330nm wavelength, InN is the fittest materials because among the three nitride binaries, InN has the lowest bandgap means provide longer wavelength. This can be inferred from the following equation

$$E_g = h\nu = hc/\lambda,$$
$$\lambda(\text{in } m) = 1.2431 \times 10^{-6}/E_g(\text{eV}). \quad (4.1)$$

If we put the value of bandgap of InN from Table 4.1 in the above equation, we will get around 1800nm wavelength. But in quantum well device structure, energy subbands are never created on the band edges. We always found conduction subbands above the conduction band edge and valence subbands below the valence band edge which is depicted in chapter three. Moreover, position of the energy subbands are also well and barrier length dependent. Subband's position is shifted farther than the band edges with the change of well and barrier width. So considering all constrain, InN is the fittest nitride material for having an optical output of 1330nm wavelength.

After choosing the fittest quantum well material, we took InGaN as a barrier material. Due to the strain effect in nitride materials, the unscreened polarization fields cause a 'sawtooth' type of band diagram for the well and the barrier regions, shown in Figure 4.1. The injection of free carriers into the structures causes a partial screening of the polarization field by a spatial separation of the electron and hole gases. Thus, the transition energy is red-shifted, and the oscillator-strength is reduced due to a lower electron-hole wave-function overlap. Epitaxial growth of the nitride semiconductors in directions that have either lower polarization, or no polarization at all is being actively pursued for increasing the efficiency of light emission. Lowering the electron-hole wave-function overlap strength introduce quantum confinement stark effect. The quantum-confined Stark effect (QCSE) describes the effect of an external electric field upon the light absorption spectrum or emission spectrum of a quantum well (QW). In the absence of an external electric field, electrons and holes within the quantum well may only occupy states within a discrete set of

energy subbands. Consequently, only a discrete set of frequencies of light may be absorbed or emitted by the system. When an external electric field is applied, the electron states shift to lower energies, while the hole states shift to higher energies. This reduces the permitted light absorption or emission frequencies. Additionally, the external electric field shifts electrons and holes to opposite sides of the well, decreasing the overlap integral, which in turn reduces the recombination efficiency of the system.

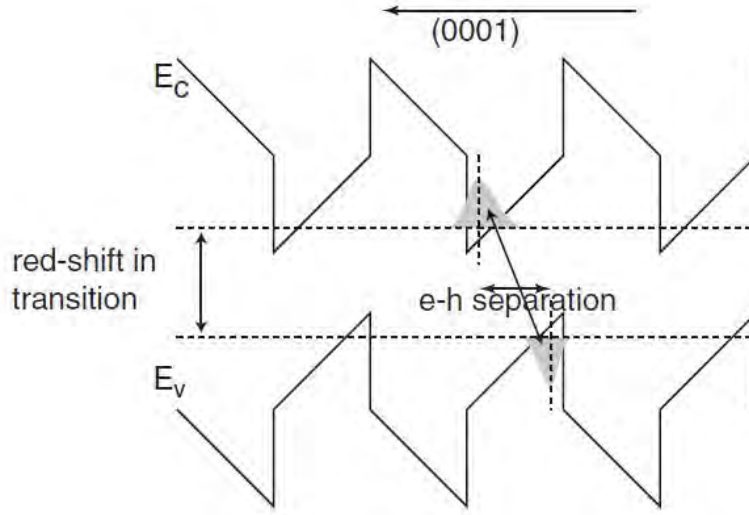


Figure 4.1: Polarization induced red-shift and reduction of oscillator strength in optical devices [62].

To calculate the oscillator strength, we can use [62]

$$f_{osc} = \frac{2}{m_e \hbar \omega_{cv}} \| u_c | \mathbf{p} \mathbf{e} | u_v \rangle \|^2 \left| \int f_e(z) f_h(z) dz \right|^2. \quad (4.2)$$

Here, \mathbf{p} is the electron momentum operator and \mathbf{e} is the unitary polarization vector, m_e is the free electron mass and $\hbar \omega_{cv}$ is the energy of the interband transition (usually the transition e_1-hh_1 in type I heterostructures, that between the first electron QW state (e_1) and the first heavy hole QW state (hh_1)). $\left| \int f_e(z) f_h(z) dz \right|^2$ is the square modulus of the overlap integral between electron and hole wave functions. In our work, with InN-InGaN we have used GaN as a SCH (Separate Confinement Hetero-structure) material to provide a good optical and carrier confinement. SCH is a layer of lower refractive index as well as higher bandgap with respect to well and barrier layer. As a results, SCH provides better confinement for both carrier and photon. Moreover, the thickness of this layer has impact on the energy band level and carrier distribution in well region [76, 77]. In this work, the effect of well, barrier and SCH layer thickness on the optical characteristics has been studied with the developed numerical model. So thickness of these layers has been calculated through the optimization of the optical characteristics. Before the calculation of the optical characteristics of the designed structure, we have calculated the electronic properties of the structure utilizing the developed numerical method described in chapter 03. Whole model is developed by using MATLAB and verified with previously published results. For the performance

of the electronic properties of the structure, the material parameters are taken from ref. [17, 23, 38, 55, 63].

Table 4.1: The material parameter Table for GaN, AlN and InN

Parameters	GaN	AlN	InN
Lattice Constant (\AA)			
a	3.189	3.112	3.545
c	5.185	4.982	5.703
Energy Parameters			
E_g (eV) at 0K	3.510	6.10	0.69
E_g (eV) at 300K	3.437	6.00	0.608
α (meV K ⁻¹)	0.914	2.63	0.414
β (K)	825	2082	154
Δ_1 (= Δ_{cr}) (eV)	0.010	-0.227	0.024
$\Delta_2 = \Delta_3 = \Delta_{so}/3$ (eV)	0.00567	0.012	0.00167
Conduction band effective masses			
$m_{//}^*/m_0$ at 300K	0.21	0.32	0.07
m_{\perp}^*/m_0 at 300K	0.20	0.30	0.07
Valence band effective mass parameter			
A_1	-7.21	-3.86	-8.21
A_2	-0.44	-0.25	-0.68
A_3	6.68	0.58	7.57
A_4	-3.46	-1.32	-5.23
A_5	-3.40	-1.47	-5.11
A_6	-4.90	-1.64	-5.96

$A_7(\text{eV } \text{\AA})$	0.0937	0	0
Deformation potentials (eV)			
$a_{cz}(\text{eV})$	-7.1	-3.4	-4.2
$a_{ct}(\text{eV})$	-9.9	-11.8	-4.2
$D_1(\text{eV})$	-3.6	-2.9	-3.6
$D_2(\text{eV})$	1.7	4.9	1.7
$D_3(\text{eV})$	5.2	9.4	5.2
$D_4(\text{eV})$	-2.7	-4.0	-2.7
$D_5(\text{eV})$	-4.0	-3.4	-4.0
$D_6(\text{eV})$	-5.5	-3.4	-5.5
Elastic stiffness constants			
$C_{11}(\text{GPa})$	390	396	223
$C_{12}(\text{GPa})$	145	137	115
$C_{13}(\text{GPa})$	106	108	92
$C_{33}(\text{GPa})$	398	373	224
$C_{44}(\text{GPa})$	105	116	48
Piezoelectric coefficients			
$d_{13}(\text{pmV}^{-1})$	-1.0	-2.1	-3.5
$d_{33}(\text{pmV}^{-1})$	1.9	5.4	7.6
$d_{15}(\text{pmV}^{-1})$	3.1	3.6	5.5
Spontaneous polarization			
$P_{sp}(\text{C/m}^2)$	-0.034	-0.090	-0.042

The linear interpolation formula for determining the material parameter of nitride ternary materials from binary nitrides is as below [52]

$$T(A_xB_{1-x}N) = xB(AN) + (1 - x)B(BN). \quad (4.3)$$

This formula is used for most of the parameters except for the bandgap energy, which has a bowing parameter [52]. Like for $\text{Al}_x\text{Ga}_{1-x}\text{N}$, the bowing parameter's value is 0.98 eV. So,

$$E_g(\text{Al}_x\text{Ga}_{1-x}\text{N}) = xE_g(\text{AlN}) + (1 - x)E_g(\text{GaN}) - 0.98x(1 - x). \quad (4.4)$$

In this work, bowing parameter of InGaN for gamma energy band calculation is taken as 1.4 eV [31] and for spontaneous polarization calculation is -0.037C/m^2 [31]. And the band offset is taken as ΔE_c : $\Delta E_v = 0.7:0.3$. In some literature, it is shown that full polarization effect is not active in calculation of device performances. Here, it is considered that only 75% of polarization effect is effective to determine the device characteristics.

4.2 Band Energy Profile of the Laser Structure

In our work, we have only studied single quantum well structure. Here, for the demonstration of electronic properties, total device length has taken as 150\AA where well thickness is 12\AA and barrier thickness is 15\AA . Rest of the device thickness is the SCH's thickness. Using these values from the simulation of the developed numerical model we have found the following band profile of the designed laser structure. Here, valence band reference voltage of quantum well is taken as 0 and with respect to this reference other energy level has been calculated. All the strain component has been calculated with respect to GaN layer. Here, InGaN is experienced a compressive strain of 2.72% and in the well region, InN is experienced 7.53% compressive strain. As a result, the energy bandgap in both well and barrier regions is increased in value. The obtained energy band profile considering only strain effect without polarization has been shown in Figure 4.2.

In nitride semiconductor materials, polarization is an inherent characteristics. Two types of polarizations have been found in nitride materials: one is spontaneous polarization and other is piezoelectric polarization. Origin of these polarization has been illustrated in the previous chapter. Using the material parameters of Table 4.1, polarization effect has been calculated for our structure. Polarization creates an internal electric field in all region which turns the previous band structure into a saw tooth like band structure. In some literature, it has been considered that only a portion of polarization effect became active in the calculation of band profile. In this work, complete polarization effect has been taken into account. Considering the constrains discussed in chapter Three, energy band profile has been performed by numerical method which is shown in Figure 4.3. The obtained values of internal electric field are 1.97 MVcm^{-1} , -2.41 MVcm^{-1} , and -11.7 MVcm^{-1} for SCH, barrier and well region respectively.

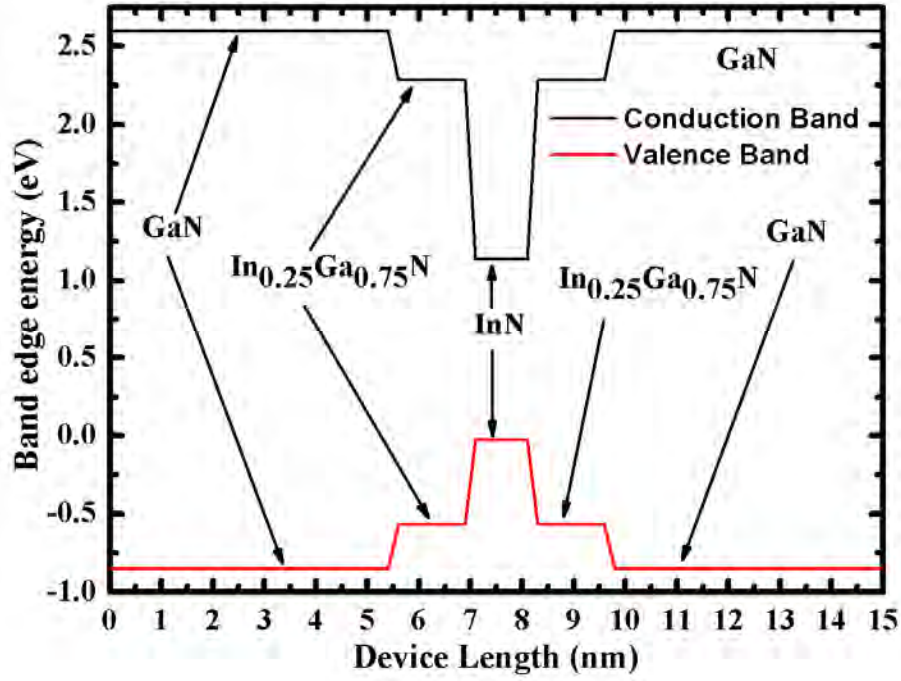


Figure 4.2: Energy band profile of InN-InGaN quantum well structure with strain effect. Red line represents the conduction band edge and blue line is the valence band edge.

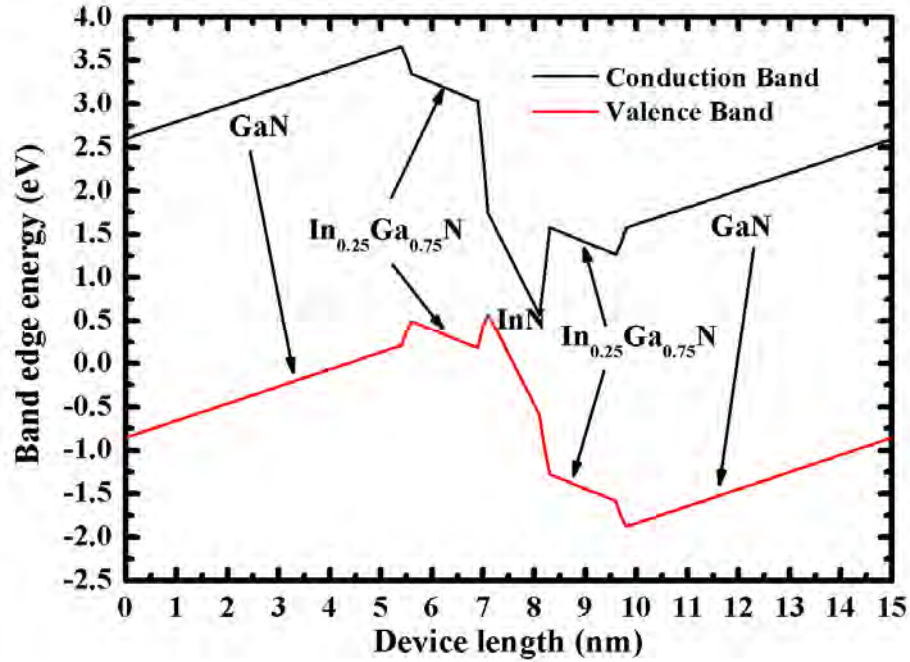


Figure 4.3: Energy band profile of InN-InGaN quantum well structure with strain effect and polarization induced internal electric field. Black line represents the conduction band edge and red line is the valence band edge.

4.3 Work Flow of the Numerical Model

After having the band energy profile, using conduction band Hamiltonian and valence band Hamiltonian described in chapter three, Self-consistent analysis which includes both Schrodinger and Poisson equation has been performed using the developed numerical model utilizing MATLAB. Here, for conduction band and valence band Schrodinger equation, different Hamiltonians are solved. For valence band, 6-band $\mathbf{k}\cdot\mathbf{p}$ method based Hamiltonian including valence band mixing, strain effect, spontaneous and piezoelectric polarization has been developed using the mathematical model of chapter three and using the material parameter of Table 4.1. The numerical flow chart to compute the spontaneous emission and optical gain of III–Nitride semiconductor nanostructure is shown in Figure 4.4. Based on the general formalism for the calculation of the band structure for semiconductor heterostructure / nanostructure (like quantum well or quantum dots systems), finite difference method is used to solve the Schrödinger equations. The spatial interval for the finite difference method is 1 Å. The final band-edge potential has to be solved self-consistently due to the interdependent of the carrier distribution and band-edge potential. Therefore, a closed loop is formed to solve the Schrödinger equations and Poisson equation alternately until the Eigen energy converges. Then the wave functions are simultaneously solutions for both Schrödinger and Poisson equations. In the self-consistent calculation, the convergence condition is set such as the error of the Eigen energy converge to less than 0.1%, which requires 4 to 8 iterations for each carrier density computation. After having the energy states for the designed structure, optical transition matrix elements have been performed to obtain the interband transitions which eventually provide the emission light.

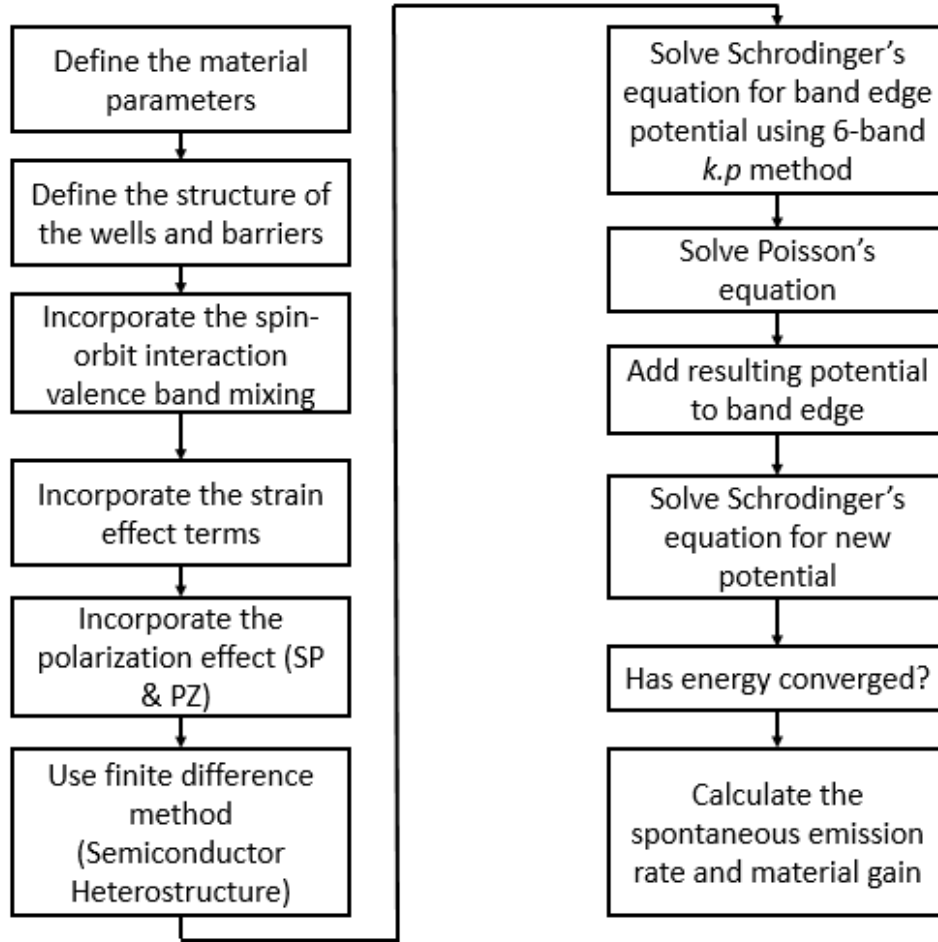


Figure 4.4: Numerical flow chart of the simulation process for self-consistent model of 6-band $k.p$ Hamiltonian for wurtzite nitride semiconductor quantum well active region.

With the obtained optical transition matrix element for TE and TM polarization, spontaneous emission rate, material gain, radiative recombination current density etc. are calculated to analysis the device performance. Analysis of the device characteristics and comparison with other work are provided in next chapter.

4.4 Validation of the Numerical Model

To verify the developed numerical model for the thesis work, we have taken the published results of [55, 78]. In both works, same numerical model has been adopted to get their results. In [55], a numerical model has been developed for GaN-Al_xGa_{1-x}N quantum well laser. In this work, polarization effect was not incorporated into the numerical model. The author performed the model for two different QW with two different well widths. First QW had well width of 26Å and second QW had 50Å well width. Most of the numerical model of my work has been developed by following this ref. So, to verify my model, we first perform the simulation taking similar device structure mentioned in [55]. The performed results and the published results are shown side by side in the following figures. In [55], finite difference method has been utilized to solve the energy levels with 2Å interval where in our work the interval is 1Å. In Figure 4.5, first our calculated the valence band energy levels for 26Å GaN well layer along with 62Å Al_{0.3}Ga_{0.7}N barrier layers are shown with the published result of [55]. As the reference band edge are different in two works so energy levels are not in same value but their patterns and position differences are same.

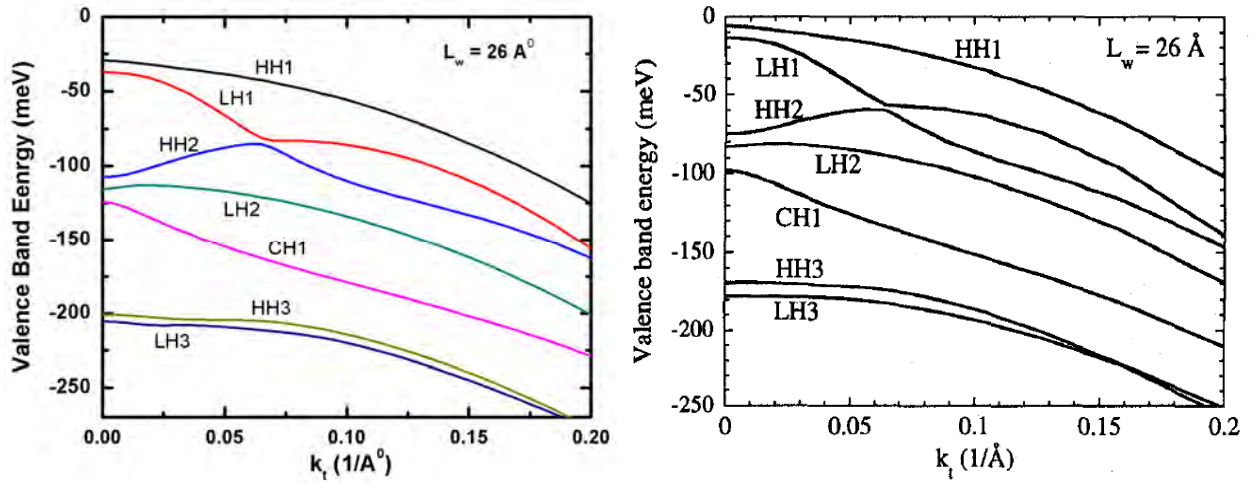


Figure 4.5: Comparison between the performed result (left) and published result (right) for valence band energy of 26Å GaN well layer with Al_{0.3}Ga_{0.7}N barriers.

Same performance has been done with another structure of same material system given in [55]. The well width is 50Å for this structure along with 50Å Al_{0.3}Ga_{0.7}N barrier layers. The comparative illustration has been shown in Figure 4.6. From Figure 4.5 and 4.6, it is shown that that a thick well has closer spacing between the subband energies than those of the thin well. Thin well layer has significant effect on optical gain of the structure.

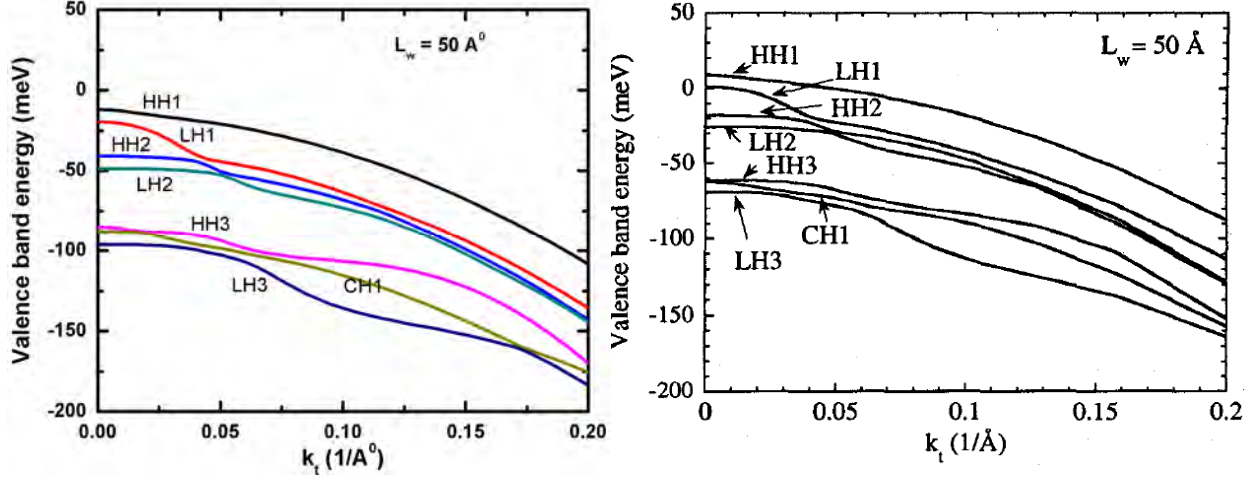


Figure 4.6: Illustration of comparison between valence band energy levels of 50Å GaN - 50Å $\text{Al}_{0.3}\text{Ga}_{0.7}\text{N}$ Quantum well structure. Left figure is performed with our developed model and right figure is published in [55].

After comparing the electronic characteristics, we have also compare the optical characteristics with the published result in [55]. In the published work, the author had been calculated the dispersion of momentum matrix elements of TE and TM polarization as a function of the in-plane wavenumber k_{\parallel} for 62Å $\text{Al}_{0.3}\text{Ga}_{0.7}\text{N}$ -26Å GaN-62Å $\text{Al}_{0.3}\text{Ga}_{0.7}\text{N}$ structure. Matrix elements were calculated for the first conduction subband (C1) to the first heavy-hole (HH1), the light-hole (LH1), and the crystal-field split-hole (CH1) transitions. Considering the same conditions, we have also performed the same momentum matrix elements. In Figure 4.7, the comparison result between the published and obtained momentum matrix elements for TE polarization has been shown. In both figures, the C1-HH1 and C1-LH1 transitions have strong TE components near the zone center. In Figure 4.8, comparison of momentum matrix elements for TM polarization has been depicted where the C1-CHI transition has a dominant TM component.

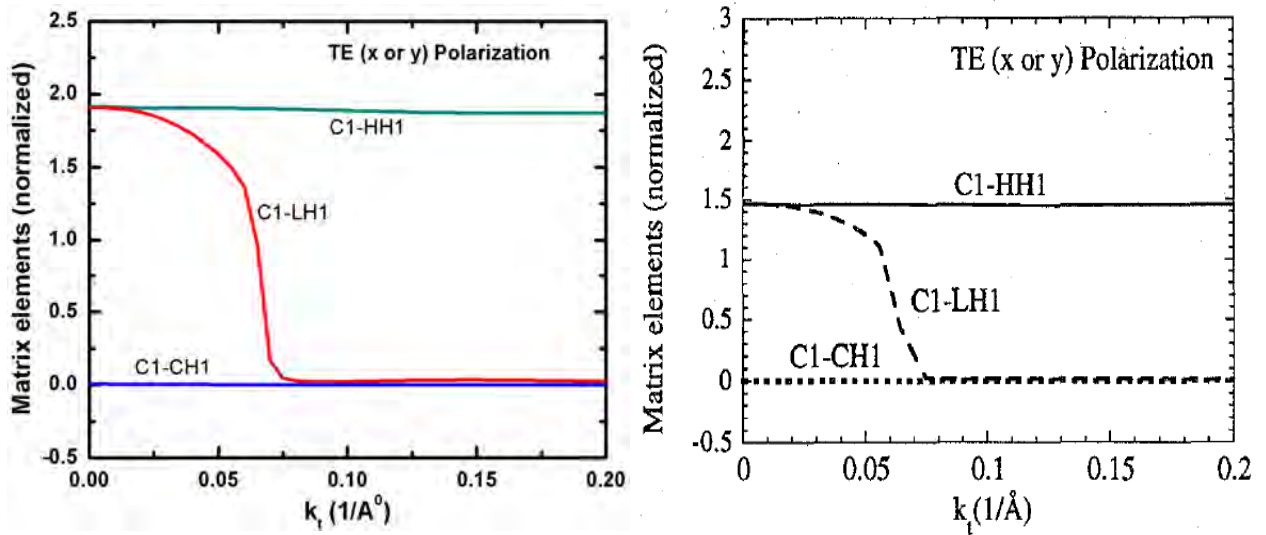


Figure 4.7: Comparison between obtained (left) and published (right) result of normalized momentum-matrix elements for the first conduction (C1) subband to the HH1, the LH1, and the CH1 subband transitions for

TE polarization (on the x-y plane, which is perpendicular to the c axis (=z axis)) for a well width $L_w = 26 \text{ \AA}$.

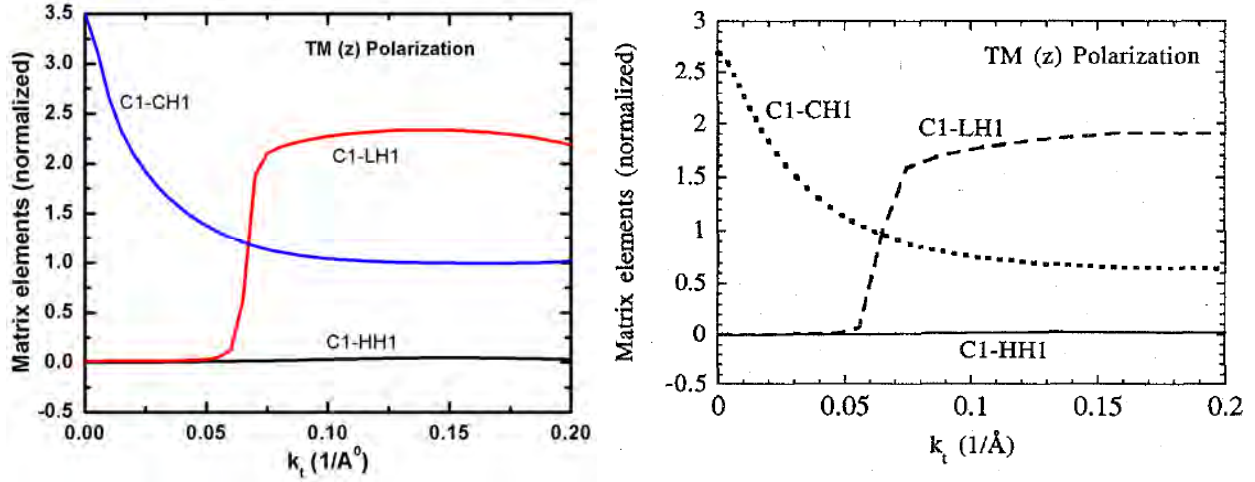


Figure 4.8: Comparison between obtained (left) and published (right) result of normalized momentum-matrix elements for the first conduction (C1) subband to the HH1, the LH1, and the CH1 subband transitions for TM polarization (on the z axis) for a well width $L_w = 26 \text{ \AA}$.

After comparing momentum matrix elements, spontaneous emission spectrum and optical gain for the two above structures has been compared with the performed result. Keeping similarities we have obtained the spontaneous emission rate and optical gain for the same structures and shown the comparison in same manner. In Figure 4.9, comparison of spontaneous emission rate and optical gain for 26\AA QW has been shown and in Figure 4.10 comparison of same optical characteristics for 50\AA has been given. In right-side figures, the solid curves are for the TE polarization and the dashed curves for the TM polarization. For left-side figures, green and red lines are for TM polarization and blue and black lines are for TE polarization. A narrow well has a larger separation of subbands, resulting in sharper gain and spontaneous emission spectra than those of a wider well. It is clearly seen that the TM polarized gain is very small, as expected from the valence subband structures, since the HH and LH subbands contribute mostly to TE polarization.

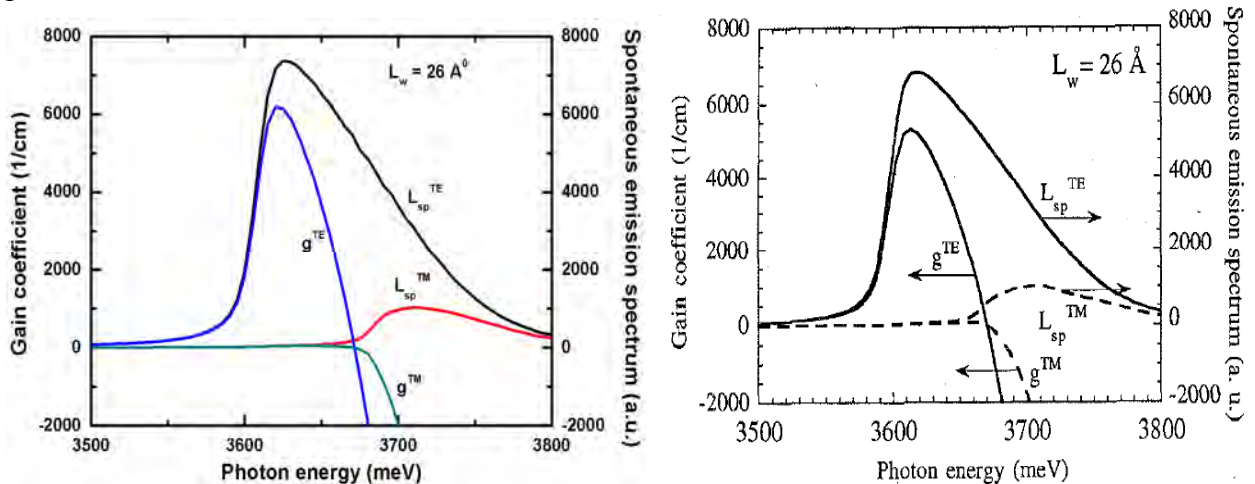


Figure 4.9: Illustration of gain co-efficient and spontaneous emission rate spectrum of GaN-AlGa_{0.2}N for 26Å well width. Left figure is performed with our developed model and right figure is published in [55].

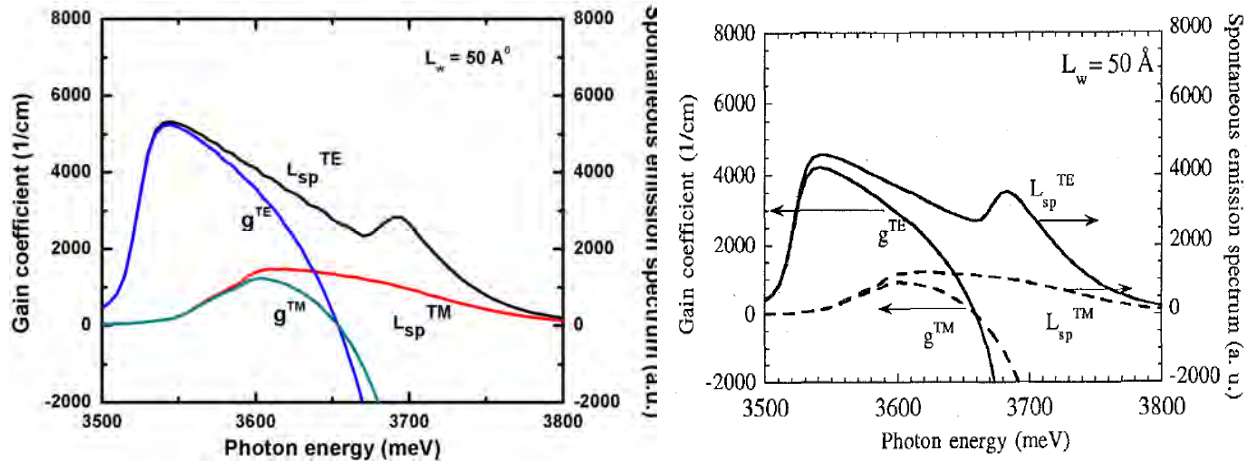
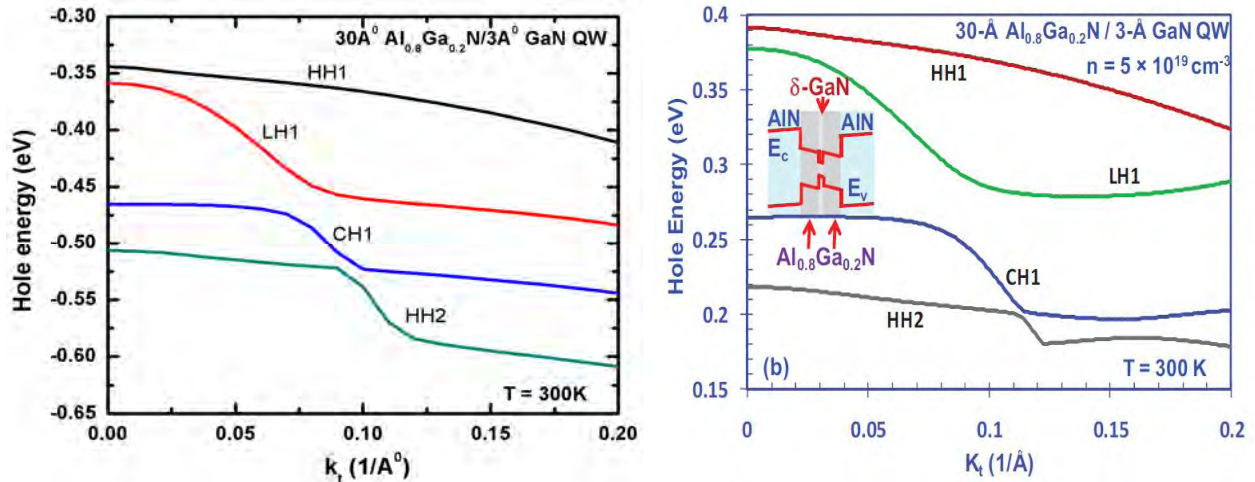


Figure 4.10: Illustration of gain co-efficient and spontaneous emission rate spectrum of GaN-AlGa_{0.2}N for 50Å well width. Left figure is performed with our developed model and right figure is published in [55].

Second verification has been done with [78] where the authors were worked with AlGa_{0.2}N-delta GaN quantum well laser to obtain large optical gain with respect to conventional AlN-AlGa_{0.2}N quantum well laser. The authors showed the improvement of inserting delta layer into a conventional well layer in their work. As their improved structure was similar to our designed structure, for verification we only consider their improved structure and corresponding results. First in Figure 4.11, comparison between performed and published result regarding valence band energy or hole energy states of 30Å Al_{0.8}Ga_{0.2}N well region with 3Å GaN delta layer has been illustrated. Generally inserting a delta layer into a well region results shifting hole energy level into higher state means producing light output of higher emission wavelength or lower photon energy. As the reference valence band edge is not same between two works, the relative energy level positions are not same. Moreover, in [78] parameter values are not available like [55]. So perfect reproducing cannot be obtained for this validation. One limitation in our model is not to



include the carrier screening effect and polarized induced carrier density into Poisson's equation which gives some deviation into the figure.

Figure 4.11: Illustration of comparison between performed (left) and published (right) result of hole energy levels of 30Å Al_{0.8}Ga_{0.2}N / 3Å GaN QW for T = 300K. Device structure is shown in right figure.

In Figure 4.12, the performed optical gain for two material systems for both TE and TM polarization has been compared with the same published result. Optical gain has been calculated for 30Å Al_xGa_{1-x}N / 3Å GaN delta layer with AlN barriers at T = 300K for $5 \times 10^{19} \text{ cm}^{-3}$ injection carrier density. The solid lines in the figures are TE polarization lines where dot line represents TM Polarization lines. From following figure, it can be concluded that though the hole energy levels are not found into same energy states with compare to the published result but the relative positions and the energy difference between hole and electron levels are identical. Without this the emission wavelengths will not be identical. According to [78], the obtained large optical gain for TE Polarization has been found 4442 cm^{-1} at $\lambda_{\text{peak}} = 253.6 \text{ nm}$ for 30 Å Al_{0.7}Ga_{0.3}N / 3 Å GaN and 3537 cm^{-1} at $\lambda_{\text{peak}} = 245.1 \text{ nm}$ for Al_{0.8}Ga_{0.2}N / 3 Å GaN. From the performance of our simulation model, the obtained large optical gain for TE Polarization has been obtained 4379.48 cm^{-1} at $\lambda_{\text{peak}} = 256 \text{ nm}$ for 30 Å Al_{0.7}Ga_{0.3}N / 3 Å GaN and 3723.18 cm^{-1} at $\lambda_{\text{peak}} = 246.4 \text{ nm}$ for Al_{0.8}Ga_{0.2}N / 3 Å GaN. This slight discrepancy has been arose from the deviation of energy states due to difference in numerical model for calculating electronic characteristics of a structure.

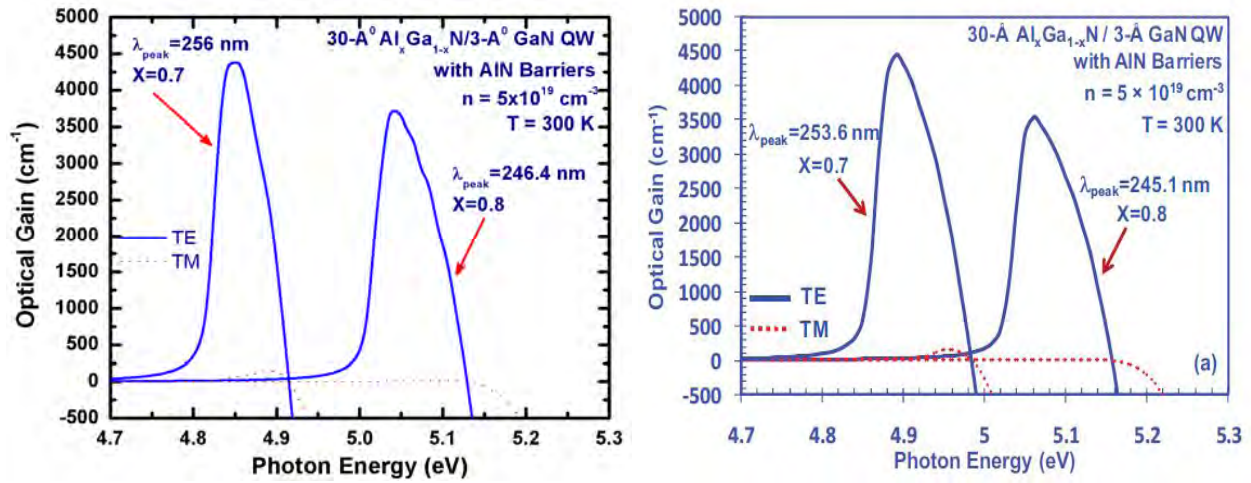


Figure 4.12: Illustration of optical gain for TE polarization and TM polarization of 30Å Al_xGa_{1-x}N / 3Å GaN delta layer with AlN barriers at T = 300K for $5 \times 10^{19} \text{ cm}^{-3}$ injection carrier density. The left figure has been performed with our developed numerical model and the right figure has been published in [78].

Chapter Five

Analysis of the Laser Characteristics

As mentioned into Chapter One, nitride based quantum well structure design at communication wavelength has hardly seen and most of the published works on design nitride Laser at this spectrum are intersubband transition device like Quantum Cascade Laser (QCL). But, our aim is to design nitride based interband transition Laser structure at communication wavelength. So far we have investigated the published works on these area, we have found a suggestion made in [31]. The authors of [31] were mentioned that they have found around 1330nm emission wavelength for 10Å InN as well thickness and 30Å In_{0.25}Ga_{0.75}N as barrier thickness. Authors were showed the relationship between well thickness and transition wavelength. As no detail analyses are found in [31], we have to analysis our work with others published works [31-33, 55, 63-64 and 78].

5.1 Calculation of Electronic Band Structure

To calculate the band structure for the Laser structure, we have performed our developed model with material parameters given in Table 4.1. In numerical model, we have utilized two Hamiltonians discussed in Chapter Three. To solve the Hamiltonian, in this work, we utilize ‘eigs’ command to evaluate the Eigen function and Eigen vector with sparse matrix idea to reduce the simulation complexity. In laser structure, it is considered that only the energy subbands created into the well region have most dominating effect on the optical transition matrix elements as well as optical characteristics of the device. In our developed method, we have calculated 8 conduction subbands and 24 valence subbands. In Figure 5.1, 5.2 and 5.3, the performed energy subbands for conduction band and valence band (Upper and Lower Hamiltonian) respectively are shown. In case of valence subbands, to determine the band type (HH or LH or CH) we have calculated the square value of the area of the envelop function (g_m^1, g_m^2, g_m^3 for upper Hamiltonian and g_m^4, g_m^5, g_m^6 for lower Hamiltonian) of the corresponding valence subbands. The sum of the square of the area of 3 envelop functions should be 1. The valence subband is named with the name of the envelop function which contribution to total area is largest. Like if g_m^1 has the largest contribution than subband will be named as HH (heavy hole). Same calculation is also applicable for lower Hamiltonian to determine its valence subbands. Figure 5.2 and 5.3 show the details of the valence band subbands. Due to the strong valence band mixing effect for our structure, HH and LH bands have higher energy value than CH band. Though, at zone center HH and LH bands are not showed any separation in energy level. As it is mentioned in chapter three that Upper and Lower Hamiltonian will provide same results with only a reflection symmetry. This phenomena is illustrated by the following figures. Generally spacing between energy states depends on the thickness of the well layer. Thick well has closer spacing between the subband energies than those of the thin well. For the quasi-two-dimensional nature of the density of states to play a significant role on the optical gain of a QW laser, a thin well is desirable, especially because the hole effective masses of InN are very heavy. However, a thin well reduces the modal gain; therefore, multiple

quantum wells are required. Comparing with [63], Figure 5.2 gives almost similar valence subband energy levels. The structure of [63] was $\text{In}_{0.28}\text{Ga}_{0.72}\text{N}$ -GaN while our structure is InN - $\text{In}_{0.25}\text{Ga}_{0.75}\text{N}$ -GaN.

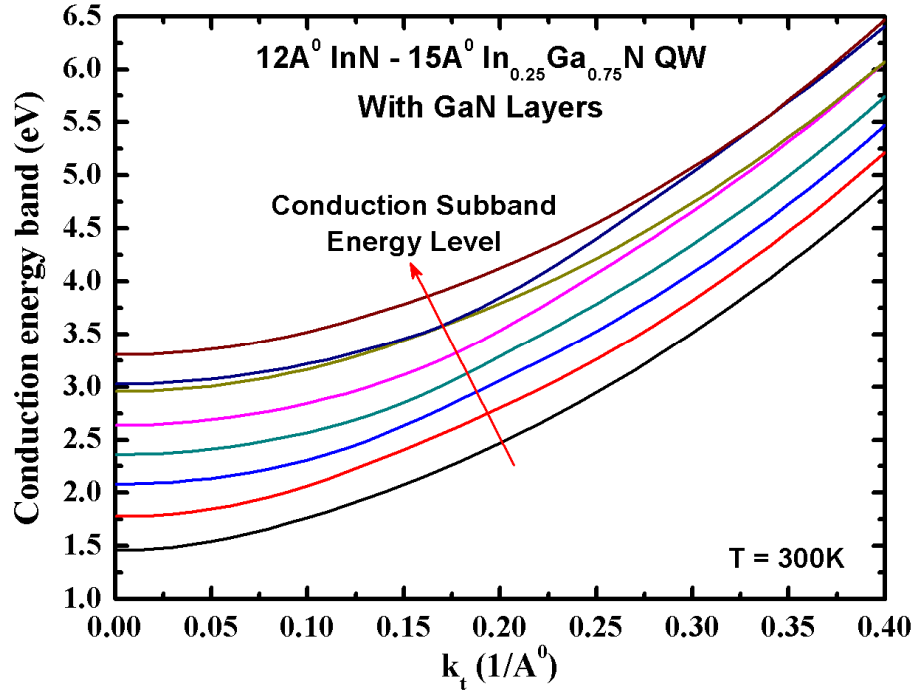


Figure 5.1: Obtained conduction subband energy levels for the laser structure with respect to wave vector, k_t . Here 8 conduction subbands are illustrated.

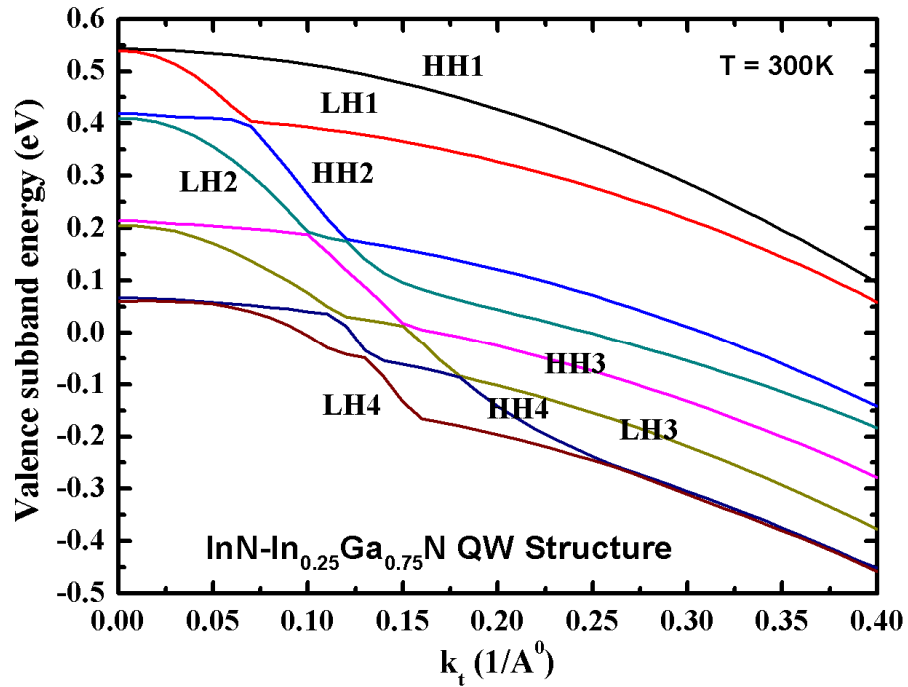


Figure 5.2: Obtained valence subband energy for the laser structure with respect to wave vector, k_t . Here only 8 valence subbands are illustrated with their subband characteristics.

In Figure 5.3, obtained valence subbands energy from lower Hamiltonian are shown with their respective band names. From the figure is shown that both upper and lower Hamiltonian gives the same subbands energy levels which has been mentioned in [55].

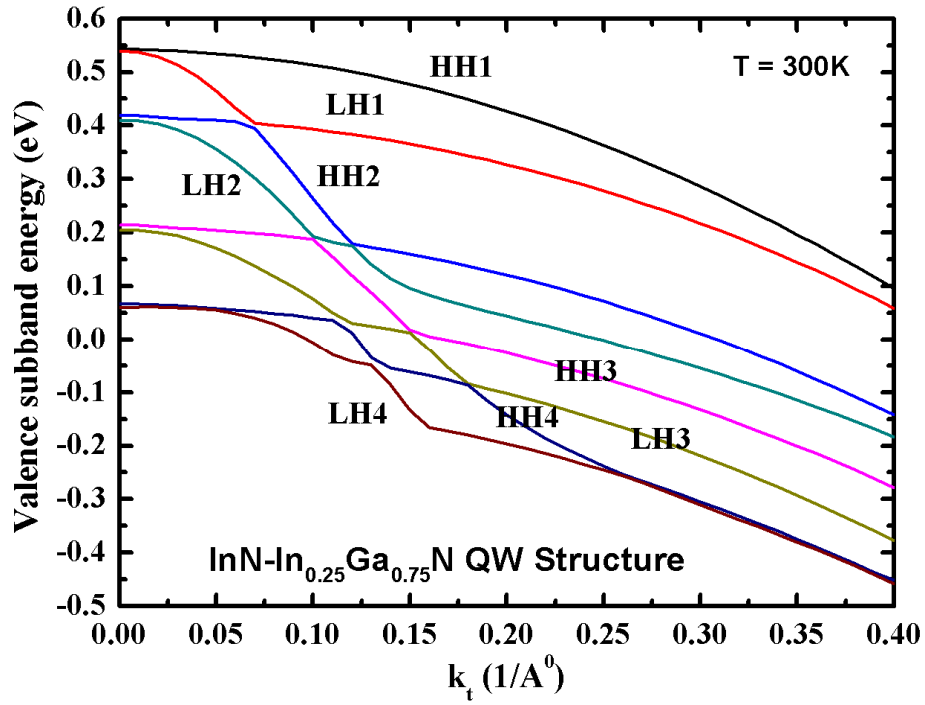


Figure 5.3: Obtained valence subband energy of lower Hamiltonian for the laser structure with respect to wave vector, k_t . Here only 8 valence subbands are illustrated with their subband characteristics.

In Figure 5.4, the area calculations and corresponding contributions of the three bulk material's valence subband (g_m^1, g_m^2, g_m^3 for upper Hamiltonian) for first subband of our structure are shown. Valence subband is determined by observing $k_t = 0$ position.

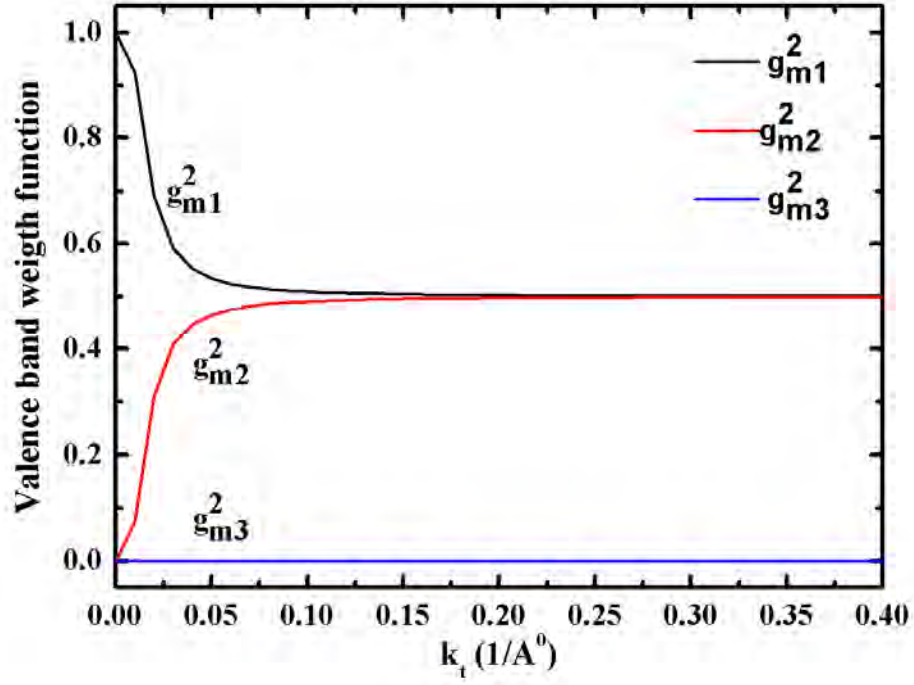


Figure 5.4: Weight functions of the envelop function of Upper Hamiltonian are shown.

Along with the calculated energy subbands, wave function for both conduction and valence band subbands are also obtained from the developed model. The obtained results are demonstrated in the Figure 5.5 to Figure 5.9. In Figure 5.4, 4 consecutive conduction wave functions are shown along with their corresponding energy subband levels with respect to device length. In our designed structure, first energy level of conduction subband is found at 1.457 eV. The second, third and fourth conduction subband energy levels are 1.78 eV, 2.08 eV and 2.36 eV respectively.

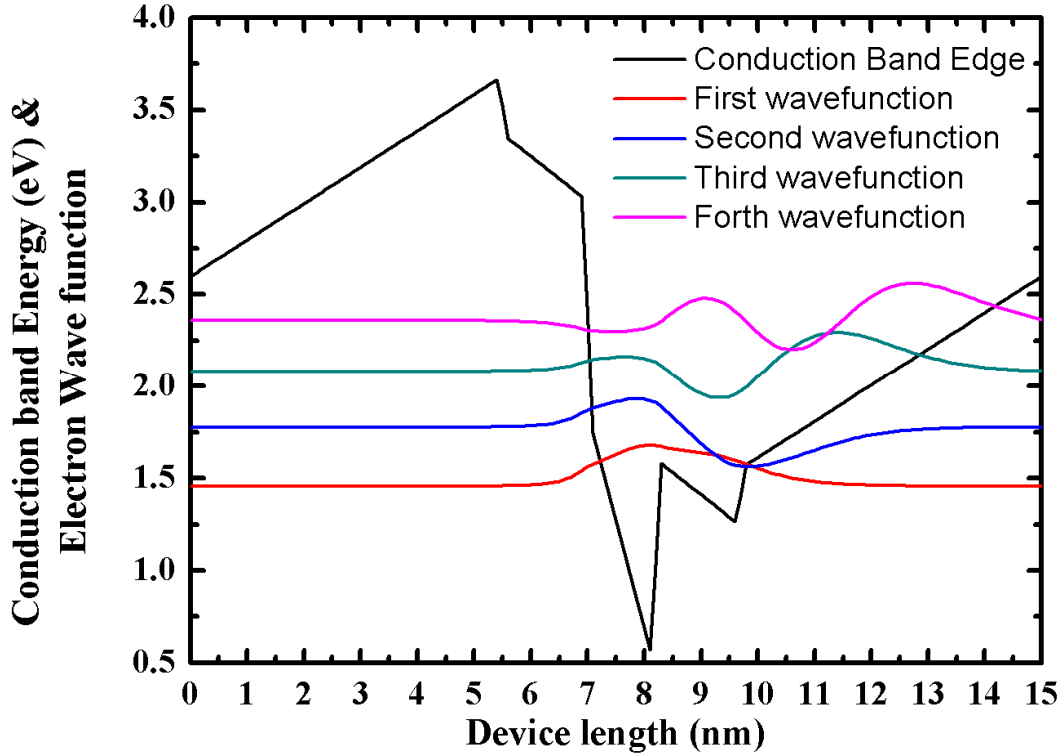


Figure 5.5: Conduction subband energy levels with their corresponding wave functions formed in the quantum well of conduction band.

In above figure, it has been seen that how electron probability wave-function has distributed within conduction band well region. Due to presence of internal electric field, all probability density function have been shifted towards lower energy levels (in our case at right side). This shifting phenomena is a common characteristics of nitride based device structure. Comparing with [31], energy band edge profile and first electron wavefunction of conduction band shows a good agreement. Other wavefunctions are determined in same manner.

In Figure 5.6, whole E-k diagram for InN-InGaN quantum well laser structure has been illustrated which is direct bandgap type. In this figure only 2 consecutive conduction energy subbands and 3 consecutive valence energy subbands are shown. From the figure, it is found that conduction band minima is at 1.457 eV and valence band maxima is at 0.544 eV. In Figure 5.7, new energy band edge profile of the designed laser structure has been shown. This profile has been obtained by self-

consistent analysis where Poisson's and Schrodinger's equations are both performed. From the performance of the numerical model, the obtained quasi Fermi level for electron is 1.42 eV.

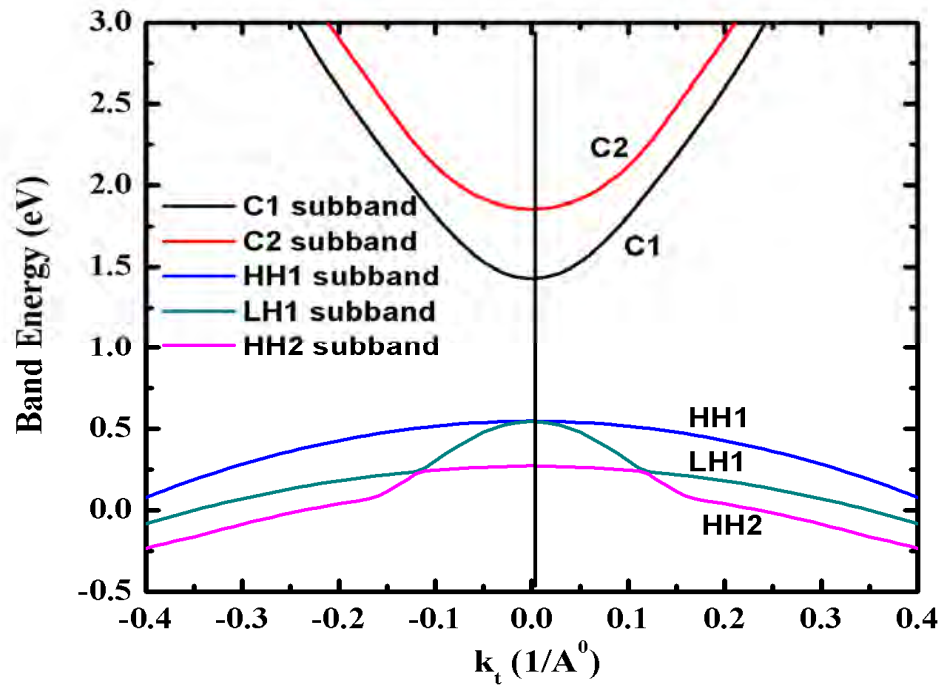


Figure 5.6: E-k diagram for 12Å InN - 15Å In_{0.25}Ga_{0.75}N quantum well structure. This is a direct bandgap type structure which provides an optical signal at around 1330nm wavelength.

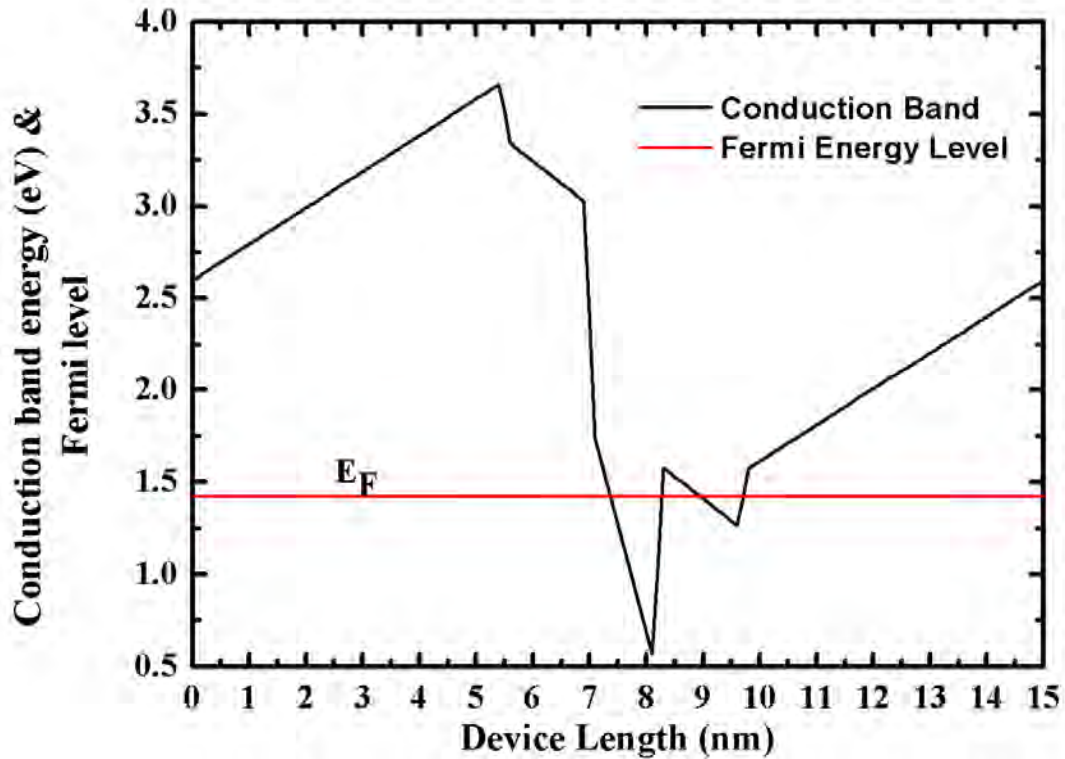


Figure 5.7: Energy band profile of the designed structure from the self-consistent analysis along with the quasi Fermi level.

From the discussion of Chapter Three, we know that valence subband in quantum well structure is formed with the mixing of the valence subbands (HH, LH and CH) of bulk structure. Moreover, from the solution of the 6-band $k.p$ Hamiltonian we get 6 wave vector for single device point. Here, device point means a node considered into the structure. In this work, we divide the structure into 150 points for which the Hamiltonian matrix become 453 by 453 matrix ($3*N+3$, where N is number of points). Among them 3 for upper Hamiltonian and 3 for lower Hamiltonian. And upper and lower Hamiltonian wave vectors are same in nature with reflection symmetry. According to the mathematical model, from the solution of valence band Hamiltonian we have found gm^1 , gm^2 , gm^3 , gm^4 , gm^5 and gm^6 . In Figure 5.8, these 6 envelop functions for 1st valence subband for $k = 1$ point has been shown. As gm^1 and gm^4 , gm^2 and gm^5 and gm^3 and gm^6 are symmetrical pairs, only first two pairs are shown in Figure 5.8.

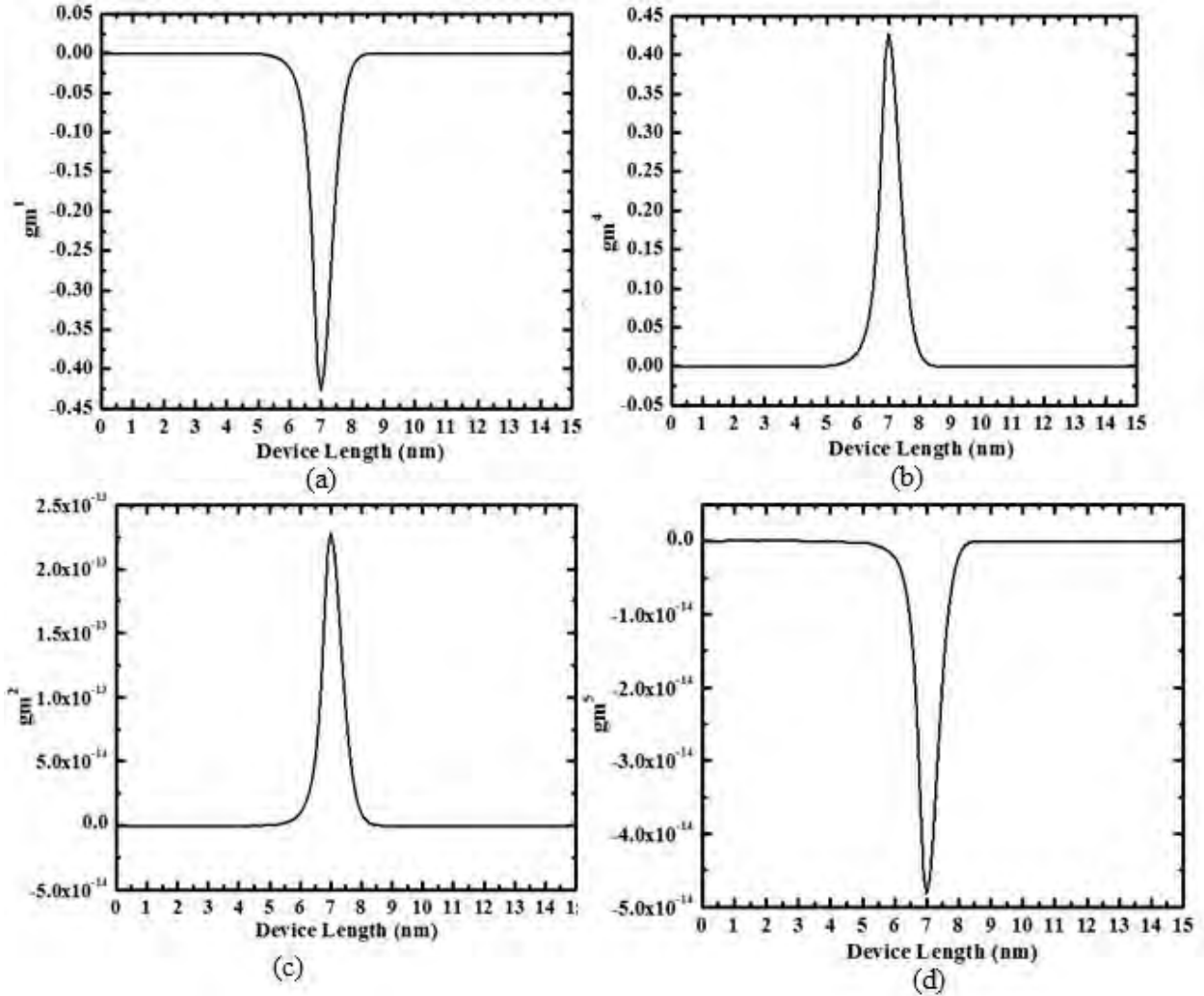
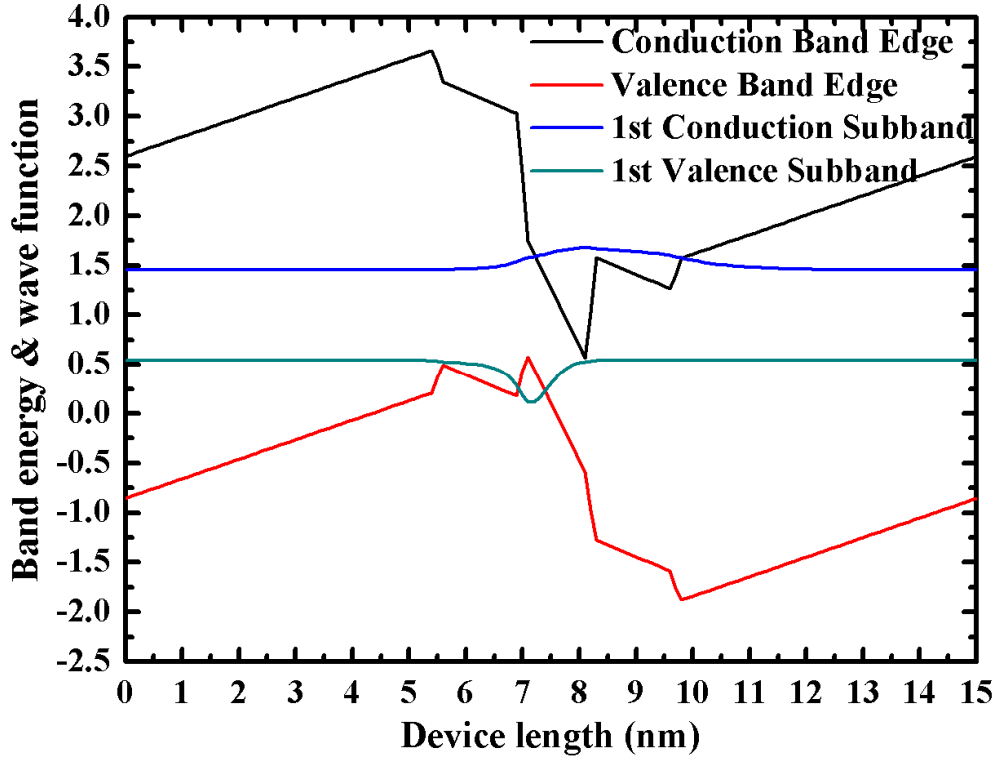


Figure 5.8: Four envelop functions obtained from the solution of k.p based Hamiltonian for the designed laser structure for first valence subband at $k = 1$. (a) gm^1 , (b) gm^4 , (c) gm^2 and (d) gm^5 .

In this work, our goal is to design a quantum well laser structure with wurtzite based nitride semiconductor whose output light wavelength will be around 1330 nm. From the performance of the simulation of the developed numerical model, we found that, 1st conduction subband created at 1.457 eV and 1st valence subband created at 0.544 eV. So transition energy is 0.9135 eV. In a laser structure, total spontaneous emission rate is depend on the oscillator strength hence on the overlap integral of electron-hole wave functions. Due to the polarization fields, the electron and hole functions are confined in opposite directions leading to reduction of the electron-hole wave



function overlap. On this factor, radiative recombination rate and radiative efficiency are dependent. In Figure 5.9, the first conduction and valence subbands are shown with respect to the device length. From the electron and hole wave functions, we have found the value of e1-hh1 wave function overlap integral of 43.27%. In [31], the obtained wave functions overlap factor was 44% which is very much nearer to our obtained value. Moreover, illustration of the overlap factor between electron and hole wavefunction in [31] shows a good agreement with Figure 5.9.

Figure 5.9: Illustration of electron hole wave functions overlap integral with respect to device length.

5.2 Calculation of the optical transition matrix elements

After having the electronic properties of the structure, to calculate the optical properties we have first calculated the optical transition matrix elements or the momentum matrix elements. Transition matrix elements gives the values of the optical transition strength between the energy states. From the Fermi' golden rule and the selection rule, it can be infer that which optical transitions are allowed and which are not allowed in the process of optical characteristics. In a bulk

semiconductor, the optical matrix element is usually isotropic. However, in a quantum-well or superlattice structure, the optical matrix element will depend on the polarization of the optical electromagnetic field. Generally among all optical transition combination, some transition are allowed and some are prohibited due to the symmetry properties. But in nitride based structure where spontaneous and piezoelectric polarization are present, all transitions can be took place due to the break of symmetry. From the detail discussion of the previous chapter, we developed the numerical model to calculate the optical transition matrix elements which is necessary to obtain the spontaneous emission rate as well as the optical gain of the designed structure. Polarization dependent spontaneous emission rate and optical gain phenomena can be understood by the polarization nature of the optical transition matrix elements. In Figure 5.10 and 5.11, the dispersion of the optical transition matrix elements for TE polarization and TM polarization are shown respectively as a function of in-plane wave vector (k_t). Among the all transitions, some are highlighted in the figures. From the figure, it can be asserted that in our designed structure, C1-HH1, C1-LH1 and C1-HH2 transitions are more dominating in the determination of the optical characteristics. In figure 5.10, it has been seen that C-HH and C-LH momentum matrix element are similar at the zone center ($k_t = 0$). As the increase in the wave vector, C-HH and C-LH transitions are diverged. The C1-HH1 and C1-LH1 transitions have strong TE components near the zone center. Since the compressive strain in the quantum well makes the top few valence subband HH- or LH-like, the dominant transitions for this structure are TE polarized. Generally, C-HH and C-LH have strong TE component and C-CH transition has strong TM component. Both

HH and LH bands contribute to the same TE polarization, yet at different energies result in a boarder gain spectrum.

Figure 5.10: Square of momentum matrix elements of the TE-polarization for InN (12 Å) / In_{0.25}Ga_{0.75}N (10 Å) SQW at carrier density of $4 \times 10^{19} \text{ cm}^{-3}$.

From the Figure 5.10 and Figure 5.11, it can be inferred that the designed laser structure is of TE-polarization type optoelectronic device as the magnitude of momentum matrix elements for TE-Polarization is higher than that of TM-Polarization. From the both figure, the highest value of TE-polarization has found $0.2 \times 10^{-50} \text{ kg}^2 \text{ m}^2 / \text{s}^2$ and for TM-polarization the highest value is $0.07 \times 10^{-50} \text{ kg}^2 \text{ m}^2 / \text{s}^2$ at $k_t = 0$ position. From Figure 5.11 it has been seen that at the zone center all transitions have minimum value but with increase in wave vector C2-LH2 and C2-HH2 shows strong TM components.

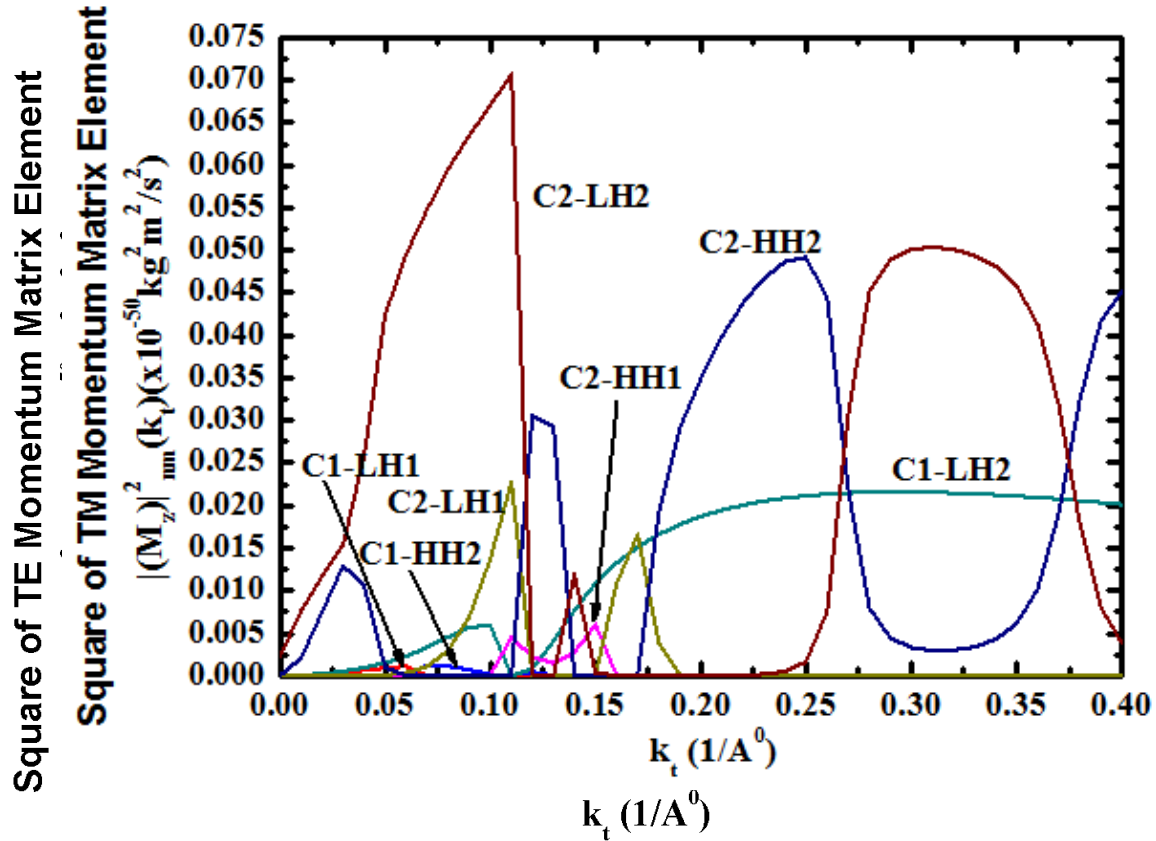
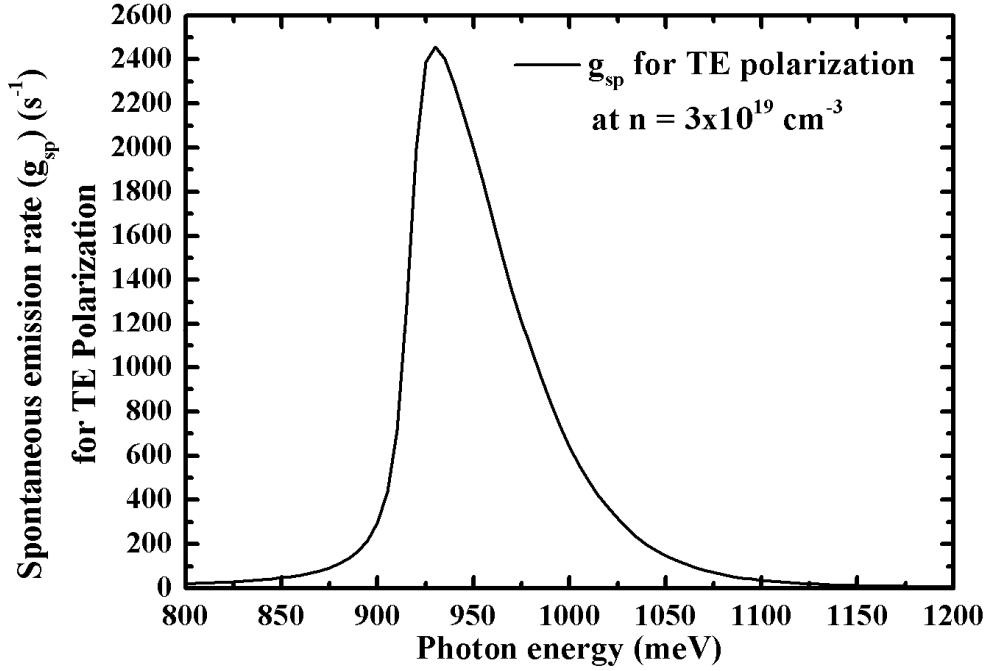


Figure 5.11: Square of momentum matrix elements of the TM-polarization for InN (12 Å) / In_{0.25}Ga_{0.75}N (10 Å) SQW at carrier density of $4 \times 10^{19} \text{ cm}^{-3}$.

5.3 Calculation of Optical Properties of the Designed Structure

After obtaining the electronic properties for the quantum well laser structure, we have obtained the optical properties from the performance of the numerical model based on the mathematical model described in Chapter Three. The simulation process has been performed with developed numerical model. From the performance, we have first obtained the spontaneous emission rate for both TE

and TM polarization. Here, spontaneous emission rate for TE polarization at $3 \times 10^{19} \text{ cm}^{-3}$ and $6 \times 10^{19} \text{ cm}^{-3}$ carrier density are shown in Figure 5.12 and 5.13 and spontaneous emission rate for



TM polarization at $3 \times 10^{19} \text{ cm}^{-3}$ and $6 \times 10^{19} \text{ cm}^{-3}$ carrier density are shown in Figure 5.14 and 5.15. In our work, the simulation temperature is 300 K. Here, the obtained Quasi Fermi level for conduction band is 1.494 eV and for valence band is 0.574 eV. From the detail mathematical illustration of Chapter Three, we have known that these spontaneous emission rate has been utilized for calculating the polarization based material gain. Generally, these figures are not shown in published work. The authors only showed the spontaneous emission spectrum and also made their literature less bulky. As here we have presented my work thoroughly, we have shown these figures step by step. In Figure 4.16, it has been found that the peak emission rate, 2456.024 s^{-1} for $3 \times 10^{19} \text{ cm}^{-3}$ carrier density is occurred at 0.93 eV (at 1336.7 nm wavelength). In Figure 5.13, spontaneous emission rate for TE polarization at $6 \times 10^{19} \text{ cm}^{-3}$ carrier density has been shown. The peak emission rate of 5945.2 s^{-1} has been found at 0.935 eV (at 1329.55 nm wavelength). Here, it is seen that with the increase in carrier density, the spontaneous emission rate has been increased as well as the peak emission wavelength has been shown a slight blue shift which is agreed with the previously published work [63, 64].

Figure 5.12: Spontaneous emission rate for TE polarization for InN-InGaN quantum well structure at $3 \times 10^{19} \text{ cm}^{-3}$ carrier density at $T=300 \text{ K}$.

Figure 5.13: Spontaneous emission rate for TE polarization for InN-InGaN quantum well structure at $6 \times 10^{19} \text{ cm}^{-3}$ carrier density at $T=300 \text{ K}$.

In Figure 5.14 and 5.15, spontaneous emission rate for TM polarization have been illustrated. As from the figure of momentum matrix element, it is obtained that the designed structure is TE polarized quantum well structure, Figure 4.18 and 4.19 also show the same observation. The peak emission rate for TM polarization for both carrier density is several order lower than that of TE polarization.

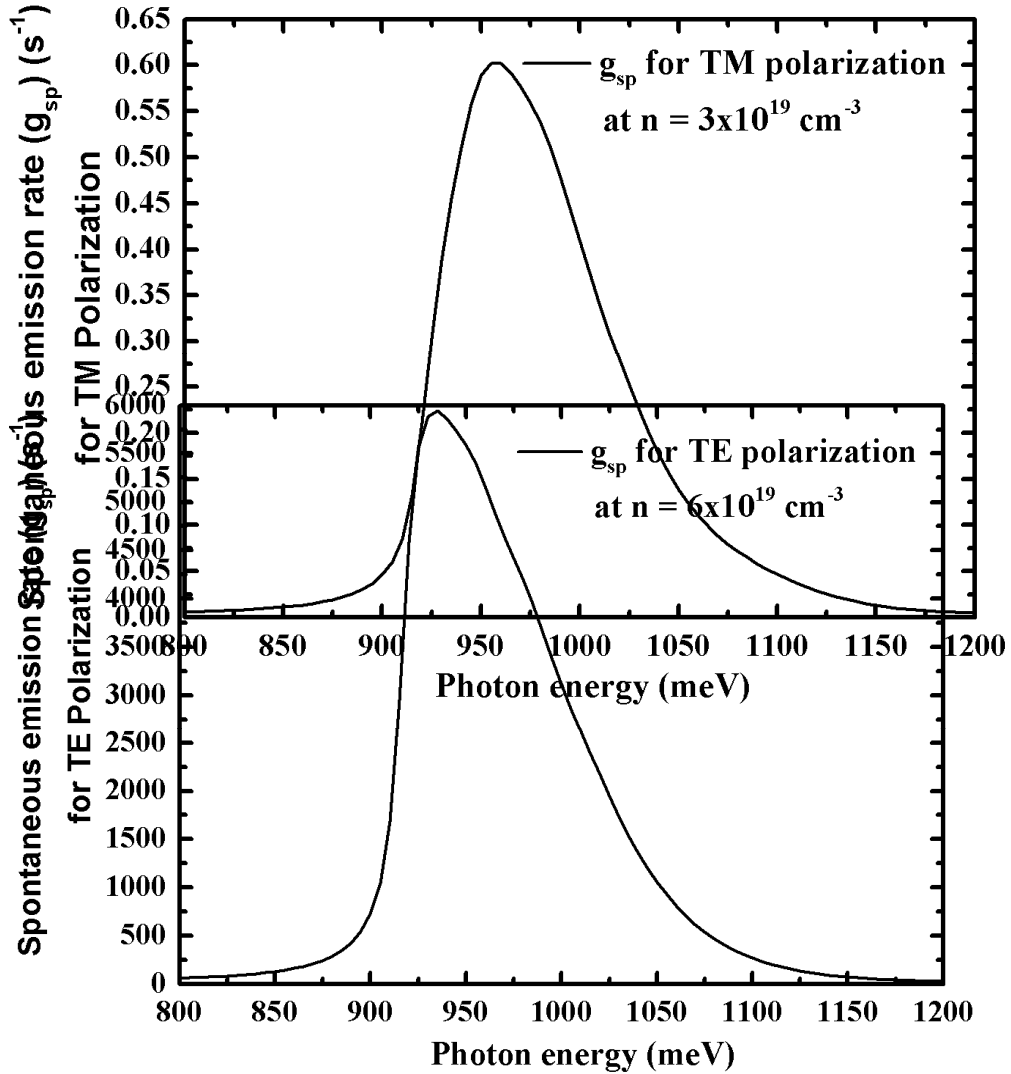
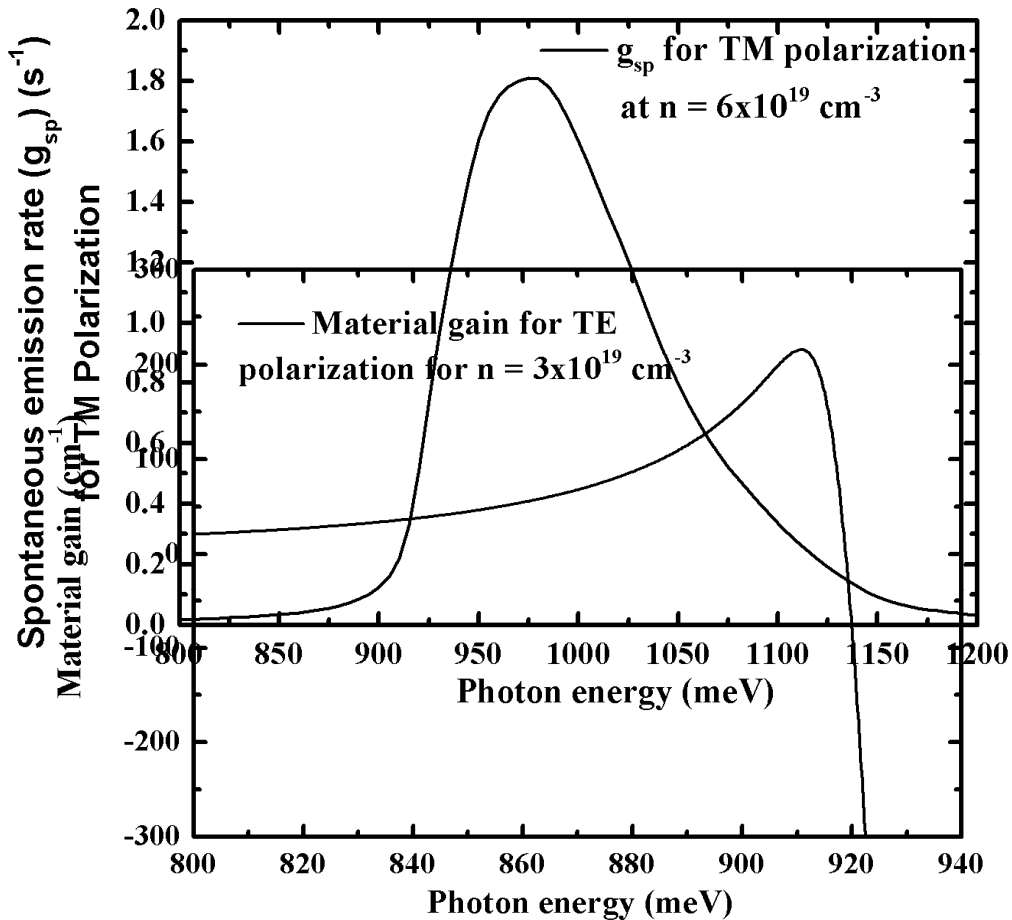


Figure 5.14: Spontaneous emission rate for TM polarization at $3 \times 10^{19} \text{ cm}^{-3}$ carrier density at $T=300 \text{ K}$.

Figure 5.15: Spontaneous emission rate for TM polarization at $6 \times 10^{19} \text{ cm}^{-3}$ carrier density at $T=300 \text{ K}$.

From the calculation of the spontaneous emission rate, we have calculated the material gain for the laser structure for both TE and TM polarization. Material gain or optical gain of a laser structure means the growth of the optical signal generated from the device per unit length. Optical gain of semiconductor laser is described as the optical amplification in the semiconductor materials. This gain term is associated with photon generation and recombination rate into the active region. If generation rate is higher than recombination rate, optical gain can be achieved from that structure. From the spontaneous emission, using the mirror emission has been trapped into the active region. And for the material gain the trapped optical signal strength has been increased and after certain level the signal can penetrate through the designed partially reflection mirror. Here these mirrors have been made by semiconductor materials following the Bragg reflection principle. Optical gain of a structure always denotes the gain after suppressing the loss terms of the structure. In Figure 5.16 and 5.17, optical gain for TE polarization of InN-InGaN laser structure with GaN layer at $3 \times 10^{19} \text{ cm}^{-3}$ and $6 \times 10^{19} \text{ cm}^{-3}$ carrier density has been depicted. Later in Figure 5.18 and 5.19, optical gain for TM polarization has been illustrated. From these figures, it is seen that TE polarization based optical gains are much higher than that of TM polarization as expected from valence subband structure. The HH and LH subbands contribute mostly to TE polarization.



Generally a narrow well has sharper gain and spontaneous emission spectrum than those of a wider well. Moreover narrow well width results large optical gain. Increase in well width decreases the magnitude of optical gain. The shape of optical gain spectrum shows good similarity with the same figure of [63, 64]. From Figure 5.16, it is found that the peak optical gain of 222.587 cm^{-1} for $3 \times 10^{19} \text{ cm}^{-3}$ carrier density at $T=300 \text{ K}$ has been occurred at 0.91 eV (at peak wavelength is 1366.1 nm). And from Figure 5.17, the peak optical gain of $5261.5187 \text{ cm}^{-1}$ for $6 \times 10^{19} \text{ cm}^{-3}$ carrier density at $T=300 \text{ K}$ has been found at 0.93 eV photon energy which means the peak emission wavelength of 1336.7 nm .

Figure 5.16: TE-polarized optical gain spectrum of 12\AA InN-InGaN quantum well with GaN layer for carrier density of $3 \times 10^{19} \text{ cm}^{-3}$ at $T = 300 \text{ K}$.

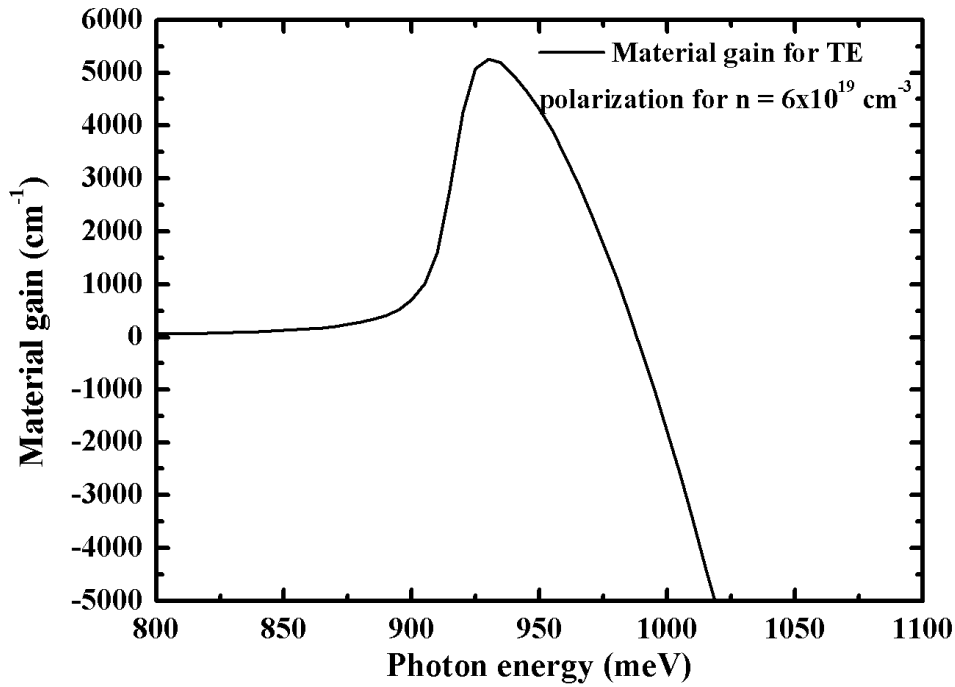


Figure 5.17: TE-polarized optical gain spectrum of 12\AA InN-InGaN quantum well with GaN layer for carrier density of $6 \times 10^{19} \text{ cm}^{-3}$ at $T = 300 \text{ K}$.

For TM polarized optical gain, the peak gain has been found as 0.0263 cm^{-1} and 1.2398 cm^{-1} for $3 \times 10^{19} \text{ cm}^{-3}$ and $6 \times 10^{19} \text{ cm}^{-3}$ carrier density respectively. Results are shown in Figure 5.18 and 5.19. From figures, it has been seen that the spectrum of TM polarized optical gain has flat shape in positive gain region and with the increase in photon energy it has shown a steep change in negative gain region which means in this region loss is greater than gain.

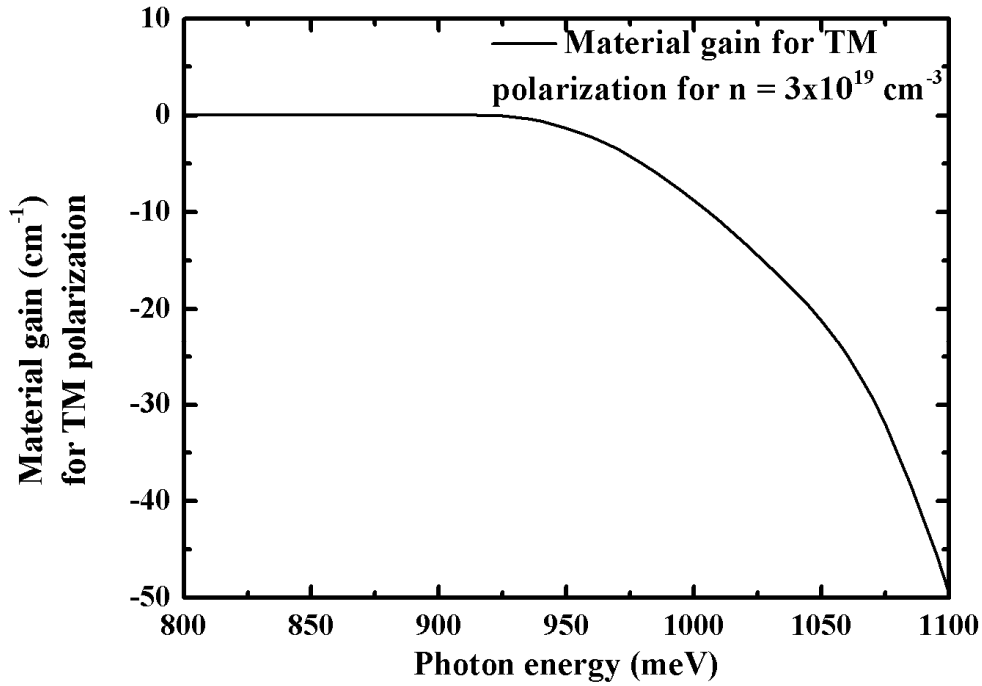


Figure 5.18: Optical gain spectrum of TM polarization for InN-InGaN QW structure with GaN layer for carrier density of $3 \times 10^{19} \text{ cm}^{-3}$ at $T = 300 \text{ K}$.

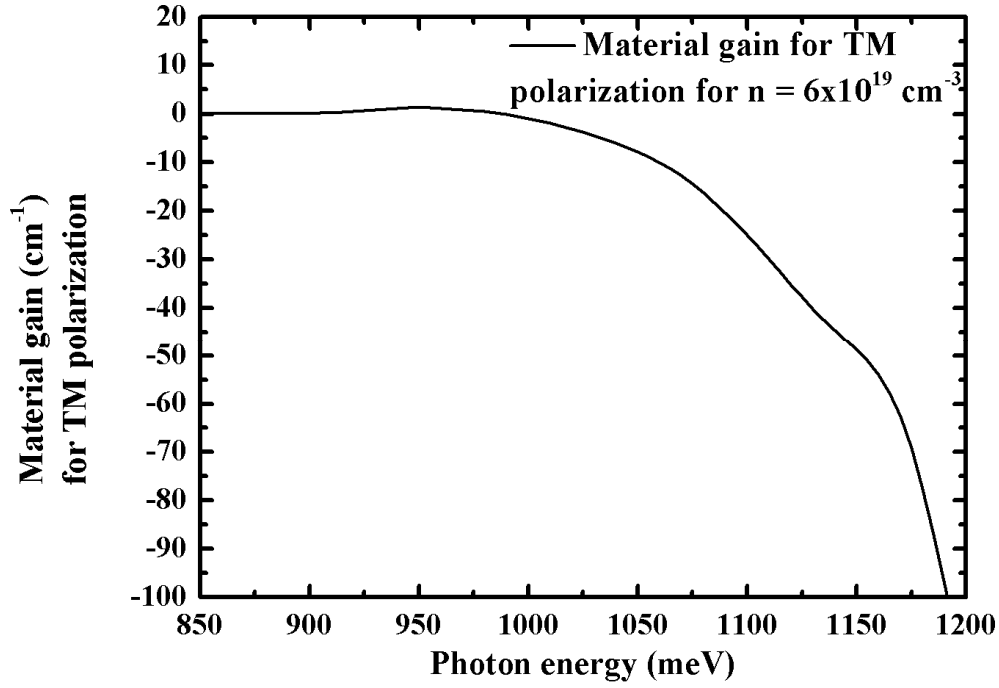


Figure 5.19: Optical gain spectrum of TM polarization for InN-InGaN QW structure with GaN layer for carrier density of $6 \times 10^{19} \text{ cm}^{-3}$ at $T = 300 \text{ K}$.

In Figure 5.20 and 5.21, optical gain of the Laser Structure for a range of carrier density from $2 \times 10^{19} \text{ cm}^{-3}$ to $6 \times 10^{19} \text{ cm}^{-3}$ has been shown. Figure shows that the peak optical gain increases with the increase of the injection carrier density and the peak wavelength shows a blue shift which agrees with the previously published works [63, 64].

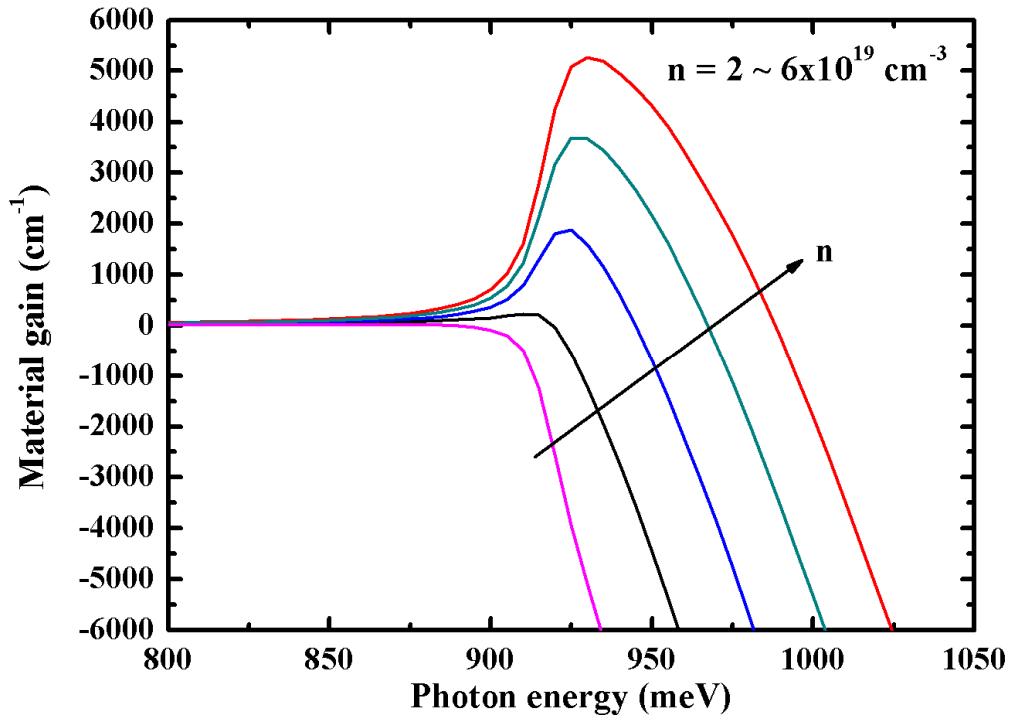


Figure 5.20: TE polarized optical gain spectra of strained 12Å InN-In_{0.25}Ga_{0.75}N quantum well with GaN layer for carrier density (n) from $2 \times 10^{19} \text{ cm}^{-3}$ up to $6 \times 10^{19} \text{ cm}^{-3}$ at T = 300 K.

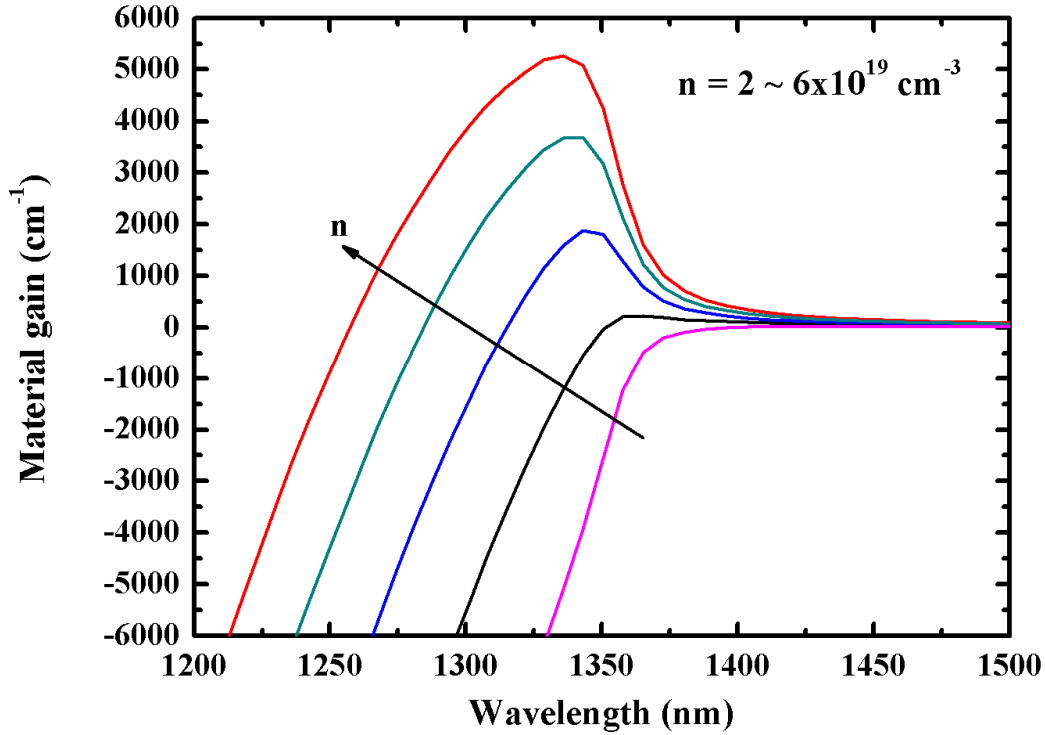


Figure 5.21: TE polarized optical gain spectra with respect to emission wavelength of strained 12Å InN-In_{0.25}Ga_{0.75}N quantum well with GaN layer for carrier density (n) from $2 \times 10^{19} \text{ cm}^{-3}$ up to $6 \times 10^{19} \text{ cm}^{-3}$ at T = 300 K.

From Figure 5.21, it has been found that the optical gain near threshold condition [$n_{th} \sim 2-3 \times 10^{19} \text{ cm}^{-3}$] has the emission wavelength of around 1350nm. Both figures also show that with the increase in the injection carrier density, the optical gain shows good improvement in magnitude which means that the designed structure will provide a good lasing output.

Following the equation (3.67) and (3.68), the spontaneous emission spectra for InN-In_{0.25}Ga_{0.75}N has been calculated for a range of carrier density of $2 \times 10^{19} \text{ cm}^{-3}$ up to $6 \times 10^{19} \text{ cm}^{-3}$ at T = 300 K using the simulation model. The spontaneous emission spectrum has important role in calculating the optical gain. As like the optical gain, narrow well results sharper spectrum in comparison with that of wider well. From the optical transition matrix element, the net optical emission of a structure has been obtained with random phase orientation known as spontaneous discussed in Chapter Two. But in lasing action, we need stimulated emission which can be found from spontaneous emission using feedback system (mirror system). As spontaneous emission has significant role in forming optical gain, both shows almost same behavior. In a Laser structure, when spontaneous emission has begun to build-up, due to loss components no lasing output has been found. That's why optical gain spectrum has negative component and within this spectrum region, Laser has no gain. In Figure 5.22, spontaneous emission spectrum of the designed structure for carrier density of

$3 \times 10^{19} \text{cm}^{-3}$ at $T = 300 \text{ K}$ has been given. Figure 5.23 shows spontaneous emission spectrum for carrier density of $6 \times 10^{19} \text{cm}^{-3}$ at same temperature. The peak emission rate has been found as $2.946 \times 10^{27} \text{ s}^{-1} \text{cm}^{-3} \text{eV}^{-1}$ at 0.93eV for carrier density of $3 \times 10^{19} \text{cm}^{-3}$ and $7.21 \times 10^{27} \text{ s}^{-1} \text{cm}^{-3} \text{eV}^{-1}$ at 0.935eV for $6 \times 10^{19} \text{cm}^{-3}$ carrier density. Comparing with [31, 63 and 64], the wave-shape of the spontaneous emission spectrum shows a similar behavior and good improved emission rate.

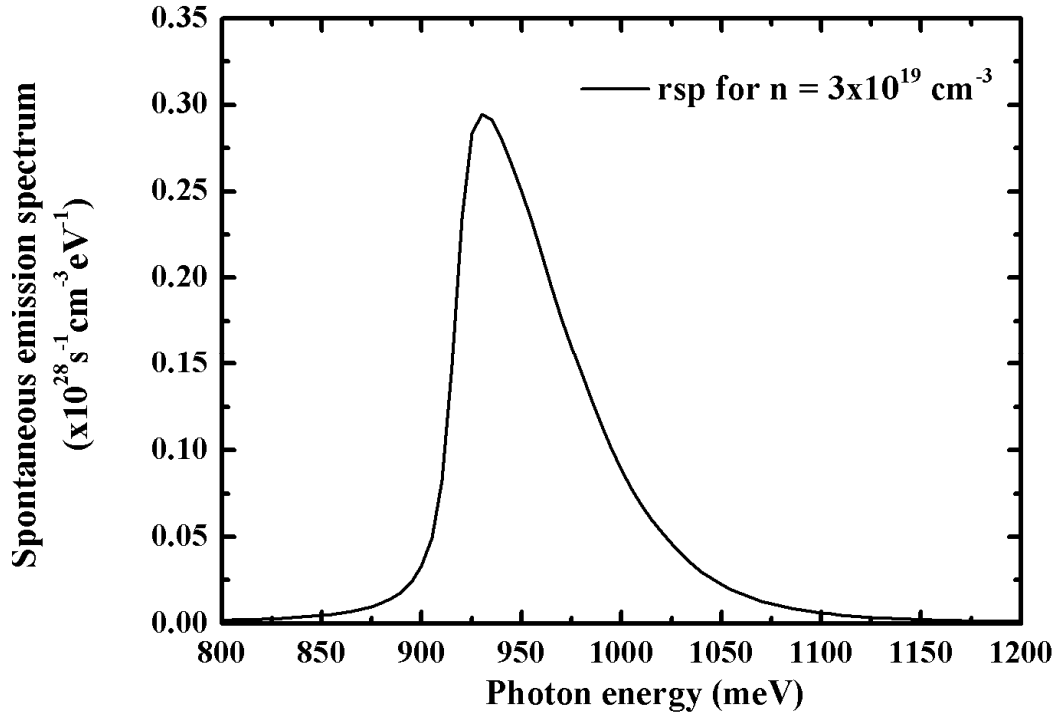


Figure 5.22: Spontaneous emission spectrum of 12Å InN-In_{0.25}Ga_{0.75}N quantum well with GaN layer for carrier density (n) from $3 \times 10^{19} \text{ cm}^{-3}$ at $T = 300 \text{ K}$.

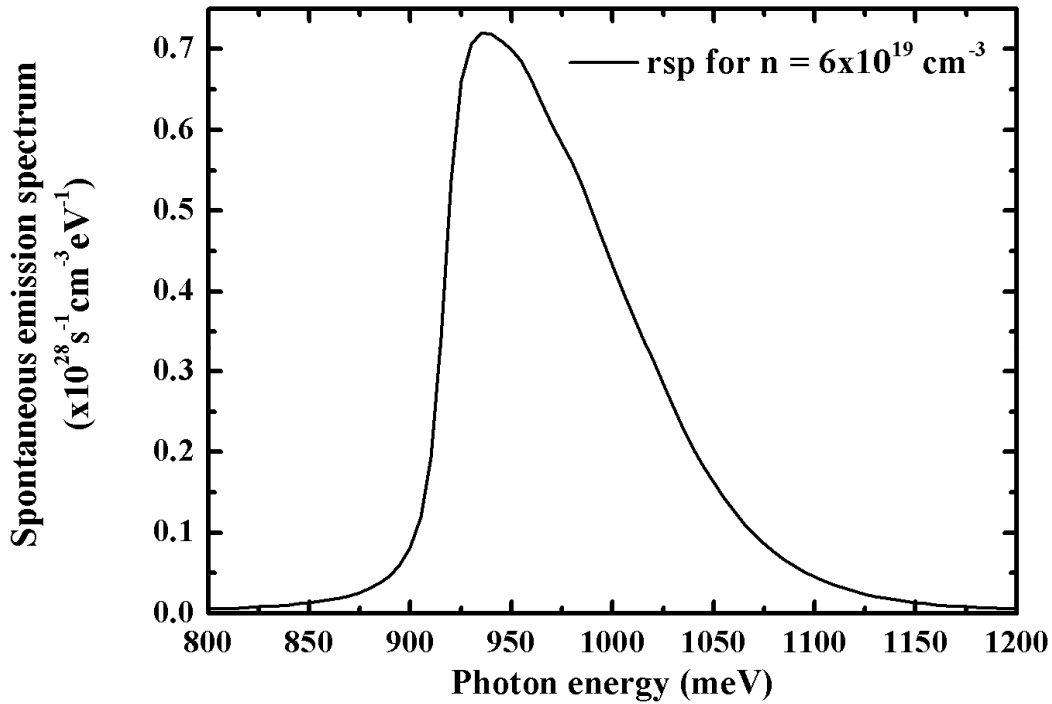
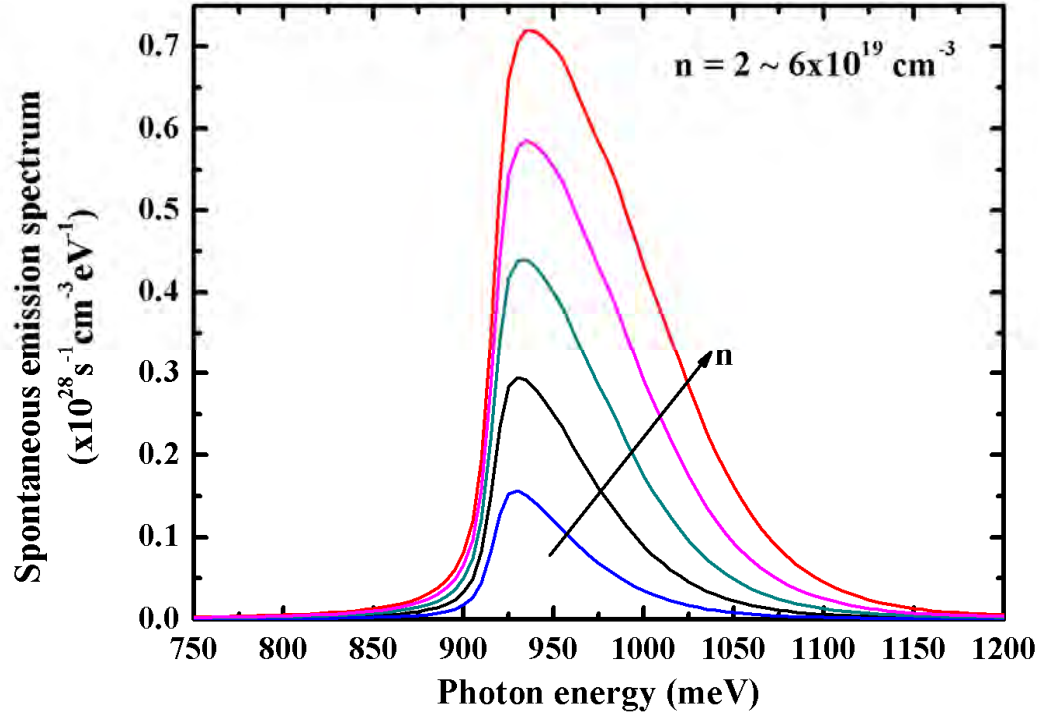


Figure 5.23: Spontaneous emission spectrum of 12Å InN-In_{0.25}Ga_{0.75}N quantum well with GaN layer for carrier density (n) from $6 \times 10^{19} \text{ cm}^{-3}$ at $T = 300 \text{ K}$.

In Figure 5.24 and 5.25, spontaneous emission spectra of the designed structure has been shown for a range of carrier density from $n = 2 \times 10^{19} \text{ cm}^{-3}$ to $6 \times 10^{19} \text{ cm}^{-3}$. From both figures, it is shown

that increase in carrier density increases the peak emission amplitude and the peak wavelength shows a slight blue-shift with the increase in carrier density. This spontaneous emission spectrum depends on the electron-hole wavefunction overlap factor. Higher overlap will cause higher spontaneous emission rate. Both Figure 5.24 and 5.25 shows good similarity and better improved



behavior in comparison with [31, 63 and 64].

Figure 5.24: Spontaneous emission spectra of strained 12Å InN-In_{0.25}Ga_{0.75}N quantum well with GaN layer for carrier density (n) form $2 \times 10^{19} \text{cm}^{-3}$ up to $6 \times 10^{19} \text{cm}^{-3}$ at $T = 300 \text{ K}$.

Figure 5.25: Spontaneous emission spectra with respect to emission wavelength of strained 12Å InN-In_{0.25}Ga_{0.75}N quantum well with GaN layer for carrier density (n) form $2 \times 10^{19} \text{cm}^{-3}$ up to $6 \times 10^{19} \text{cm}^{-3}$ at $T = 300 \text{ K}$.

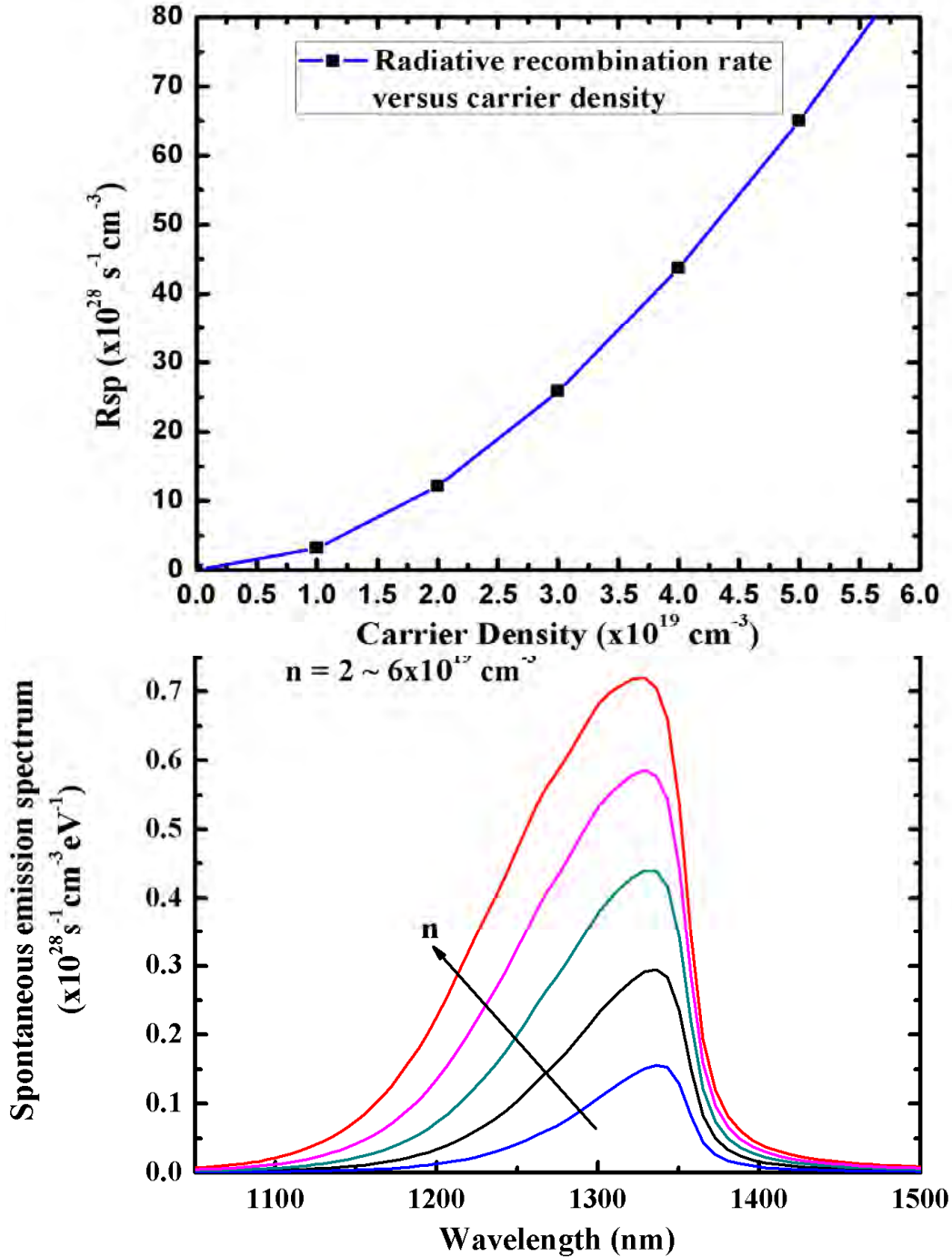
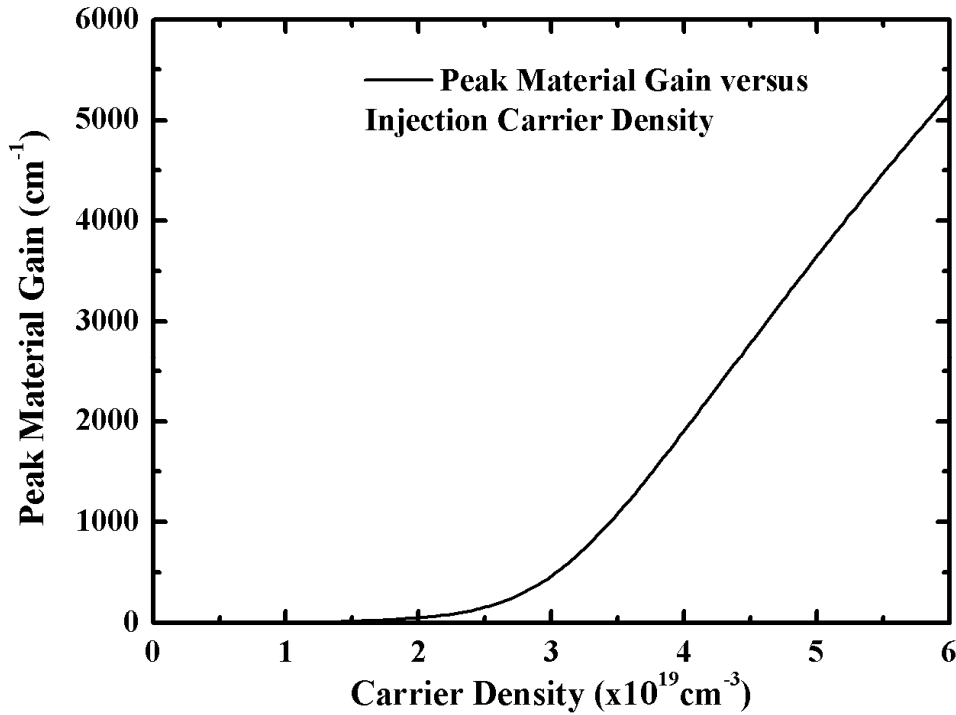


Figure 5.26: Spontaneous emission radiative recombination rate per unit volume as a function of carrier density at 300 K for 12Å InN-In_{0.25}Ga_{0.75}N quantum well.

Figure 5.26 illustrate the spontaneous emission radiation recombination rate per unit volume (R_{sp}) of 12Å InN-In_{0.25}Ga_{0.75}N quantum well structure plotted against carrier density (n) for low carrier

density ($n = 2 \times 10^{18} \text{ cm}^{-3}$ up to $10 \times 10^{18} \text{ cm}^{-3}$) and high carrier density ($n = 2 \times 10^{19} \text{ cm}^{-3}$ up to $6 \times 10^{19} \text{ cm}^{-3}$) regimes respectively. The spontaneous emission radiative recombination rate per unit volume can be obtained from equation (3.73) of Chapter Three. The typical carrier density for LED operation ranges from $2.5 \times 10^{18} \text{ cm}^{-3}$ up to $1 \times 10^{19} \text{ cm}^{-3}$ [79]. As shown in Figure 4.30, QW exhibited a significant enhancement of the radiative recombination rate for the low carrier density regime. This will lead to a significant improvement in the radiative efficiency of the LEDs. On the other hand, designed structure shows a significant improvement of the radiative recombination rate for the high carrier density regime where the threshold carrier density of QW structure exists. This enhancement indicates the application of the designed structure for laser operation with higher radiative efficiency.

Figure 5.27 shows the peak optical gain of the InN-InGaN quantum well with respect to carrier density from $1 \times 10^{19} \text{ cm}^{-3}$ up to $6 \times 10^{19} \text{ cm}^{-3}$. The transparency carrier densities (n_{tr}) for the designed



laser structure is around $\sim 0.5 \times 10^{19} \text{ cm}^{-3}$. Transparency carrier density gives the transparency current density which is defined as the minimum current density for which the material becomes transparent for any photon energy larger than or equal to the well band gap energy. The material becomes transparent when the gain equals to zero. Beyond the transparency carrier density, the material shows the gain phenomena which increases very fast with increase in carrier density. In our structure, the peak material gain has been found as 2.43 cm^{-1} at carrier density of $1 \times 10^{19} \text{ cm}^{-3}$ and gain increases up to 5261.518 cm^{-1} at carrier density of $6 \times 10^{19} \text{ cm}^{-3}$. Figure 5.27 shows a good agreement with [55, 63 and 78].

Figure 5.27: Peak material gain as a function of carrier density at 300 K for the designed laser structure.

From the Figure 5.27, the differential gain for the structure has been calculated. The gain coefficient of a thinner well has a larger transparent carrier density and larger differential gain than those of a wider well. Differential gain (dg/dn) denotes the increase in optical gain with the increase in injected carrier density. Generally differential gain is reduced as the optical gain increased. For our structure, the obtained differential gain is $1.871 \times 10^{-18} \text{ cm}^2$ at $2 \times 10^{19} \text{ cm}^{-3}$ carrier density. At $3 \times 10^{19} \text{ cm}^{-3}$ carrier density, the value of dg/dn is $2.014 \times 10^{-17} \text{ cm}^2$ when at $4 \times 10^{19} \text{ cm}^{-3}$ and higher carrier density, the value of dg/dn is around $1.7 \times 10^{-16} \text{ cm}^2$. Without considering carrier screening effect, the maximum differential gain is found near transparency condition. Higher differential gain should lead to higher modulation bandwidth as well as low frequency chirp and narrow linewidth capabilities. Modulation bandwidth can be derived from the modulation transfer function of the structure where the relationship between output laser power and the generated photon number due to the injected carrier density is made. And frequency chirp means the instantaneous frequency changing with time.

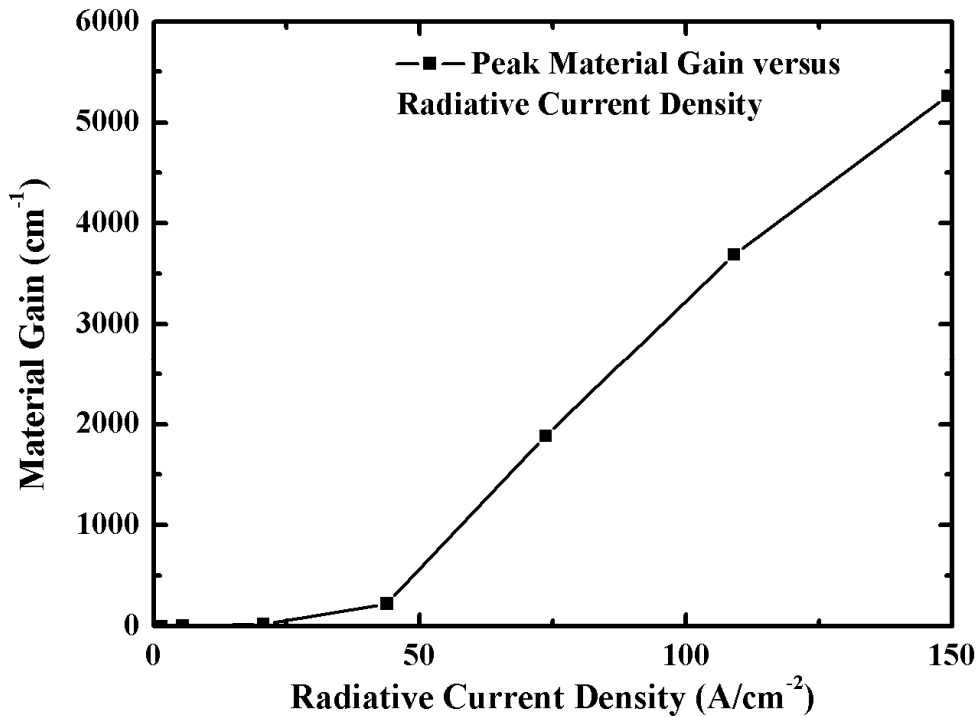
From the recombination of electron and hole, some amount of energy has been released. This energy may be of two kinds: radiative recombination and nonradiative recombination. Radiative recombination generates photon which can be spontaneous emission or stimulated emission. Stimulated emission provides the optical gain. When pumping rate increases, E_{FC} increases and E_{FV} decreases. At the condition of $E_{FC} - E_{FV} = E_g$, the material become transparent. But at $E_{FC} - E_{FV} > E_g$, the material can provide optical gain. And when from the recombination of electron and hole, energy is emitted as phonon, the recombination is known as nonradiative recombination. This parameter affects the threshold current density of a structure. This recombination includes Auger recombination, surface recombination and recombination due to defects. It is important that the reduction in the threshold carrier density or current density can be obtained from the minimization of the nonradiative recombination rate. From the equation (3.74), we can derived the radiative recombination current density for our designed structure from radiative spontaneous emission rate. In Figure 5.28, the relationship between calculated material gain and radiative recombination current density has been shown. Figure shows that with radiative current density of

above 30 Acm^{-2} the structure shows an increase in optical gain and with the increase in current density optical gain increases largely. Figure 5.28 shows the agreement with [63].

Figure 5.28: Material gain or optical gain versus radiative current density of InN-InGaN quantum well structure.

5.4 Optimization of the Laser Parameters

Up to now we have worked with fixed device structure's parameters for which we have gotten some fixed laser characterization parameters. From these parameters, we have calculated the electronic characteristics and then from the electronic characteristics we have performed the



optical characteristics. As we have the aim to design a QW laser structure, our material choice is fixed. And with this selection, material parameters are also became fixed. To modulate the laser's optical characteristics we have to depend on the device structure's parameters like well width, barrier width, SCH width, injected carrier density etc. As these parameters are user defined parameters. From the mathematical analysis of chapter 03, we have known that these parameters have certain effects on the electronic properties of the designed structure like the position of the conduction and valence subbands, interband momentum matrix elements etc. With the decrease in well width generally subband's position comes nearer the band edge of the corresponding band. Moreover, spontaneous emission rate and optical gain are also device structure parameter dependent. So with the modulation of the device structure's parameters, optical properties of a QW structure are also modulated. From this modulation, in our work we have tried to find out the optimum performance of the designed structure. For this performance we have utilized genetic algorithm based MATLAB tool. Chapter 03 gives an elaborate notion about the genetic algorithm's principles. In this work, for the optical characteristics optimization of quantum well

lasers at communication, multi-objective Genetic algorithm has been applied. This global search algorithm searches for the global optimum for a multi-variable multi-objective target problem. From a batch of initial population (i.e., probable solutions) the genetic algorithm repeatedly modifies the population of individual solutions at each step (or generation). Over successive generations, the population evolves toward optimal solutions.

In this work, the fitness function for the Genetic algorithm (GA) is defined as a vector consisting of the spontaneous emission rate and the optical gain for both TE and TM polarization. Minimization of the fitness function is done using the Genetic algorithm based Optimization toolbox of MATLAB. Therefore, negative values of the target functions are used for maximizing these parameters. For evaluating the fitness of the solutions the Pareto ranking technique is used. The implemented Genetic algorithm uses tournament type selection function with tournament size of 2 and adaptive feasible mutation function that generates adaptive directions depending on previous generations. The intermediate crossover function is used for reproduction with crossover fraction equal to 0.8 and crossover ratio equal to 1. After every 20 generations, forward migration is used with a migration fraction of 0.2. The initial populations are created randomly within the given boundary conditions. The results of the multi-objective Genetic algorithm contains a Pareto optimal set in which the solutions (known as the non-dominated Pareto optimal solutions) optimizes the objectives at an accepted level. Identifying the entire Pareto optimal set is practically unfeasible due to its size and computational limitations. Hence, certain boundaries or constraints are required to be imposed on the input vector. For this optimization problem, the input vector consists of the physical device parameters. Layer thicknesses are only allowed to have integer values in angstroms and kept within a reasonable boundary. From the performance of the GA based optimization process, we have two kinds of optimum results. First result is the maximum optical output that can be found from this material system. Second result is the maximum optical output that the designed structure can generate at around 1330 nm wavelength. After starting the optimization process, to obtain the optimum results 30 iterations required with 54 hour time duration. Two optimization processes are performed in this work. In the first performance, symmetric barrier and SCH width have been considered. From this performance, the optimum spontaneous emission rate of $8.376 \times 10^{27} \text{ s}^{-1} \text{ cm}^{-3} \text{ eV}^{-1}$ at 1308.6 nm wavelength and maximum TE polarized optical gain of 5957.6 cm^{-1} at 1322.3 nm wavelength are obtained for 12Å well width, 11Å barrier width, 58Å SCH width at $6 \times 10^{19} \text{ cm}^{-3}$ injected carrier density at $T = 300 \text{ K}$. In second optimization performance, asymmetric barrier and SCH width have been considered. From the performance, optimum spontaneous emission rate of $5.958 \times 10^{27} \text{ s}^{-1} \text{ cm}^{-3} \text{ eV}^{-1}$ at 0.835eV and maximum TE polarized optical gain of 5669 cm^{-1} at 0.83eV are obtained for 13Å well width, 13Å and 14Å barrier width, 32Å and 78Å SCH width and $6 \times 10^{19} \text{ cm}^{-3}$ injected carrier density at $T = 300 \text{ K}$.

Chapter Six

Conclusion and Future work

6.1 Conclusion of the Work

In this work, a wurtzite strained based nitride semiconductor quantum well (QW) laser has been designed and characterized. After the characterization, a genetic algorithm based optimization has been performed to obtain the optimum optical output signal. The underlying motivation of this work is to design a laser structure for communication wavelength. In our design, we focused on the design of a QW laser structure which can produce an optical output at around 1330 nm wavelength. We have taken the interband device structure for our design. All the performance has been done by utilizing our developed simulation model using MATLAB based on the discussion of chapter 03 for device characterizations. For the work, we first select a proper material system and corresponding layer thickness to obtain our desire output. Here, 12Å of InN layer has been taken as well region which is known as the active region. 15Å InGaN layer has been chosen as barrier region and 54Å GaN layer has been utilized as separate hetero-structure confinement (SCH) which provides better carrier and optical confinement to increase the recombination rate in the active region.

After the selection process, we have performed our developed simulation model to obtain the electronic characteristics of the designed structure. From this performance, we have conduction subbands, wave function for conduction subbands, valence subbands, wave function for valence subbands and interband transition matrix elements which is derived from Fermi's golden rule. Here, a self-consistent model has been developed for the performance of electronic properties. In this model separate Schrodinger's equations for both conduction and valence band along with Poisson's equation have been solved. For conduction band, a single band Hamiltonian has been formed when for valence band a 6-band k.p Hamiltonian formalism has been utilized. To calculate the band profile, valence band mixing, strained effect due to lattice mismatch, spontaneous polarization due to distortion of charge symmetry and piezoelectric polarization effect. All the material parameters are given in table in chapter four. From the performance of the electronic properties, we have found that our designed laser structure is of TE polarization type. In our designed QW structure, C1-HH1 and C1-LH1 transitions are most dominating transition for TE polarization while TM polarized momentum matrix elements have significantly lower value. The highest value of TE-polarization has found $0.2 \times 10^{-50} \text{ kg}^2\text{m}^2/\text{s}^2$ and for TM-polarization the highest value is $0.07 \times 10^{-50} \text{ kg}^2\text{m}^2/\text{s}^2$ at $k = 0$ position. All the performed results are plotted and demonstrated in chapter 04 with detailed discussion. All these results show good agreement with the previously published works.

After obtaining the electronic properties of the designed QW structure, we have performed another simulation model developed by us in MATLAB to obtain the optical properties. Using the obtained

interband momentum matrix elements, the optical properties of the designed laser structure has been determined. In our work, among the optical properties spontaneous emission rate for TE and TM polarization, spontaneous emission rate per unit energy interval per volume, material gain for TE and TM polarization, spontaneous emission radiative recombination rate and radiative recombination current density are calculated. The amount of the spontaneous emission rate depend on the electron and hole wave-function overlap integral. Higher overlap factor provides higher oscillator strength. For our device structure, we have gotten 43.27% of overlap integral. To analysis the optical properties of the QW laser structure, a range of injected carrier density from $2 \times 10^{18} \text{ cm}^{-3}$ to $6 \times 10^{19} \text{ cm}^{-3}$ has been used.

For carrier density of $3 \times 10^{19} \text{ cm}^{-3}$, the obtained peak spontaneous emission rate for TE polarization is 2456.024 s^{-1} at 0.93 eV (at 1336.7 nm wavelength) when peak emission rate for TM polarization is 0.60198 s^{-1} at 0.955 eV which is correspond to 1301.67 nm wavelength. The peak optical gain of 222.587 cm^{-1} for $3 \times 10^{19} \text{ cm}^{-3}$ carrier density at $T=300 \text{ K}$ has been calculated at 0.91 eV (peak wavelength is 1366.1 nm) and for TM polarized optical gain, the peak gain has been found as 0.0263 cm^{-1} . The peak spontaneous emission rate per energy interval per volume has been found as $2.946 \times 10^{27} \text{ s}^{-1} \text{ cm}^{-3} \text{ eV}^{-1}$ at 0.93 eV for carrier density of $3 \times 10^{19} \text{ cm}^{-3}$. On the other hand, the peak spontaneous emission rate for TE polarization has been measured as 5945.2 s^{-1} at 0.935 eV (at 1329.55 nm wavelength) and 1.8084 s^{-1} has been found at 0.975 eV (at 1275 nm wavelength) for TM polarization at carrier density of $6 \times 10^{19} \text{ cm}^{-3}$ at $T = 300 \text{ K}$. At same carrier density and temperature, the peak optical gain of $5261.5187 \text{ cm}^{-1}$ has been found at 0.93 eV photon energy which means the peak emission wavelength of 1336.7 nm. And the TM polarized peak optical gain has been obtained as 1.2398 cm^{-1} . The peak spontaneous emission rate per energy interval per volume has been determined as $7.21 \times 10^{27} \text{ s}^{-1} \text{ cm}^{-3} \text{ eV}^{-1}$ at 0.935 eV (1329.55 nm peak emission wavelength) for $6 \times 10^{19} \text{ cm}^{-3}$ carrier density.

From the sweeping of the carrier density, it is found that with the increase in carrier density the amplitude of spontaneous emission rate per unit energy interval per unit volume is also increased and the peak emission wavelength shows a slight blue-shift in wavelength. And optical gain analysis with carrier density sweeping, we have seen that the value of peak optical gain is increased with the increase in carrier density and the peak emission wavelength shows a blue shift. After these analysis, we have calculated the spontaneous emission radiative recombination rate for both carrier density range of LED operation ($n = 2 \times 10^{18} \text{ cm}^{-3}$ up to $10 \times 10^{18} \text{ cm}^{-3}$) and Laser operation ($n = 2 \times 10^{19} \text{ cm}^{-3}$ up to $6 \times 10^{19} \text{ cm}^{-3}$). From the analysis of peak optical gain versus carrier density, the obtained transparency carrier densities (n_{tr}) for the designed laser structure is relatively in the range of $\sim 0.5 \times 10^{19} \text{ cm}^{-3}$. For our structure, the obtained differential gain is $1.871 \times 10^{-18} \text{ cm}^2$ at $2 \times 10^{19} \text{ cm}^{-3}$ carrier density. At $3 \times 10^{19} \text{ cm}^{-3}$ carrier density, the value of dg/dn is $2.014 \times 10^{-17} \text{ cm}^2$ when at $4 \times 10^{19} \text{ cm}^{-3}$ and higher carrier density, the value of dg/dn is around $1.7 \times 10^{-16} \text{ cm}^2$. Relationship between peak optical gain versus radiative recombination current density has been also determined and demonstrated in chapter four.

After having all the electronic and optical properties, a multi-objective Genetic algorithm based optimization process has been adopted to determine the optimum performance parameters. From the performance of the GA based optimization process to obtain the optimum results 30 iterations required with 48 hour time duration. Two optimization processes are performed in this work. In the first performance, symmetric barrier and SCH width have been considered. From this performance, the optimum spontaneous emission rate of $8.376 \times 10^{27} \text{ s}^{-1} \text{ cm}^{-3} \text{ eV}^{-1}$ at 1308.6 nm wavelength and maximum TE polarized optical gain of 5957.6 cm^{-1} at 1322.3 nm wavelength are obtained for 12Å well width, 11Å barrier width, 58Å SCH width and $6 \times 10^{19} \text{ cm}^{-3}$ injected carrier density at $T = 300 \text{ K}$. In the second optimization performance, asymmetric barrier and SCH width have been considered. From this performance, the optimum spontaneous emission rate of $5.958 \times 10^{27} \text{ s}^{-1} \text{ cm}^{-3} \text{ eV}^{-1}$ at 0.835eV photon energy and maximum TE polarized optical gain of 5669 cm^{-1} at 0.83eV photon energy are obtained for 13Å well width, 13Å and 14Å barrier width, 32Å and 78Å SCH width at $6 \times 10^{19} \text{ cm}^{-3}$ injected carrier density at $T = 300 \text{ K}$.

Growth of high quality InN alloy have been reported for material grown by metal organic chemical vapor deposition (MOCVD) [80-81] and molecular beam epitaxy (MBE) [82-83]. The growths of InN material by MBE have resulted in high electron mobility in the order of $2370 \text{ cm}^2/\text{Vs}$. The use of pulsed MOCVD has also resulted in high optical quality InN alloy. Recent experimental studies by MBE have also indicated the capabilities to grow InN with monolayer precision.

6.2 Scope of Future Works

In this work, we try to develop a numerical simulation model to characterize the electronic and optical properties of a wurtzite-strained nitride semiconductor single quantum well laser (SQW). For the characterization, we have used 6 band ***k,p*** method for valence band and separate Hamiltonian for conduction band. This process of band calculation is perfect for one dimensional confinement like QW and many previously published works addressed this formalism mentioned in chapter 03. But still for higher dimensional confinement and incorporating the conduction band effect with valence band, 8 band ***k,p*** formalism provides better result. In our future extension, we will work on this 8 band ***k,p*** method which is appropriate to include eight functions in the set, namely the spin up and spin down zone center Bloch waves from the conduction band minimum, and the spin up and spin down functions from each of the three degenerate p-like states at the top of the valence band [84].

Again, in our work, we limited our work to SQW structure and such multi material system where only one SQW exists. In case of higher number of QW, if the wells are closer to each other, positions of subbands into the well regions depend on the subband of nearer well. The energy levels interact, with one being forced to higher energies and the other to lower energies. This is analogous to the formation of a pair of bonding and antibonding orbitals when two hydrogen atoms

are brought together to form a hydrogen molecule. That's why, to do work on multiple quantum well structure, the effect of nearer well's energy subband should be included. In future, we are trying to incorporate this effect into our energy band calculation which will extend our work to multiple quantum well (MQW) structure.

Moreover, our work is focused on TE and TM polarized device structure design. But recent researches are covered the non-polar device structure design and characterization. Energy efficiency improvement was inevitable for solid-state lighting technology. During a research process on efficiency improvement, it was found that the quantum-confined Stark effect (QCSE) had a negative impact on nitride-based optoelectronic devices shown in chapter 02. The basal plane (called the c plane) is an electrically polar plane; the electrical polarization originates from the lack of inversion symmetry along the c axis. When a quantum-well (QW) structure is fabricated on the c plane, spatially fixed charges appear on both sides (an equal amount but opposite in sign for the two sides) of the QW which separate electrons and holes toward different sides because of the QW by Coulomb force. This spatial separation of mobile charges is referred to as QCSE. As a consequence, electrons and holes do not readily recombine and the light-emission efficiency deteriorates.

Materials research interest then expanded to another technique, which is called non-polar orientations. To obtain such structure, two approaches are studied. One is to find a suitable material system sweeping its composition as well as device parameter which will show non-polar characteristics. In this aspect, the challenge is to calculate the wavelength and composition dependent refractive index calculation. This calculation needs more complex model computation which includes exciton effect, bounded and unbounded wave-function effects. So for this, we have to develop another simulation model which is our future aim to extent the boundary of our works.

Second approach to design a non-polar structure is to do work with such structure whose has different growth axis like m -axis and a -axis discussed in chapter 02. Because electrical polarization occurs along the c axis, QW structures fabricated on non-polar planes (the a and m planes are the major ones) will not experience QCSE. Emission efficiency can be improved compared to those fabricated on the c plane. For the conventional light-emitting semiconductor materials, such as GaAs and InP, QCSE was not a serious problem. These materials crystallize into a zinc-blend structure (two-constituent cubic). The cubic structure has a higher crystal symmetry than the hexagonal structure, and conventional cubic materials do not experience QCSE under normal circumstances. When nitride films are prepared on non-polar planes, in-plane crystal symmetry (rectangular symmetry) becomes lower than for the films prepared on the c plane (hexagonal symmetry). As a result, light emission from these non-polar films can have polarized (asymmetric) characteristics to the surface-normal direction. For this types of structure, we have to reform our Schrodinger's equation with different kind of Hamiltonian formalism. Most of the recent works

are on this approach. In future, we have an aim to incorporate this approach into our research work to keep pace with the recent trends.

All of the above improvements are regarding to the electronic properties. In our work, we have a target to extend our optical analysis of our designed structure. In this work, we have only determined the QW's optical properties up to radiative recombination rate and current density. But into a QW system, there are some non-radiative recombination process which generates heat as a form of phonon. Auger recombination, surface recombination, recombination into crystal defects and leakage current are the non-radiative components which increase the threshold current for a QW structure. To analysis the threshold current density we have to determine the non-radiative current components. These components are some parameters dependent which are not well addressed. We have the aim to incorporate this non-radiative analysis into our optical properties determination techniques. Moreover, after characterizing and determining the electronic and optical parameters for active and modal region of the QW structure other important analyses are rate equation calculation, optical output power versus injection current, modulation bandwidth calculation are important for optoelectronics device characterization. For these analysis, we have to design two end facets or mirror at two ends of the QW structure which is made of semiconductor materials to provide the desired reflectivity. The design of this Bragg reflector needs some calculation. With the value of the reflectivity of the two mirrors, loss components are calculated and final optical output power is measured. The rate equations determines the rate at which an interactive process occurs and concentrating on the dominant features which limit the interaction rate. In semiconductor physics, the motion of the charge carrier as well as photon within a semiconductor is governed by a number of rate equations which determines the rate of change of particles in space, time momentum and energy. The laser diode rate equations model the electrical and optical performance of a laser diode. With these all improvements, a complete laser simulation model can be developed for any wurtzite-strained nitride semiconductor based multiple quantum well optoelectronic devices specially LEDs and lasers.

References

- [1] J. Hecht, "The Laser Guidebook," McGraw-Hill Companies, Inc., New York, 1993, pp. 1-3, 13-21, 23-42, 297-319, 355-370.
- [2] V. K. Kononenko, "History and Development of Semiconductor Lasers", 5th International Conference on Advanced Optoelectronics and Lasers (CAOL'2010), Sevastopol, Crimea, Ukraine, September 10 -14, 2010,
- [3] P. S. Zory Jr., "Quantum Well Lasers," Academic Press Limited, London, 1993, pp. 1-10, 18-92, 132-179, 217-263.
- [4] R. N. Hall, G. E. Fenner, J. D. Kingsley, T. J. Soltys and R. O. Carlson, "Coherent Light Emission from GaAs Junctions," Physical Review Letters, vol. 9, no. 9, pp. 366-368, November 1962.
- [5] M. I. Nathan, W. P. Dumke, G. Burns, F. H. Dill Jr. and G. Lasher, "Stimulated Emission of Radiation from GaAs p-n Junctions," Applied Physics Letters, vol. 1, no. 3, pp. 62-64, November 1962.
- [6] T. M. Quist, R. H. Rediker, R. J. Keyes, W. E. Krag, B. Lax, A. L. McWhorter and H. J. Zeigler, "Semiconductor MASER of GaAs," Applied Physics Letters, vol. 1, no. 4, pp. 91-92, December 1962.
- [7] N. Holonyak and S. F. Bevacqua, "Coherent (Visible) Light Emission From $\text{Ga}(\text{As}_{1-x}\text{P}_x)$ Junctions," Applied Physics Letters, vol. 1, no. 4, pp. 82-83, December 1962.
- [8] N. G. Basov, O. V. Bogdankevich and A. G. Devyatkov, "Exciting of a Semiconductor Quantum Generator with a fast electron beam," Soviet Physics - Doklady, vol. 9, pp. 288, February, 1964.
- [9] Zh. I. Alferov and R. F. Kazarinov, Russian patent application N950840 "Semiconductor Laser with Electrical Pumping" March 30, 1963.
- [10] H. Kroemer, "A proposed class of Hetero-junction injection lasers," Proceedings of the IEEE, vol. 51, no. 12, pp. 1782-1783, December 1963.
- [11] H. Rupprecht, J. M. Woodall and G. D. Pettit, "Efficient Visible Electroluminescence at 300° K from $\text{Ga}_{1-x}\text{Al}_x\text{As}$ p-n Junctions Grown by Liquid Phase Epitaxy," Applied Physics Letters, vol. 11, no. 3, pp. 81-83, August 1967.
- [12] Zh. I. Alferov, V. M. Andreev, D. Z. Garbuzov, Yu. V. Zhilyaev, E. P. Morozov, E. L. Portnoi and V. G. Trofim, "Investigation of the influence of the AlAs-GaAs heterostructure parameters on the laser threshold current and the realization of the continuous emission at room temperature," Soviet Physics Semiconductor, vol. 4, no. 9, pp. 1573–1575, 1971.

- [13] I. Hayashi, M. B. Panish, P. W. Foy and S. Sumski, "Junction lasers which operate continuously at room temperature," *Applied Physics Letters*, vol. 17, no. 3, pp. 109–111, August 1970.
- [14] L. Esaki and R. Tsu, "Superlattice and negative differential conductivity in semiconductors," *IBM Journal of Research and Development*, vol. 14, no. 1, pp. 61-65, January 1970.
- [15] R. F. Kazarinov and R. A. Suris, "Possibility of amplification of electromagnetic waves in a semiconductor with a superlattice," *Soviet Physics Semiconductor*, vol. 5, no. 4, pp. 707-709, October 1971.
- [16] N. Holonyak Jr., R. M. Kolbas, R. D. Dupuis and P. D. Dapkus, "Room-temperature continuous operation of photopumped MO-CVD $\text{Al}_x\text{Ga}_{1-x}\text{As-GaAs-Al}_x\text{Ga}_{1-x}\text{As}$ quantum-well lasers," *Applied Physics Letters*, vol. 33, no. 1, pp. 73-75, July 1978.
- [17] Joachim Piprek, "Nitride Semiconductor Devices: Principles and Simulation," Wiley-VCH Verlag GmbH & Co. KGaA, Weinheim, 2007.
- [18] H. Soda, K. Iga, C. Kitahara and Y. Suematsu, "GaInAsP/InP Surface Emitting Injection Lasers," *Japanese Journal of Applied Physics*, vol. 18, no. 12, pp. 2329-2330, December 1979.
- [19] J. Faist, F. Capasso, D. L. Sivco, C. Sirtori, A. L. Hutchinson, and A. Y. Cho, "Quantum Cascade Laser," *Science*, vol. 264, no. 5158, pp. 553-556, April 1994.
- [20] S. Nakamura, T. Mukai and M. Senoh, "Candela-class high-brightness InGaN/AlGaIn double-heterostructure blue-light-emitting diodes," *Applied Physics Letters*, vol. 64, no. 13, pp. 1687-1689, March 1994.
- [21] T. Suhara, "Semiconductor Laser Fundamentals", MerceL Dekker Inc., New York, 2004, pp. 1-14, 37-73, 79-97.
- [22] S. Nakamura, M. Senoh, S. Nagahama, N. Iwasa, T. Yamada, T. Matsushita, H. Kiyoku and Y. Sugimoto, "InGaIn-Based Multi-Quantum-Well-Structure Laser Diodes," *Japanese Journal of Applied Physics*, vol. 35 part 2, no. 1B, pp. L74-L76, January 1996.
- [23] I. Vurgftman and J. R. Meyer, "Band Parameters for Nitride-Containing Semiconductors," *Journal of Applied Physics*, vol. 94, no. 6, pp. 3675-3696, September 2003.
- [24] D. F. Feezell, M. C. Schmidt, R. M. Farrell, K.C. Kim, M. Saito, K. Fujito, D. A. Cohen, J. S. Speck, S. P. DenBaars and S. Nakamura, "AlGaIn-Cladding-Free Nonpolar InGaIn / GaIn Laser Diodes," *Japan Journal Applied Physics Letters*, vol. 46, part 2, no. 12-16, pp. L284-L286, April 2007.

- [25] U. K. Mishra, P. Parikh and Y. F. Wu, "AlGaIn/GaN HEMTs - an Overview of Device Operation and Application," *Proceedings of IEEE*, vol. 90, no. 6, pp. 1022-1031, June 2002.
- [26] J. Zhang, H. Tong, G. Y. Liu, J. A. Herbsommer, G. S. Huang and N. Tansu, "Characterizations of Seebeck Co-efficients and Thermoelectric Figures of Merit for AlInN Alloys with Various In-contents," *Journal of Applied Physics*, vol. 109, no. 5, pp. 053706, March 2011.
- [27] M. Jamil, H. Zhao, J. B. Higgins and N. Tansu, "MOVPE and Photoluminescence of Narrow Band gap (0.77 eV) InN on GaN/Sapphire by Pulsed Growth Mode," *Physics Status Solidi A*, vol. 205, no. 12, pp. 2886-2891, December 2008.
- [28] G. Sun, G. Xu, Y.J. Lin, H. Zhao, G. Liu, J. Zhang and N. Tansu, "Efficient Terahertz Generation from Multiple InGaIn/GaN Quantum Wells," *IEEE Journal of Selected Topic on Quantum Electron*, vol. 17, no. 1, pp. 48-53, January/February 2011.
- [29] M. A. Khan, Q. Chen, M. S. Shur, B. T. McDermott, J. A. Higgins, J. Burm, W. J. Schaff and L. F. Eastman, "Microwave Operation of GaN/AlGaIn-doped Channel Heterostructure Field Effect Transistors," *IEEE Electron Device Letter*, vol. 17, no. 7, pp. 325-327, July 1996.
- [30] H. Machhadani, P. Kandaswamy, S. Sakr, A. Vardi, A. Wirtmuller, L. Nevou, F. Guillot, G. Pozzovivo, M. Tchemycheva, A. Lupu, L. Vivien, P. Crozat, E. Warde, C. Bougerol, S. Schacham, G. Strasser, G. Bahir, E. Monroy and F. H. Julien, "GaN/AlGaIn Intersubband Optoelectronic Devices," *New Journal of Physics*, vol. 11 (120523), pp. 1-16, December 2009.
- [31] H. Zhao, G. Liu and N. Tansu, "Analysis of InGaIn-delta-InN Quantum Wells for Light-emitting Diodes," *Applied Physics Letter*, vol. 97, no. 13, pp. 131114, September 2010.
- [32] C. Galeriu, "k.p theory of Semiconductor Nanostructures," Ph. D. dissertation, Department of Physics, Worcester Polytechnic Institute, Worcester, Massachusetts, November 2005.
- [33] S. L. Chuang and C. S. Chang, "k.p method for strained wurtzite semiconductor," *Physical Review B*, vol. 54, no. 4, p. 2491-2504, July 1996.
- [34] J. McCall, "Genetic Algorithms for Modeling and Optimization," *Journal of Computational and Applied Mathematics*, vol. 184, no. 1, pp. 205-222, December 2005.
- [35] C. E. Webb and J. D C Jones, "Handbook of laser technology and applications," Institute of Physics Publishing, London, 2004, pp. 6-15.
- [36] P. W. Miloni and J. H. Eberly, "Laser Physics", John Wiley & Sons, New Jersey, 2010, pp. 1-12, 74-84, 141-170, 175-203.
- [37] S. O. Kasap, "Optoelectronics and Photonics: Principles and Practices", Prentice Hall, New Jersey, 2001, pp. 107-205.

- [38] S. Adachi, "Properties of Semiconductor Alloys Group-IV, III-V, II-VI Semiconductor", John Wiley & Sons, New York, 2009, pp. 133-214, 238-253, 277-286, 307-332.
- [39] T. Swietlik, "Laser Diodes based on Gallium Nitride - Investigation of Carrier Injection Mechanisms, Gain and Distribution of The Electromagnetic Field," Ph.D. Dissertation, Institute of High Pressure Physics, Polish Academy of Sciences, Warsaw 2008.
- [40] S. Nakamura and G. Fasol, "The Blue Laser Diodes: GaN Based Light Emitters and Lasers," Springer Verlag, Berlin 1997.
- [41] T. K. Sharma and E. Towe, "Application-oriented nitride substrates: The key to long-wavelength nitride lasers beyond 500 nm," Journal of Applied Physics, vol. 107, no. 2, pp. 024516(1-11), January 2010.
- [42] G. Muziol, H. Turski, M. Siekacz, M. Sawicka, P. Wolny, P. Perlin and C. Skierbiszewski, "Determination of gain in AlGaIn cladding free nitride laser diodes," Applied Physics Letters, vol. 103, no. 6, pp. 061102(1-3), August 2013.
- [43] F. Renner, P. Kiesel, G. H. Döhler, M. Kneissl, C. G. Van de Walle and N. M. Johnson, "Quantitative analysis of the polarization fields and absorption changes in InGaIn/GaN quantum wells with electroabsorption spectroscopy," Applied Physics Letters, vol. 81, no. 3, pp. 490-492, July 2002.
- [44] D. Fuhrmann, U. Rossow, C. Netzel, H. Bremers, G. Ade, P. Hinze and A. Hangleiter, "Optimizing the internal quantum efficiency of GaInN SQW structures for green light emitters," Physica Status Solidi C, vol. 3, No. 6, pp. 1966–1969, May 2006.
- [45] G. Franssen, a_ T. Suski, P. Perlin, R. Bohdan, A. Bercha, W. Trzeciakowski, I. Makarowa, P. Prystawko, M. Leszczyński, I. Grzegory and S. Porowski, "Fully-screened polarization-induced electric fields in blue/violet InGaIn/GaN light-emitting devices grown on bulk GaN," Applied Physics Letters, vol. 87, no. 4, pp. 041109(1-3), July 2005.
- [46] S. Nagahama, Y. Sugimoto, T. Kozaki and T. Mukai, "Recent progress of AlInGaIn laser diodes," Proceedings of SPIE, vol. 5738, pp. 57-62, 2005.
- [47] M. Ueda, K. Kojima, M. Funato, Y. Kawakami, Y. Narukawa and T. Mukai, "Epitaxial growth and optical properties of semipolar (11 $\bar{2}$ 2) GaN and InGaIn/GaN quantum wells on GaN bulk substrates," Applied Physics Letters, vol. 89, no. 21, pp. 211907(1-3), November 2006.
- [48] P. Waltereit, O. Brandt, A. Trampert, H. T. Grahn, J. Menniger, M. Ramsteiner, M. Reiche and K. H. Ploog, "Nitride semiconductors free of electrostatic fields for efficient white light-emitting diodes," Nature, vol. 406, no. 6798, pp. 865-868, August 2000.
- [49] B. A. Haskell, F. Wu, S. Matsuda, M. D. Craven, P. T. Fini, S. P. DenBaars, J. S. Speck and Shuji Nakamura, "Structural and morphological characteristics of planar (1120) a-plane gallium nitride grown by hydride vapor phase epitaxy," Applied Physics Letters, vol. 83, no. 8, pp. 1554-1556, August 2003.

- [50] P. Harrison, "Quantum Wells, Wires and Dots," Wiley, New York, 1999.
- [51] L. C. Lew Yan Voon and M. Willatzen, "Electron states in modulated nanowires," *Journal of Applied Physics*, vol. 93, no. 12, pp. 9997-10000, 2003.
- [52] N. W. Ashcroft and N. D. Mermin, "Solid State Physics," Brooks Cole, Cengage Learning, 1976.
- [53] C. Kittel, "Introduction to Solid State Physics," John Wiley & Sons, New York, 1953.
- [54] Y. Sun, S. E. Thompson and T. Nishida, "Strain Effect in Semiconductors: Theory and Device Applications," Springer, New York, 2010.
- [55] S. L. Chuang, "Optical Gain of Strained Wurtzite GaN Quantum Well Lasers," *IEEE Journal of Quantum Electronics*, vol. 32, no. 10, pp. 1791-1800, October 1996.
- [56] E. Vanelle, A Alexandrou, J.P. Likforman, D. Block, J. Cibert and R Romestain, "Ultrafast in-well screening of the piezoelectric field in (111) quantum wells," *Physical Review B*, vol. 53, no. 24, pp. R16172-R16175, June 1996.
- [57] S. H. Park and S. L. Chuang, "Crystal-orientation effects on the piezoelectric field and electronic properties of strained wurtzite semiconductors," *Physical Review B*, Vol. 59, No. 7, pp. 4725-4737, February 1999.
- [58] S. H. Park and S. L. Chuang, "Piezoelectric effects on electrical and optical properties of wurtzite GaN/AlGaIn quantum well lasers," *Applied Physics Letters*, vol. 72, no. 24, pp. 3103-3105, June 1998.
- [59] F. Bernardini and V. Fiorentini "Spontaneous vs. Piezoelectric Polarization in III-V Nitrides: Conceptual Aspects and Practical Consequences," *Physica Status solidi (b)*, vol. 216, pp. 391-398, November 1999.
- [60] F. Sacconi, A. D. Carlo, P. Lugli and H. Morkoc, "Spontaneous and piezoelectric polarization effects on the output characteristics of AlGaIn/GaN heterojunction modulation doped FETs," *IEEE Transactions on Electron Device*, vol. 48, no. 3, pp. 450-457, March 2001.
- [61] B. W. Kim, "Piezoelectric-field effect on electronic and optical properties of [111] $\text{In}_x\text{Ga}_{1-x}\text{As}$ / GaAs superlattices" *Journal of Applied Physics*, vol. 89, no. 2, pp. 1197-1204, January 2001.
- [62] W. Colin and J. Debdeep, "Polarization Effects in Semiconductors: From Ab Initio to Device Applications," Springer Science & Business Media, New York, 2007.
- [63] H. Zhao, R. A. Arif, Y. K. Ee and N. Tansu, "Self-Consistent Analysis of Strain-Compensated InGaIn-AlGaIn Quantum Wells for Lasers and Light-Emitting Diodes," *IEEE Journal of Quantum Electronics*, vol. 45, no. 1, pp. 66-78, January 2009.
- [64] H. Zhao, R. A. Arif, Y. K. Ee and N. Tansu, "Optical gain and spontaneous emission of strain-compensated InGaIn-AlGaIn quantum wells including carrier screening effect," *Proceedings of*

SPIE Photonics West 2008, Physics and Simulation of Optoelectronics Devices XVI, San Jose, CA, vol. 6889, p. 688903 (1-10), Jan. 2008.

[65] M. Suzuki, T. Uenoyama and A. Yanase, "First-principles calculations of effective-mass parameters of AlN and GaN," *Physical Review B*, vol. 52, no. 11, pp. 8132-8139, September 1995.

[66] C. S. Chuang, S. L. Chuang, J. R. Minch, W. C. W. Fang, Y. K. Chen and T. Tanbun-Ek, "Amplified spontaneous emission spectroscopy in strained quantum-well lasers," *IEEE Journal of Selected Topics in Quantum Electronics*, vol. 1, no. 4, pp. 1100-1107, December 1995.

[67] W. W. Chow and M. Kneissl, "Laser gain properties of AlGaIn quantum wells," *Journal of Applied Physics*, vol. 98, no. 11, pp. 114502(1-6), December 2005.

[68] S. Kirkpatrick, C. D. Gelatt, and M. P. Vecchi, "Optimization by simulated annealing," *Science*, vol. 220, no. 4598, pp. 671-680, May 1983.

[69] D. E. Goldberg, "Genetic Algorithms in Search, Optimization, and Machine Learning," Addison-Wesley, New York, 1989.

[70] P. A. Moscato, "On Evolution, Search, Optimization, Genetic Algorithms and Martial Arts. Towards Memetic Algorithms," Tech. Rep. Caltech Concurrent Computation Program, Report 826, California Institute of Technology, Pasadena, 1989.

[71] J. Kennedy and R. C. Eberhart, "Particle swarm optimization," *Proceedings IEEE International Conference on Neural Network*, Perth, Australia, vol. 4, pp. 1942-1948, December 1995.

[72] M. Dorigo, V. Maniezzo, and A. Colnari, "The ant system: Optimization by a colony of cooperating agents," *IEEE Transactions on Systems, Man, Cybernetics: Systems*, vol. 26, no. 1, pp. 29-41, February 1996.

[73] S. Gerbex, R. Cherkaoui, and A.J. Germond, "Optimal Location of Multitype FACTS Devices in a Power System by Means of Genetic Algorithms", *IEEE Transactions on Power Systems*, vol. 16, no. 3, pp. 537-544, August 2001.

[74] J. McCall, "Genetic algorithms for modelling and optimization," *Journal of Computational and Applied Mathematics*, vol. 184, pp. 205-222, 2005.

[75] K. Chandrasekar and N. V. Ramana, "Performance Comparison of GA, DE, PSO and SA Approaches in Enhancement of Total Transfer Capability using FACTS Devices," *Journal of Electrical Engineering & Technology*, vol. 7, no. 4, pp. 493-500, 2012.

[76] G. Shmavonyan and H. G. Asatryan, "The role of separate confinement heterostructure layer in designing semiconductor nanostructured optoelectronic devices," *Proceedings of SPIE, 16th International Workshop on Physics of Semiconductor Devices*, vol. 8549, October 2012.

- [77] C. F. Lin, Y. S. Su, C. H. Wu and Y. C. Chang, "Influence of Separate Confinement Heterostructure Layer on Carrier Distribution in InGaAsP Laser Diodes with Non-identical Multiple Quantum Wells," Japanese Journal of Applied Physics, vol. 43, no. 10, pp. 7032–7035, October 2004.
- [78] J. Zhang, H. Zhao and N. Tansu, "Large Optical Gain AlGaIn-delta-GaN Quantum Wells Laser Active Regions in Mid- and Deep-Ultraviolet Spectral Regimes," Applied physics letters, vol. 91, Art. 171111, April 2011.
- [79] Y. C. Shen, G. O. Mueller, S. Watanabe, N. F. Gardner, A. Munkholm and M. R. Krames, "Auger recombination in InGaIn measured by photoluminescence," Applied physics letters, vol. 91, Art. 141101, October 2007.
- [80] A. Kadir, T. Ganguli, M. R. Gokhale, A. P. Shah, S. S. Chandvankar, B. M. Arora and A. Bhattacharya, "Growth and characterization of InN layers by metal-organic vapour phase epitaxy in a close-coupled showerhead reactor," Journal of Crystal Growth, vol. 298, pp. 403-408, January 2007.
- [81] G. Xu, Y. J. Ding, H. P. Zhao, M. Jamil, G. Y. Liu, N. Tansu, I. B. Zotova, C. E. Stutz, D. E. Diggs, N. Fernellius, F. K. Hopkins, C. S. Gallinat, G. Koblmüller and J. S. Speck, "THz generation from InN films due to destructive interference between optical rectification and photocurrent surge," Semiconductor Science and Technol., vol. 25, no. 1, pp. 015004 (1-5), January 2010.
- [82] G. Koblmüller, C. S. Gallinat, S. Bernardis, J. S. Speck, G. D. Chern, E. D. Readinger, H. Shen and M. Wraback, "Optimization of the surface and structural quality of N-face InN grown by molecular beam epitaxy," Applied physics letters, vol. 89, no. 7, pp. 071902 (1-3), August 2006.
- [83] K. Wang, T. Kosel and D. Jena, "Structural and transport properties of InN grown on GaN by MBE," Physica Status Solidi C, vol. 5, no. 6 pp. 1811-1814, May 2008.
- [84] D. Gershoni, C. H. Henry and G. A. Baraff, "Calculating the Optical Properties of Multidimensional Heterostructures: Application to the Modeling of Quaternary Quantum Well Lasers," IEEE Journal of Quantum Electronics, Vol. 29, No. 9, pp. 2433-2450, September 1993.